Planification des ressources radio dans les réseaux IoT longues portées avec faible puissance

Yi Yu

le cnam

ÉCOLE DOCTORALE EDITE
LISITE, ISEP Paris

THÈSE DE DOCTORAT

présentée par : **Yi YU**
soutenue le : **29 Janvier 2021**

pour obtenir le grade de : **Docteur du Conservatoire National des Arts et Métiers**

Discipline : **Génie électrique, électronique, photonique et systèmes**

Spécialité : **Radiocommunications**

Radio Resource Planning in Low Power Wide Area IoT Networks

THÈSE dirigée par

Mme Mroueh Lina	*Enseignante-Chercheuse, ISEP*
M. Terré Michel	*Professeur, CNAM*

PRÉSIDENT DU JURY

Mme Helard Maryline	*Professeur, INSA Rennes*

RAPPORTEURS

M. Di-Renzo Marco	*Directeur de recherche, CNRS*
M. Clavier Laurent	*Professeur, IMT-Lille*

EXAMINATEURS

M. Martins Philippe	*Professeur, Télécom ParisTech*
M. Vivier Guillaume	*Senior Director, Sequans*
M. Slock Dirk	*Professeur, Eurecom*

MEMBRES INVITÉS

M. Bader Carlos	*Professeur, ISEP*

Publications

Journal Papers

1. **Y. Yu**, L. Mroueh, D. Duchemin, C. Goursaud, G. Vivier, J.-M Gorce, and M.Terré, "Adaptive Multi-Channels Allocation in LoRa Networks," in IEEE Access, vol. 8, pp. 214177-214189, 2020.

2. **Y. Yu**, L. Mroueh, P. Martins, G. Vivier and M. Terré, "Radio Resource Dimensioning for Low Delay Access in Licensed OFDMA IoT Networks." Sensors 2020, 20, 7173.

Related Thesis Conference Papers

1. **Y. Yu**, L. Mroueh, S. Li and M. Terré, "Multi-Agent Q-Learning Algorithm for Dynamic Power and Rate Allocation in LoRa Networks," IEEE 31st Annual International Symposium on Personal, Indoor and Mobile Radio Communications (PIMRC), London, United Kingdom, 2020.

2. **Y. Yu**, L. Mroueh, G. Vivier and M. Terré, "Packet Recovery Latency of a Rate-less Polar Code in Low Power Wide Area Networks," European Conference on Networks and Communications (EuCNC), Valencia, Spain, 2019.

3. G. Vivier, V. Mannoni, F. Dehmas, V. Berg, L. Mroueh, **Y. Yu**, D. Duchemin, J.-M Gorce, J. Manco-Vasquez and F. Bader, "Beyond LoRa and NB-IoT: Proposals for Future LPWA Systems," European Conference on Networks and Communications (EuCNC), Valencia, Spain, 2019.

4. L. Mroueh, **Y. Yu**, M. Terré and P. Martins, "Statistical Uplink Dimensioning in Licensed Cellular Low Power IoT Networks," 25th International Conference on Telecommunications (ICT), St. Malo, 2018.

Other Conference Papers

1. J. Yu, A. Hu, F. Zhou, Y. Xing, **Y. Yu**, G. Li and L. Peng, "Radio Frequency Fingerprint Identification Based on Denoising Autoencoders," International Conference on Wireless and Mobile Computing, Networking and Communications (WiMob), Barcelona, Spain, 2019.

2. **Y. Yu**, M. Pischella and D. Le Ruyet, "Distributed antenna selection with message passing algorithm for MIMO D2D communications," International Symposium on Wireless Communication Systems (ISWCS), Bologna, 2017, pp. 454-458.

Contents

List of Tables

List of Figures

List of Acronyms

IoT Internet of Things

RFID Radio Frequency Identification

NB-IoT Norrow-Band Internet of Things

LTE-M (LTE-MTC) Long Term Evolution-Machine Type Communication

5G Fifth Generation Mobile Communication System

4G Fourth Generation Mobile Communication System

LTE Long Term Evolution

SC-FDMA Single-Carrier Frequency Division Multiple Access

OFDMA Orthogonal Frequency Division Multiple Access

OFDM Orthogonal Frequency Division Multiplexing

CAGR Compound Annual Growth Rate

LPWAN Low Power Wide Area Networks

QoS Quality of Service

BLE Bluetooth Low Energy

NFC Near Field Communication

ISM Industrial Scientific Medical Band

GSM Global System for Mobile Communications

PHY PHYsical layer

MAC Medium Access Control layer

CSS Chirp Spread Spectrum

FEC Forward Error Correction

3GPP 3rd Generation Partnership Project

LTE-M LTE-Machine Type Communications

VoLTE Voice over LTE

UMTS Universal Mobile Telecommunications System

GPRS General Packet Radio Service

PRB Physical Resource Block

UE User Equipment

CP Cyclic Prefix

QAM Quadrature Amplitude Modulation

RE Resource Element

QPSK Quadrature Phase Shift Keying

BPSK Binary Phase Shift Keying

NPUSCH Narrowband Physical Uplink Shared Channel

NPRACH Narrowband Physical Random Access Channel

NPSS/NSSS Narrowband Synchronization Signal

NPDCCH Narrowband Physical Downlink Control Channel

NPBCH Narrowband Physical Broadcast Channel

MCL Maximum Coupling Loss

PUSCH Physical Uplink Shared Channel

PRACH Physical Random Access Channel

PUCCH Physical Uplink Control Channel

PDSCH Physical Downlink Shared Channel

SS/SSS Synchronization Signal

PBCH Physical Broadcast Channel

EPDCCH PEnhanced Physical Downlink Control Channel

AI Artificial Intelligence

mMTC massive Machine Type Communications

eMBB enhanced Mobile Broadband

URLLC Ultra-Reliable Low-Latency Communications

i.i.d independent and identically distributed

TDD Time Division Duplexing

UL Uplink

DL Downlink

ITU International Telecommunication Union

IMT International Mobile Telecommunication

cMTC critical Machine Type Communications

MTC Machine Type Communication

NSA Non Standalone

SA Standalone

NR New Radio

5GC 5G Core

RAN Radio Access Network

mmWave millimeter-Wave

BS Base Station

SISO Single Input Single Output

SIMO Single Input Multiple Output

MIMO Multiple Input Multiple Output

MU-MIMO Multi-User Multiple Input Multiple Output

PPP Poisson Point Process

ML Machine Learning

RL Reinforcement Learning

TD Temporal-Difference

M2M Machine-to-Machine

RRM Radio Resource Management

CSI Channel State Information

RR Radio Resource

ZF Zero Forcing

LLS Link Layer Simulation

MRC Maximum Ratio Combiner

PMF Probability Mass Function

SF Spreading Factor

FFT Fast Fourier Transform

PGFL Probability Generating Functional

IDT Independent Double Thinning Approach

UDN Ultra Dense Networks

Résumé détaillé de la thèse

L'Internet des objets (IdO) est un sujet émergent et évolutif qui couvre un large éventail de technologies assurant la communication entre les objets. L'IdO est rendu possible par les derniers développements en matière d'identification par radiofréquence (RFID), de capteurs intelligents, de technologies de communication et de protocoles Internet. Il peut effectuer l'identification, le positionnement, le suivi, la surveillance et la gestion intelligents des dispositifs, ce qui offre d'énormes avantages pour le domaine industriel [1, 2, 3, 4, 5]. Les réseaux étendus à faible puissance (LPWAN) sont une catégorie de technologies innovantes de l'IdO conçues pour fournir des services IdO avec une large couverture, une connexion massive, un faible coût et une faible consommation d'énergie. Les technologies LPWAN comprennent les technologies opérant dans des bandes licenciées comme le Narrow-Band IoT (NB-IoT), le LTE-M, ou en bande non licenciée comme le LoRa ou Sigfox, etc. Dans cette thèse, nous nous concentrons sur les questions d'optimisation de consommation énergétique et de planification des ressources pour les réseaux IoT longues portées.

Chapitre 1: Contexte de recherche

Le chapitre 1 illustre le contexte de recherche du LPWAN. Le réseau IoT illustré dans la Figure 1 contient généralement un grand nombre de dispositifs connectés tels que des capteurs. Il permet les communications entre différents dispositifs ou entre des dispositifs et le réseau central. Selon les différents cas d'utilisation, ces dispositifs peuvent être utilisés pour la détection simple de paramètres environnementaux tels que la concentration de CO_2, l'humidité de l'air, etc., ou ils peuvent être utilisés pour la détection et l'exécution d'instructions plus complexes. Les nœuds peuvent transmettre les informations collectées à un réseau fédérateur ou au cloud via une liaison montante. Après que les informations aient été analysées et traitées à distance par les terminaux, les opérations appropriées peuvent être transmises à l'appareil via une liaison descendante. La liaison descendante peut également

être utilisée pour accuser réception des informations. Les utilisateurs autorisés ont accès aux données stockées sur le serveur distant.

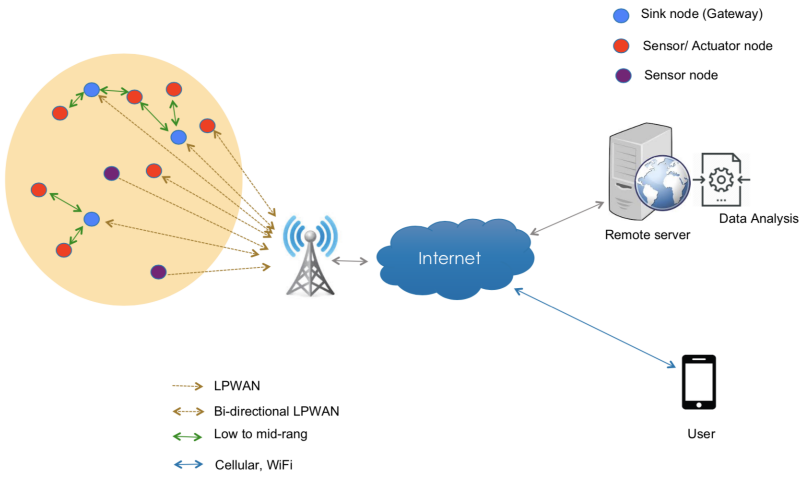

Figure 1: Architecture générale des réseaux IoT

Différentes technologies IdO sont utilisées pour transmettre des informations à partir d'un capteur et éventuellement à un actionneur [6, 7, 8, 9, 10]. Lorsque nous envisageons un scénario réel, il n'y a souvent pas de choix technique optimal absolu, mais plutôt une recherche des technologies IdO appropriées. Une technologie IdO peut être choisie pour un cas particulier à condition qu'elle atteigne les objectifs souhaités en termes de budget, de débit de données, de couverture, de qualité de service et de durée de vie de batterie. Les réseaux IdO basées sur des communications de courte portées reposent sur l'utilisation de schémas de communication à sauts multiples pour connecter les capteurs à la passerelle locale. Les technologies de communication à grande portée ne nécessitent qu'un seul saut pour connecter les appareils et le réseau central. Elles simplifient ainsi les protocoles et améliorent l'efficacité de la communication.

Les réseaux Low Power Wide Area (LPWA) sont prometteurs et impératifs pour l'expansion et le développement des réseaux IdO et de leur infrastructure de connectivité [11]. Ils fournissent des services IdO à faible puissance, à grande échelle et à faible coût pour des dispositifs massivement connectés. Ils offrent également une très longue durée de vie de batterie. Il existe différentes technologies LPWAN, telles que LoRa [12, 13] , NB-IoT [14, 15] et LTE-M [16], etc. Par exemple, le NB-IoT peut coexister avec le Global System for Mobile communications (GSM) et le LTE dans des bandes de fréquences

sous licence (par exemple, 900 MHz). La technologie LoRa fonctionne sur des bandes de fréquences non licenciées par exemple, 868 MHz en Europe, et 915 MHz aux Etats-Unis. Les réseaux IoT sous licence sont dédiés aux applications IoT critiques en temps réel nécessitant un certain niveau de QoS, de sécurité, de fiabilité et de latence. Le réseau sans licence est plus adapté aux cas d'utilisation massive de l'IdO non critique et en temps non réel. Ces trois technologies sont présentées en détail dans le chapitre 1.

Le réseau LoRa adopte la modulation à étalement de spectre Chirp (CSS), qui est une modulation à étalement de spectre [17]. La modulation CSS utilise des impulsions chirp dont la fréquence varie linéairement sur la largeur de bande pour coder les informations. Un chirp, également appelé signal de balayage, est une tonalité dont la fréquence augmente ou diminue avec le temps. L'augmentation est appelée up-chirp et la diminution est appelée down-chirp. Dans les réseaux LoRa, un nœud de capteur, situé loin du collecteur, subit la collision causée par les autres capteurs actifs qui envoient simultanément des informations et sont situés plus près du collecteur. La technique d'étalement CSS peut protéger les nœuds de capteurs en bordure de cellule des nœuds situés à proximité du collecteur du réseau. Elle comporte des facteurs d'étalement possibles de 6 (SF = 7 à 12) vers les capteurs actifs en fonction de la sensibilité du récepteur et donc des seuils de communication.

NB-IoT et LTE-M (également connu sous le nom de LTE-MTC) sont deux technologies LPWA, normalisées par le 3GPP, qui fournissent des communications IoT cellulaires à bande étroite pour les appareils connectés [18, 19, 20]. L'IoT NB est exploité sur une bande de fréquences sous licence. Il peut être déployé directement sur les réseaux cellulaires existants, par exemple, les réseaux GSM, UMTS (Universal Mobile Telecommunications System) ou LTE. Les terminaux IoT sont connectés au réseau de l'opérateur en étant équipés de modules de communication sans fil et de cartes SIM. Il permet de construire différents types d'applications industrielles centralisées. Le réseau NB-IoT utilise des modulations par déplacement de phase en quadrature (QPSK) et par déplacement de phase binaire (BPSK). Il s'agit dans les deux cas de modulations de phase numériques avec de bonnes performances en terme de probabilité d'erreur. Le budget de liaison du NB-IoT est d'environ 150 dB. Le LTE-M présente également des caractéristiques importantes pour les communications sans fil de l'IdO, telles que le faible coût, la longue durée de vie de batterie et la couverture de longueur portée. Tout comme le réseau NB-IoT, il peut coexister avec les systèmes GSM et LTE en utilisant le spectre GSM ou LTE. Il peut être facilement déployé en mettant à niveau un réseau cellulaire existant. Le débit du LTE-M

est supérieur à 200 kbps avec un budget de liaison maximal de 156 dB [16].

Le lancement de la 5G ouvre également de nouvelles possibilités pour l'IdO [21, 22, 23]. La 5G fournit un écosystème et un soutien technique solide à l'IdO. L'IMT-2020 définit 3 cas d'usage à la 5G: les communications massives de type machine (mMTC), les communications critiques de type machine (cMTC) et le haut débit mobile amélioré (eMBB) [24, 25]. mMTC correspond aux communications IoT massives qui doivent avoir une large couverture, un grand nombre de dispositifs, un faible coût d'équipement, un faible coût énergétique et une sécurité élevée. cMTC est préparé pour les réseaux IoT critiques avec des exigences élevées en matière de latence, de fiabilité et de sécurité du réseau. Il est également appelé Ultra-Reliable Low-Latency Communications (URLLC). eMBB est conçu pour les communications à haut débit et à faible latence. Il existe deux scénarios différents pour les réseaux 5G. L'un est le réseau 5G non autonome, ou non standalone en anglais (NSA) et l'autre est le réseau 5G autonome, standalone (SA). La 5G offre de nouvelles possibilités de connectivité IdO à grande échelle en fournissant un niveau plus élevé de support technique. Elle vise à permettre aux réseaux IoT de connecter plus de dispositifs, d'améliorer la fiabilité du réseau et de réduire la consommation d'énergie.

La technologie multi-antennes a permis d'améliorer l'efficacité spectrale dans les réseaux cellulaires classiques. Dans ce chapitre, nous présentons les systèmes d'antennes multiples dans les réseaux IoT LPWA en tenant compte de la limitation en complexité des objets connectés. Ensuite, nous présentons les outils de géométrie stochastique permettant de modéliser la distribution aléatoire des objets et des stations dans le réseau [26, 27, 28, 29, 30, 31, 32, 33, 34, 35, 36, 37, 38]. Les théorèmes et les propriétés des PPP sont présentés en détail. Ensuite, nous présentons des préliminaires sur l'algorithme d'apprentissage automatique le Q-learning [39, 40, 41, 42] qui sera appliqué à l'allocation dynamique des ressources dans les réseaux LPWA dans le dernier chapitre de la thèse.

Chapitre 2: Dimensionnement statistique dans les réseaux IoT OFDMA à faible délai d'accès

Dans le chapitre 2, nous nous concentrons sur la planification des ressources radio dans la liaison montante des réseaux à accès multiple utilisant l'OFDMA comme le NB-IoT, le LTE-M ou dans une moindre mesure la 5G avec la numérologie 0. Le comportement moyen du réseau est considéré en supposant que les capteurs et les collecteurs actifs sont distribués selon deux processus de points de

Poisson (PPP) aléatoires indépendants, marqués par le caractère aléatoire du canal. Nous supposons que les capteurs sont équipés d'une seule antenne et que le collecteur est équipé d'antennes de réception n_r. Ce cadre d'hypothèses définit le PPP spatial dans lequel les positions des nœuds actifs sont uniformes sachant que le nombre de nœuds est distribué selon le principe de Poisson. On considère que les capteurs sont distribués dans une zone donnée $\mathcal{A}$ selon un PPP spatial Φ_s. Nous supposons qu'un capteur est actif n_a fois par jour, que le temps de service moyen est ν^{-1} (s) et que le taux d'interception est $\frac{n_a}{24\times60\times60}\,\rho$ par seconde et par km^2. Les nœuds de capteurs actifs forment alors une PPP spatiale Φ_a avec l'intensité

$$\lambda_a = \frac{n_a}{24 \times 60 \times 60}\,\rho\,\nu^{-1}.$$

Le schéma de réutilisation des fréquences dans le réseau est égal à 1.

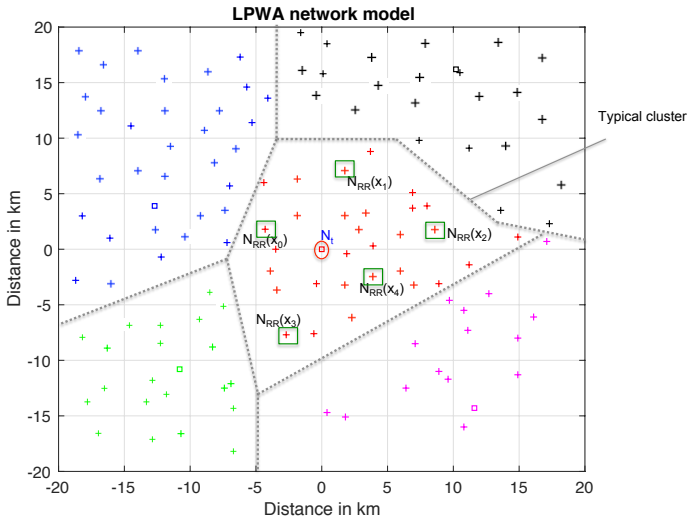

Figure 2: Modèle du réseau: cellule typique et nœuds actifs

Pour un collecteur donné situé à $y_0 \in \Phi_b$, la puissance reçue sur une ressource radio (RR) donnée d'un capteur $x \in \Phi_a$ émettant avec la puissance P_{RR} (mW par RR) est calculée comme suit, $P_r(y_0, x) = P_{\text{RR}}\,\alpha\,|y_0 - x|^{-\beta}\,A_f$ où α et β sont respectivement le facteur d'atténuation (qui inclut l'effet de masque moyen) et l'exposant d'atténuation de trajet calculés à partir du modèle Okumura-Hata, A_f est le coefficient d'évanouissement avec une distribution dépendant de la configuration de l'antenne et du mode de transmission utilisé (mono ou multi-utilisateur). En supposant un collecteur y_0, l'ensemble des capteurs connectés à ce dernier est défini comme $\Phi_c(y_0) = \{x \in \Phi : \forall y \in \Phi_b - \{y_0\} : |y_0 - x| < |y - x|\}$. Les nœuds émettant dans la même bande de fréquences génèrent une interférence additive avec la

puissance

$$I\left(y_0\right) = \sum_{x_i \in \Phi_I(y_0)} P_{\mathrm{RR}} \alpha \left|y_0 - x_i\right|^{-\beta} A_{f,i}, \tag{1}$$

avec

$$\Phi_I\left(y_0\right) = \cup_{y \in \Phi_b, y \neq y_0} \left\{x_i : x_i \text{ randomly selected in } \Phi_c(y)\right\}. \tag{2}$$

Le SINR reçu au niveau du collecteur donné y_0 est,

$$\mathrm{SINR}(y_0, x) = \frac{P_{\mathrm{RR}}\ \alpha\ \left|y_0 - x\right|^{-\beta}\ A_f}{P_n + I(y_0)} \tag{3}$$

avec P_n étant le bruit aléatoire à puissance moyenne de $\bar{P}_n = KTB$ où K est la constante de Boltzmann $K = 1,379 \times 10^{-23}$ W Hz^{-1} K^{-1}, T la température absolue en kelvins $T = 290$ K et B la largeur de bande.

Notre objectif est de déterminer statistiquement le nombre total optimal de ressources radio (RR) nécessaires pour une cellule type qui est,

$$N_{\mathrm{RR}}(x, A_f, I, P_n) = \sum_{k=1}^{N_{\max}} k \times \mathbb{1}_{\left\{\ \mathrm{SINR}(x)\ \in\ [\gamma_k\ ;\ \gamma_{k-1}[\right\}}. \tag{4}$$

avec γ_k étant le seuil SINR requis pour atteindre un taux cible de C_0/k dans un seul RR et $\gamma_0 > \gamma_1 > ... > \gamma_{N_{\max}}$ et $\gamma_0 \to \infty$. D'une part, la largeur de bande allouée doit être suffisamment importante pour supporter le trafic des appareils et garantir un faible délai d'accès. D'autre part, le sur-dimensionnement est coûteux du point de vue de l'opérateur et induit un gaspillage de spectre. C'est pourquoi nous proposons des outils statistiques dérivés de la géométrie stochastique pour évaluer, ajuster et adapter la bande passante allouée en fonction des paramètres du réseau, à savoir la qualité de service (QoS) requise en termes de débit et de délai d'accès, la densité des capteurs actifs, les intensités des collecteurs, les configurations des antennes et les modes de transmission. Le nombre total de RR requis dans une cellule centrée autour de 0 comme illustré dans la Figure 2.1 est,

$$N_{RR,t}(0) = \sum_{x \in \Phi_c(y_0)} N_{RR}(x, A_f, I, P_n).$$

On définit l'évenement de dépassement dans le réseau par l'évenement qui survient quand le nombre de ressources demandé par les objets dépassent le nombre maximal de ressource disponible dans le réseau N_t, *i.e.*,

$$\mathbb{P}_{\mathrm{out},c}(N_t) = \mathrm{Prob}\{N_{RR,t}(0) > N_t\}.$$

Nous calculons le délai moyen pour connecter l'objet connecté au réseau. Ce délai moyen ne doit pas dépasser un délai maximal $\tau_{\max}$ que nous supposons proportionnel au Time Transmission Interval (TTI). Nous supposons que les probabilités d'être rejeté après $i \times$ TTI sont indépendantes et sont égales à $\left(\mathbb{P}_{\text{out},c}(N_t)\right)^i$.

$$\bar{\tau} = \left(\sum_{i=0}^{\infty} i \times \text{TTI} \times \left(\mathbb{P}_{\text{out},c}(N_t)\right)^i\right) \leq \left(\sum_{i=0}^{\infty} i \times \text{TTI} \times p_{th,n}^i\right).$$

En laissant $\kappa = \tau_{\max}/\text{TTI}$, le seuil du réseau est,

$$p_{th,n} = \frac{(2\kappa + 1) - \sqrt{1 + 4\kappa}}{2\kappa} < 1. \tag{5}$$

Le nombre total optimal de RR requis pour une cellule type est ensuite calculé en tenant compte conjointement des contraintes de faible délai d'accès, de puissance limitée par RR, de débit de données cible et de probabilité d'interruption du réseau. Différents types de réseaux sont pris en compte, notamment les systèmes de type Single Input Single Output (SISO), Single Input Multiple Output (SIMO) utilisant la sélection d'antenne ou le Maximum Ratio Combiner (MRC), et les systèmes multi-utilisateurs (MU-MIMO).

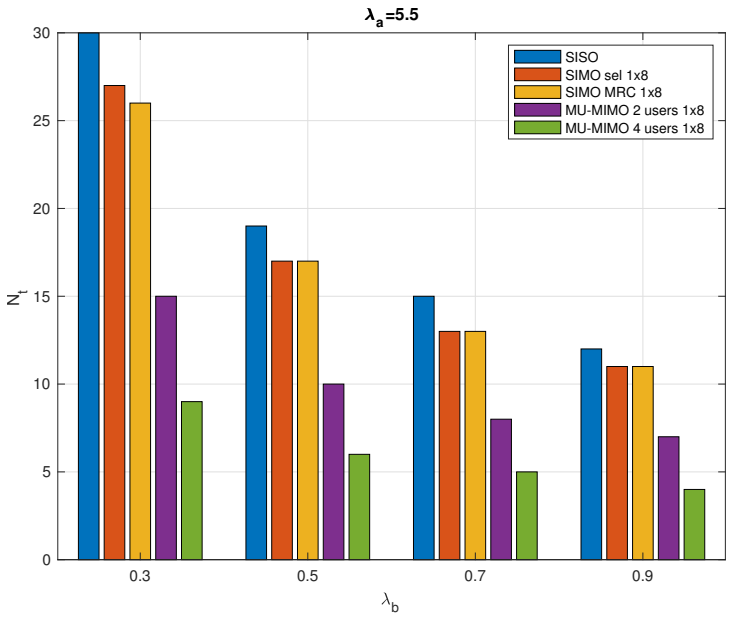

Figure 3: Nombre total de RR requis dans une cellule type en fonction de l'intensité du collecteur λ_b avec $\lambda_a = 5,5$ nœuds/km^2, $\tau_{max} = 1$ ms.

La comparaison des résultats théoriques avec les résultats des simulations empiriques montre que les résultats obtenus à partir de notre modèle statistique sont très proches des résultats empiriques.

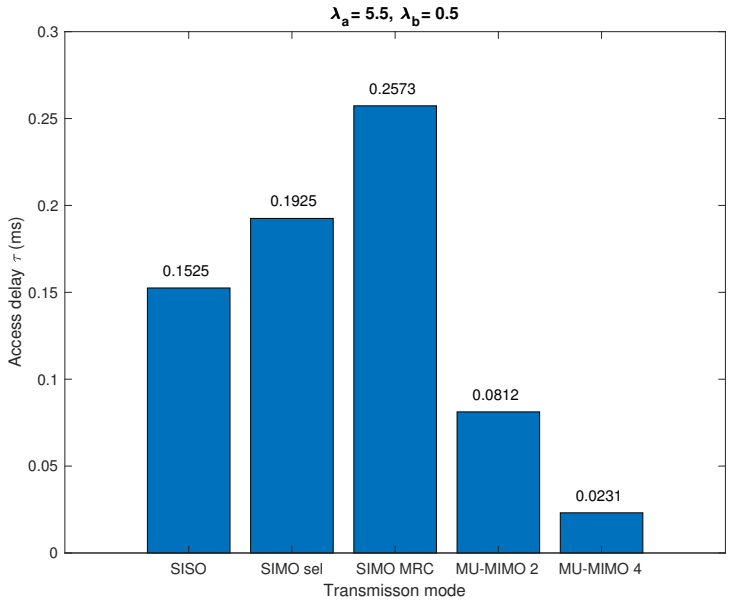

Figure 4: Délai d'accès réel τ avec dimensionnement statistique calculé avec un délai maximal $\tau_{max} = 1$ ms, $\lambda_a = 5,5$ noeuds/km^2 et $\lambda_b = 0,5$ noeuds/km^2.

La Figure 3 présente le nombre total de RR requis dans une cellule typique en fonction de l'intensité du collecteur. La Figure 4 montre le retard d'accès moyen réel correspondant à différentes configurations d'antennes et à différents modes de transmission pour des intensités données de capteurs et de collecteurs actifs λ_a, λ_b, et le retard d'accès maximum $\tau_{max} = 1$ ms. Il ressort de la figure que le délai d'accès moyen τ est inférieur au délai d'accès maximum τ_{max}. Le SIMO avec mode de transmission MRC nécessite le temps d'accès le plus long car il a la plus faible probabilité de dépassement individuel, c'est-à-dire qu'il dessert le plus grand pourcentage de nœuds actifs. Le deuxième délai d'accès le plus long est celui du SIMO avec schéma de sélection d'antenne. Pour la configuration SISO, le délai d'accès moyen est relativement plus faible car dans ce mode, de nombreux nœuds sont en état de repos et ne sont pas desservis. Pour le système MU-MIMO, chaque fois qu'il y a des nœuds n_u, ils transmettent des informations simultanément et sont traités par le collecteur. Plus le n_u est important, plus le délai d'accès moyen nécessaire est court.

Avec la demande croissante de connectivité sans fil pour l'IdO, les ressources en bande licenciée sont limités et coûteux et ne peuvent pas répondre pleinement à toutes les exigences du marché. Ces technologies devraient être complétées par des technologies fonctionnant dans des bandes sans licence offrant un accès massif pour des applications non critiques et en temps réel. Dans les prochains

chapitres, nous nous concentrerons sur l'atténuation des interférences dans les réseaux LoRa.

Chapitre 3: Allocation adaptive de canaux multiples dans les réseaux LoRa

Dans le chapitre 3, nous considérons un réseau dédié à l'IdO correspondant à un réseau LoRa sans licence. Le réseau LoRa fonctionne dans la bande de 868 MHz sans licence dans une largeur de bande totale de 1 MHz divisée en 8 canaux orthogonaux de 125 kHz chacun. Malgré le niveau élevé d'interférences, ce réseau offre des communications à longue distance de l'ordre de 2 à 5 km dans les zones urbaines et de 10 à 3 km dans les zones rurales. Pour atténuer efficacement ce niveau élevé d'interférence, le réseau LoRa repose essentiellement sur une modulation à étalement de spectre par impulsions et sur des mécanismes de diversité de répétition. La modulation Chirp Spread Spectrum (CSS) de LoRa étale le signal dans une bande de 125 kHz en utilisant 6 facteurs d'étalement possibles (de 7 à 12) pour atteindre les débits de données cibles (de 5 kbps pour le nœud le plus proche à 300 bps pour les plus éloignés). Les mécanismes de diversité de répétition permettent la récupération des données lorsque la transmission est soumise à de mauvaises conditions de canal et/ou à des niveaux d'interférence élevés.

Nous considérons la liaison montante d'un réseau LoRa dans lequel un ensemble de dispositifs actifs Φ_a sont distribués dans une région $\mathcal{A}$ selon un PPP homogène caractérisé par son intensité λ_a nœuds par km^2. Nous supposons qu'il n'y a pas de coordination entre les dispositifs de transmission. Les collecteurs sont distribués selon une distribution spatiale PPP avec intensité λ_b collecteurs par km^2 et nous laissons Φ_b désigner l'ensemble des collecteurs. En raison du théorème de Slivnyak-Mecke dans [27], le comportement statistique dans le PPP reste inchangé lorsque l'on ajoute un collecteur au centre de cette région. Nous supposons que chaque nœud de capteur est connecté au collecteur le plus proche. Nous nous concentrons sur la cellule typique centrée à l'origine o contenant l'ensemble de tous les nœuds de capteurs connectés à o.

En ce qui concerne la politique d'attribution des canaux de taille fixe, tous les nœuds du réseau transmettent dans une sous-bande de taille fixe B_0 choisie parmi $B_0 = 125, 250$ et 500 kHz, *i.e.*

$$\forall x \in \Phi_a : B_a(x) = B_0.$$

L'interférence intra sous-bande est induite par des nœuds qui sélectionnent la même sous-bande pour la

transmission. Chaque sous-bande est accessible avec la même probabilité $\text{Prob}\{e_{B_0}(x) = k\} = 1/N_m$, $\forall\ k$. Bien que la modulation CSS protège les dispositifs à cellules de bordure contre le niveau élevé d'interférence induit par les nœuds à proximité du collecteur, elle ne protège pas les nœuds en bordure d'une région SF donnée. Pour résoudre ce problème, nous proposons de diminuer l'efficacité spectrale pour les nœuds de bordure des régions SF. Pour ce faire, nous augmentons progressivement, à l'intérieur de chaque région SF, la taille de la bande passante tout en conservant le même débit de données, comme le montre la figure 5.

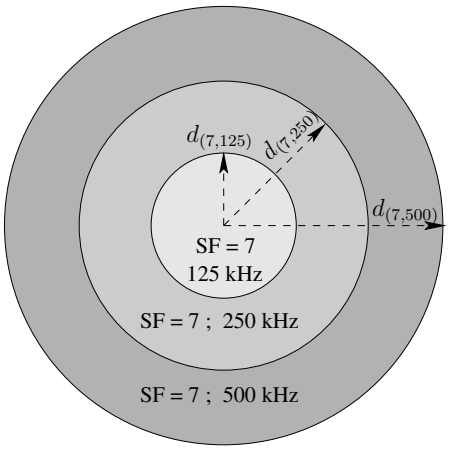

Figure 5: Allocation de canaux multiples dans les zones de SF

Pour un nœud donné $x \in \mathcal{A}_{\text{SF}}$, la taille de la sous-bande allouée à ce nœud en utilisant la politique adaptative multicanaux est,

$$B_a(x) = \sum_{B_0 \in \{125,250,500\}} B_0 \times \mathbb{1}_{\{x \in \mathcal{A}_{\text{SF}} \cap \mathcal{B}_{B_0}\}},$$

avec

$$\mathcal{A}_{\text{SF}} \cap \mathcal{B}_{B_0} = \{x \in \Phi_a : d_{\text{in}} \leq |x| < d_{(\text{SF},B_0)}\}$$

et

$$d_{\text{in}} = \begin{cases} \rho_{\text{SF}-1} & B_0 = 125 \text{ kHz}; \\ d_{(\text{SF},B_0/2)} & \text{else.} \end{cases}$$

Notre objectif est de trouver les valeurs appropriées de ces plages de communication $d_{(\text{SF},B_0)}$ pour minimiser la probabilité moyenne de coupure individuelle dans la cellule en tenant pleinement compte du facteur d'inter-corrélation $c(x, y)$. Ce chapitre présente une expression analytique de la probabilité de coupure dans un réseau LoRa dans lequel différents facteurs de propagation et différentes largeurs de

bande de canal sont utilisés. Sur la base des propriétés du PPP, nous avons caractérisé statistiquement la distribution des interférences dans une cellule typique en tenant compte du facteur d'inter-corrélation entre les différents facteurs d'étalement ainsi que des différentes largeurs de bande allouées. Sur la base de ces expressions, nous avons calculé dans chaque région SF le rayon extérieur des régions où une plus grande largeur de bande est nécessaire pour minimiser la probabilité moyenne de coupure.

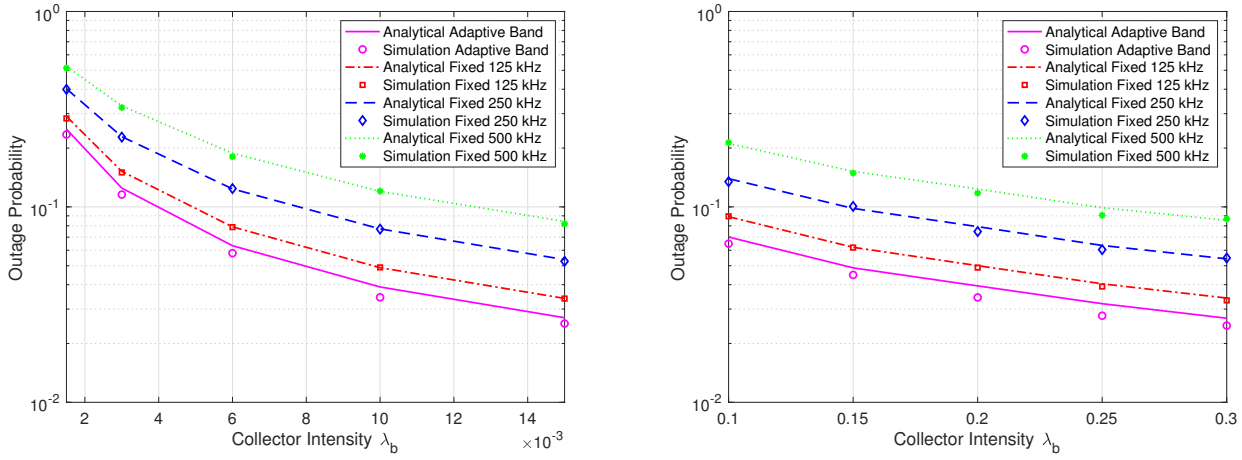

(a) Rural environment

(b) Urban environment

Figure 6: Comparaison de la probabilité moyenne de coupure théorique et empirique pour les politiques avec bande fixe et adaptative

Comme nous pouvons le voir dans les Figures 6(a) et 6(b) correspondant respectivement aux environnements urbain et rural, la différence entre les résultats numériques et les résultats analytiques est négligeable, ce qui valide nos résultats analytiques dérivés. Pour toutes les politiques d'allocation de bande, l'augmentation du nombre de collecteurs réduit la taille des cellules typiques et augmente le niveau du SINR reçu et par conséquent diminue la probabilité de coupure. On peut observer sur les Figures 6(a) et 6(b) que l'augmentation de la taille de la bande passante fixe allouée augmente le nombre de collisions du réseau. Le niveau d'interférence augmente de manière significative et cela ne peut pas être compensé par le gain de seuil SINR par rapport au cas de 125 kHz. Pour la bande adaptative, le choix optimisé du rayon délimitant les bandes réduit la probabilité moyenne de coupure par rapport à la politique d'attribution fixe. On peut également noter que les probabilités de coupure ont approximativement les mêmes portées dans les cas ruraux et urbains dans les Figures 6(a) et 6(b), ce qui est dû à la compensation du niveau élevé d'interférence dans la cellule urbaine fortement

chargée, par la perte de trajet des longues portées de communication rurales.

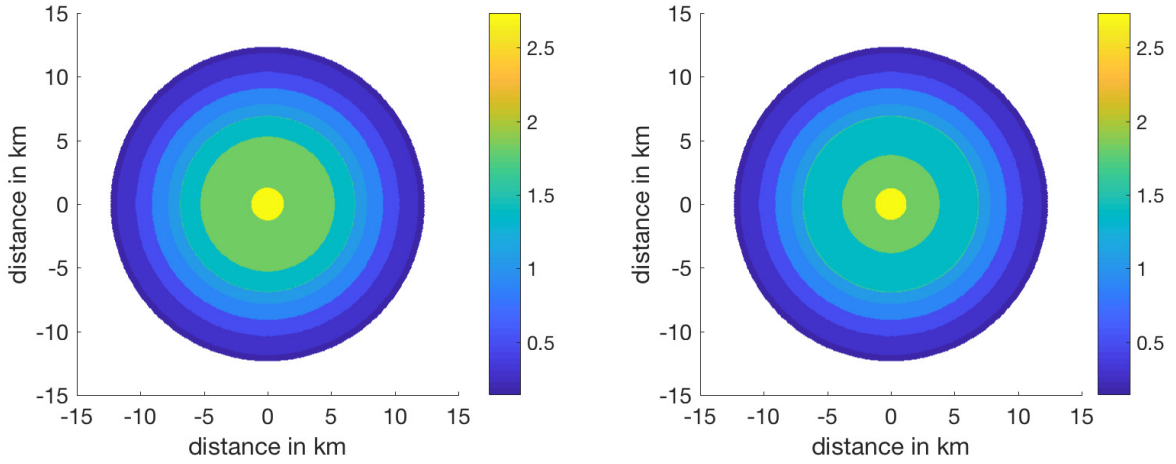

(a) Environment rural: $\lambda_b = 0.01$ collecteurs par km^2

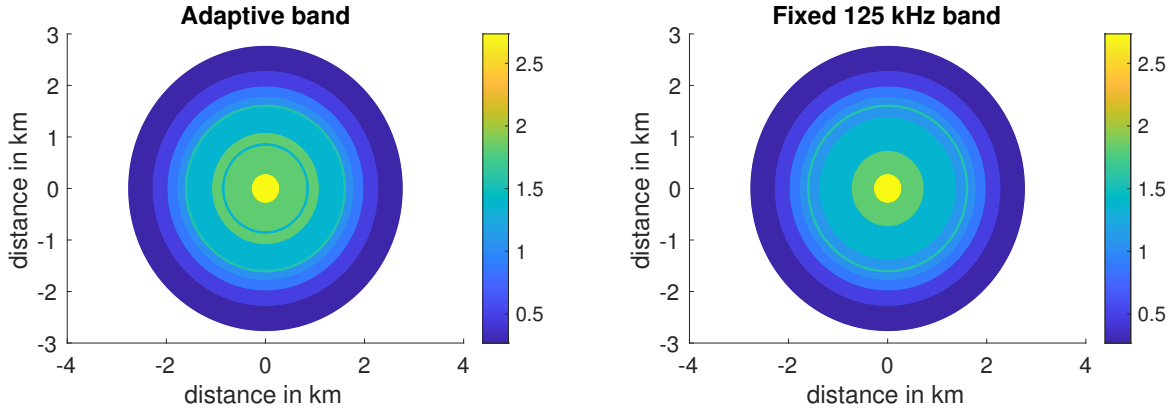

(b) Environment urbain: $\lambda_b = 0.2$ collecteurs par km^2

Figure 7: Distribution des débits en kb/s dans la cellule

Les résultats numériques montrent que la répartition optimisée des sous-bandes adaptatives surpasse les probabilités moyennes de coupure avec une politique d'allocation de bande fixe. De plus, elle améliore la distribution du taux dans la cellule en diminuant statistiquement le nombre d'essais requis pour les nœuds de bordure en utilisant le facteur d'étalement de 7, comme le montre la Figure 7. Ces résultats peuvent être très utiles aux planificateurs de réseau pour trouver les paramètres de dimensionnement du réseau : les intensités des collecteurs, la consommation électrique maximale et pour estimer la distribution moyenne du débit de données dans le réseau.

Dans ce chapitre, nous avons mis en oeuvre une stratégie statistique d'allocation de bande dans

le réseau LoRa basée sur la géométrie stochastique. L'analyse du réseau LoRa dans ce chapitre nous a amené à nous demander si d'autres méthodes dynamiques peuvent être utilisées pour allouer efficacement et dynamiquement les ressources du réseau afin de satisfaire les besoins de communication des nœuds de capteurs connectés au réseau IoT. C'est pourquoi, dans le prochain chapitre, nous utiliserons un algorithme d'apprentissage automatique pour gérer l'allocation dynamique des ressources dans les réseaux LoRa.

Chapitre 4: Apprentissage Multi-Agent pour l'allocation des ressources dans les réseaux LoRa

Dans le chapitre 4, nous nous concentrons sur les réseaux LoRa. En termes de budget de liaison, les nœuds éloignés du collecteur subissent des collisions causées par les nœuds proches du collecteur lors des transmissions de données. Afin d'améliorer l'efficacité énergétique et la fiabilité des communications, nous proposons une application de l'apprentissage multi-agent Q dans l'allocation dynamique de la puissance et du SF aux nœuds actifs pour les communications en liaison montante dans la LoRa. L'objectif principal de ce chapitre est de réduire la consommation d'énergie des transmissions en liaison montante et d'améliorer la fiabilité du réseau. Le Q-learning est un algorithme RL populaire qui a de nombreuses applications dans le domaine de l'ingénierie de contrôle, des systèmes multi-agents et de la recherche opérationnelle. C'est un outil efficace et dynamique d'aide à la décision. Il adopte des méthodes de différence temporelle (TD) hors politique pour que les agents apprennent à agir de manière optimale afin de contrôler les problèmes. En considérant les systèmes multi-agents dans une variété de domaines, y compris la robotique, le contrôle distribué et les télécommunications, l'algorithme d'apprentissage Q multi-agent donne des performances exceptionnelles dans les problèmes de prise de décision pour ces scénarios compliqués [39, 40, 41, 42].

Dans ce chapitre, nous considérons une seule cellule du réseau LoRa. Le rayon de couverture de la cellule est de R. Nous supposons que le collecteur est situé au centre de la cellule et que les nœuds de capteurs actifs N sont répartis de manière aléatoire dans la cellule donnée. Le terme $|x|$ indique la distance entre le nœud de capteur actif x et le collecteur o. L'interférence hors cellule est ignorée dans notre cas. En ce qui concerne la transmission en liaison montante du réseau LoRa, chaque capteur actif a 5 de choix différents pour la puissance de transmission P_t: 2, 5, 8, 11 et 14 dBm [43].

Notre objectif est de gérer l'allocation des ressources de manière dynamique. La puissance de

transmission et le facteur d'étalement SF sont alloués à chaque nœud de capteur actif afin d'assurer l'ensemble des communications du réseau. Dans le réseau LoRa, l'accès au support partagé est géré par le protocole Aloha. Les signaux transmis sur le même support interfèrent les uns avec les autres. Le collecteur reçoit en plus de son signal atténué prévu. Supposons que Φ_i désigne l'ensemble des nœuds interférents. Pour un signal prévu envoyé par le nœud x, le brouilleur $y \in \Phi_i$. La puissance de l'interférence est pondérée par un facteur de corrélation désigné par $c(x, y)$. L'expression de l'interférence est alors,

$$I_x \approx \sum_{y \in \Phi_i} c(x, y) \alpha |y|^{-\beta} A_f P_t(y), \tag{6}$$

où α et β sont respectivement le facteur d'atténuation et l'exposant de perte de trajectoire qui sont calculés à partir du modèle Okumura-Hata, A_f est le coefficient d'évanouissement aléatoire qui est distribué de manière exponentielle et $P_t(y)$ est la puissance d'émission du brouilleur y. Le facteur d'inter-corrélation $c(x, y)$ est calculé dans [44].

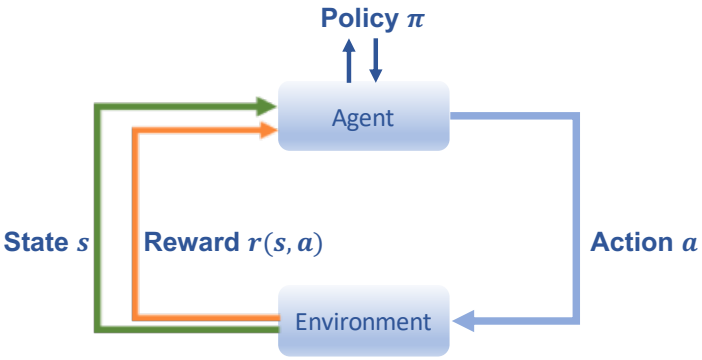

Figure 8: Apprentissage par renforcement

La Figure 8 montre le cadre général du RL. L'environnement et l'agent peuvent avoir une interaction et en tirer des enseignements pour prendre des décisions. S est l'ensemble des états possibles de l'environnement. Au temps t, en observant l'environnement, un état $s \in S$ est observé et transmis à l'agent. Ensuite, selon la politique π, l'agent décide de prendre une action $a \in A$, où A est l'ensemble des actions disponibles pour l'état s. Lorsque a est exécuté, l'agent gagne une récompense $r(s, a)$ et l'environnement se transforme en un nouvel état s'. Puisque l'agent détermine une politique π, le choix de l'action a dans un état donné s peut être décrit comme $\pi(s) = a$. Pour évaluer la performance de la politique π, la fonction de valeur d'état-action $Q(s, a)$ est introduite comme suit :

$$Q(s, a) = \mathbb{E}\left[G_t | s_t = s, a_t = a\right], \tag{7}$$

où G_t est la récompense cumulative future actualisée. L'objectif de l'apprentissage par renforcement est de trouver la meilleure politique $\pi^\star$ qui maximise la fonction de valeur état-action qui peut être décrite comme:

$$\pi^\star(s) = \arg\max_{a \in A} Q(s,a). \tag{8}$$

Le Q-learning utilise une politique non déterministe, c'est-à-dire une fonction qui associe chaque état à un ensemble d'actions afin que l'agent puisse en choisir une parmi elles, tandis qu'il est basé sur un échantillon d'autres politiques au lieu de la seule politique actuelle. Le processus de Q-learning conserve une estimation et une mise à jour de la fonction Q, elle peut s'écrire comme suit:

$$Q(s,a) = Q(s,a) + \sigma \left\{ r(s,a) + \gamma \max_{a \in A} Q\left(s', a'\right) - Q(s,a) \right\}, \tag{9}$$

où $\sigma \in [0,1]$ est un taux d'apprentissage.

Multi-Agent Q-Learning Algorithm Supposons qu'il y ait des agents de n dans le système. A un moment donné t, l'action $\boldsymbol{a} = \{a_1, a_2, ..., a_n\}$ est exécutée par tous les agents avec $a_i \in A$ étant l'action choisie par le i-ième agent. En observant l'environnement, un état courant $s \in S$ et une récompense totale $r(s, \boldsymbol{a})$ sont obtenus et transmis à tous les agents. Sur la base de l'état s et de la récompense r, chaque agent met à jour sa propre fonction d'apprentissage Q et choisit séparément une nouvelle action $a_i{}'$ pour la prochaine opération. Ensuite, l'action $\boldsymbol{a}' = \{a_1', a_2', ..., a_n'\}$ est exécutée. Le flux de travail de l'apprentissage multi-agents Q-learning reste le même que celui de l'algorithme d'apprentissage mono-agent Q-learning. Mais les informations sur l'état et la récompense sont distribuées à tous les agents, puis une décision est prise par chaque agent indépendamment.

Nous proposons de résoudre le problèmes d'allocation des SF et de contrôle de la puissance dans un réseau LoRa avec un algorithme d'apprentissage Q multi-agent. Pour chaque nœud de capteur actif connecté au collecteur o, il faut lui attribuer une valeur de SF parmi les 6 de facteurs d'étalement possibles $[7, 8, 9, 10, 11, 12]$ et une valeur de puissance d'émission sur les 5 de valeurs de puissance d'émission réalisables y compris $[2, 5, 8, 11, 14]$ dBm. Selon l'algorithme d'apprentissage Q multi-agents, le modèle de réseau LoRa est l'environnement qui fournit l'information s d'état et r de récompense pour les agents. Nous fixons $n = N$ agents pour le système. Chaque agent correspondant à un nœud de capteur actif. Un agent unique est ici une fonction d'apprentissage Q qui sélectionne une action pour un nœud actif. L'action est une paire de valeurs SF et P_t avec une probabilité ϵ ou sélectionne une

action avec une probabilité $(1-\epsilon)$ en maximisant la valeur Q,

$$a_i = \arg\max_a Q_i\left(s, a_i\right).$$

Après l'exécution de l'action $\boldsymbol{a_i}$, les agents obtiennent les nouvelles informations de l'état $s \rightarrow s'$ et une récompense r. Compte tenu de la fiabilité du réseau et de l'efficacité énergétique, la récompense r_i pour le i-ième nœud de capteur est calculée comme suit :

$$r_i = \delta_i(t) \times \varphi + \delta_i(t) \times (1-\varphi) \times \frac{P_{t\,max}}{P_t}. \tag{10}$$

où φ est un paramètre de conception offrant un compromis entre la fiabilité du réseau et l'efficacité énergétique. P_t est la puissance d'émission pour le i-ième nœud du capteur. $\delta_i(t) \in \{0, 1\}$ qui indique si le capteur i-th a une connexion stable avec le collecteur o ou non. La récompense totale pour l'action $\boldsymbol{a}$ est alors calculée comme suit :

$$r(s, \boldsymbol{a}) = \frac{1}{N}\sum_{i=1}^{N} r_i. \tag{11}$$

Nous évaluons numériquement la performance de l'algorithme d'apprentissage Q multi-agents appliqué à la sélection des SF et à l'allocation de la puissance dans le réseau LoRa en ce qui concerne la fiabilité du réseau et l'efficacité de la puissance. Nous considérons une seule cellule du réseau LoRa avec un rayon de couverture de $R = 10$ km. Supposons que les nœuds de capteurs N soient activés simultanément avec des positions aléatoires. Les nœuds de capteurs et le collecteur ont des antennes omnidirectionnelles. Les nœuds émettant dans la même bande de fréquences génèrent des interférences additives avec la puissance.

La Figure 9 montre la distribution des nœuds actifs pour 500 fois la simulation avec des agents à 5. Il y a 30 de couleurs différentes qui représentent 30 de paires de valeurs SF et P_t. On peut remarquer que la répartition conjointe des SF et de la puissance de transmission est faite de manière dynamique en fonction de la configuration instantanée du réseau. La Figure 10 présente la comparaison de la CDF de la puissance d'émission pour tous les nœuds de capteurs basée sur deux algorithmes différents. Notre algorithme d'apprentissage Q multi-agents montre de grandes améliorations de l'efficacité énergétique. En utilisant l'algorithme multi-agent Q-learning, la valeur moyenne de la puissance d'émission pour tous les capteurs actifs est égale à $4,81$ dBm alors que pour l'algorithme statique, elle est de $8,66$ dBm.

Dans ce chapitre et dans le chapitre précédent, nous avons utilisé des méthodes dynamiques d'apprentissage multi-agents et de dimensionnement statistique pour allouer les ressources dans les

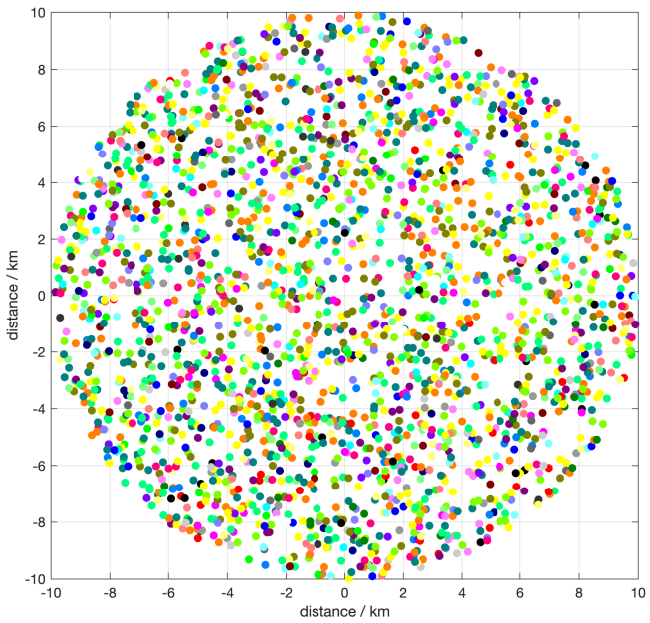

Figure 9: Répartition des nœuds de capteurs actifs dans une seule cellule avec différents choix de SF et de puissance d'émission

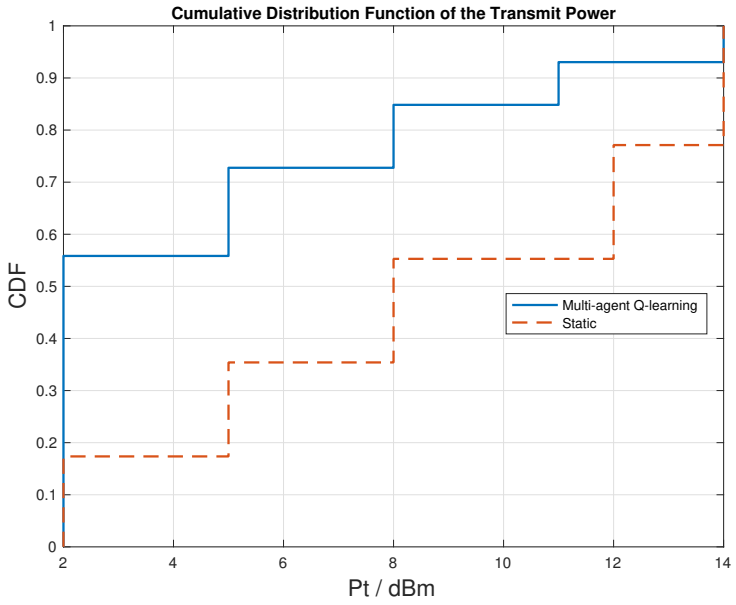

Figure 10: Fonction de distribution cumulative de la puissance d'émission

réseaux LoRa, respectivement. Chacune des deux approches différentes présente des gains significatifs, en tenant compte des différentes performances du réseau, notamment l'efficacité énergétique, la probabilité de coupure du réseau, le débit de données, l'efficacité spectrale, etc.

En conclusion, dans cette thèse, nous adoptons différentes méthodes, géométrie stochastique et algorithme d'apprentissage machine, pour résoudre les problèmes de contrôle de puissance et d'allocation des ressources dans le LPWAN. Nous considérons les caractéristiques et les limites du réseau LPWAN et essayons d'améliorer la qualité de service du réseau en termes d'efficacité énergétique, de débit de données, de délai d'accès, d'efficacité du spectre et de fiabilité des communications, etc. Pour les problèmes de dimensionnement des ressources dans les différents réseaux LPWA tels que les réseaux IoT basés sur l'OFDMA et les réseaux LoRa, nous étudions et améliorons les outils de dimensionnement statistique correspondants et l'algorithme d'apprentissage multi-agent respectivement.

Introduction and Thesis Outline

The Internet of Things (IoT) has been attracting lots of attention from the industry and research community. IoT has been called the third wave of the world's information industry after computers and the Internet. Low Power Wide Area Networks (LPWAN) is a class of innovative IoT technologies designed to provide IoT services with wide coverage, massive connection, low cost and low power consumption. LPWAN covers a wide range of IoT technologies, including licensed Narrow-Band IoT (NB-IoT), Long Term Evolution-Machine Type Communication (LTE-M), unlicensed LoRa, Sigfox, Weightless, IEEE 802.11 ah, etc. In this thesis, we focus on the radio resource planning and management in licensed network as well as the unlicensed LoRa networks. We refer to the stochastic geometry tools to analyse the network key performance indicator metrics by considering that the active sensor nodes and stations are distributed according to independent Poisson Point Process (PPP).

In the uplink of licensed OFDMA-based IoT networks, the radio-resource dimensioning is one of the major issues that should be addressed by the network planners. On one hand, the allocated bandwidth should be sufficiently large to support the traffic of the devices. On the other hand, the over-dimensioning is costly from an operator point of view and induces spectrum wastage. For this sake, we propose in this thesis statistical tools derived from stochastic geometry to evaluate, adjust and adapt the allocated bandwidth according to the network parameters. Different types of networks with a centralized and a distributed access are considered with SISO and advanced SIMO or MU-MIMO communications. In the uplink of non-licensed LoRa networks, the non-coordinated transmission induces high level of interference and affects highly the reliability of the network. To mitigate this high level of interference and to avoid the near-far problem, we propose first a stochastic geometry approach based on an adaptive multi-sub channel allocation policy. This policy spreads the chirps, depending on the distance, progressively onto one, two or four adjacent channels of 125 kHz each, while keeping the same power consumption and data rate. In the same context, we elaborate an algorithmic

approach based on multi-agent Q-learning to control the power and to allocate the spreading factor depending on the network parameters.

The organization of the thesis is presented as follows. The research context of IoT networks is presented in Chapter 1. Various applications of IoT are illustrated with examples. Different LPWAN technologies such as LoRa, NB-IoT and LTE-M are discussed. The 5G New Radio (NR) is also introduced to illustrate the direction of future IoT technologies. Then, the mathematical tools used in this thesis, including PPP and Q-learning algorithms, are described.

In Chapter 2, we address the issue of resource planning in the uplink of OFDMA-based licensed cellular IoT networks. We derive statistical tools to estimate the required bandwidth depending on the wireless network parameters such as the tolerated access delay, the antenna configuration, the network load and the density of the collectors. We also show the impact of deploying advanced MIMO transceivers with single user or multi-user on the network radio resources.

In Chapter 3, we focus on the unlicensed LoRa networks. LoRa adopts Chirp Spread Spectrum (CSS) modulation where 6 different Spreading Factors are assigned to responding nodes, depending on the location of the sensor nodes within a cell. With this spread spectrum technique, the signals sent by the active nodes are more resistant to interference. In this chapter, we propose an adaptive multi-channel allocation strategy for LoRa networks where multiple adjacent 125 kHz sub-bands are assigned to nodes located at the edge of SF regions to avoid the near-far problem. The interference in the LoRa network is statistically characterized by taking into account the correlation factors between different SF regions and multi sub-band sizes. The simulation results show the comparison between the adaptive sub-channel allocation strategy and the single channel allocation strategy.

In Chapter 4, machine learning tools are introduced to solve the resource allocation problems in a flexible and dynamic way for LoRa networks. Q-learning algorithm adopts off-policy Temporal-Difference (TD) methods for the agent to learn how to act optimally to control problems which gives outstanding performance in decision-making problems for many complicated scenarios. We apply multi-agent Q-learning algorithm to dynamically and jointly optimize the spreading factor allocation and power control for active sensor devices in the uplink communication for LoRa networks. The performance evaluation with respect to network reliability and power efficiency shows that our proposed multi-agent Q-learning algorithm outperforms the conventional static allocation policy.

Chapter 1

Research Background

Internet of Things (IoT) is an emerging topic which covers a huge scope of industries and technologies [1, 2]. In the past decades, the telecommunication technologies focused on the human-type communications. With the evolution of the society and industry, new needs requiring to interconnect objects and to ensure human-device and device-device communications emerged [3]. IoT networks should connect a huge number of devices while being low cost, with limited infrastructure, and featuring a very long device battery life. In order to address the requirements of IoT networks, a trade-off must be made between data rates, power consumption, and coverage, etc.

1.1 Introduction

Up to now, IoT is no more an advanced concept untouchable for us. It appears in our daily life everyday and everywhere, aiming to connect numerous objects, make information exchanging between electronic devices and human beings and going to change people's lifestyle. It can perform intelligent identification, positioning, tracking, monitoring and management of devices. For the industrial field, the advantages of IoT are enormous [4, 5]. It can help to improve work efficiency, reduce costs, reduce energy consumption, and able to apply machine learning technologies to act on the big data which is collected by thousands of IoT devices. It is not a big surprise that the IoT network has a large number of applications with great commercial potential, such as smart home, intelligent healthcare, smart grids, self-driving cars and so on [45, 46, 47, 48, 49, 50, 51]. With the rapid development of 5G and the continuous increase of connected devices, the IoT is currently undergoing fast evolution.

With the expansion of the industry, a variety of telecommunication technologies show up to meet

the challenges. There are plenty protocol choices existing now for developers or companies to choose for their products, meet the different requirements. For example, based on the cover range, there are long range IoT communications and short range IoT communications; Consider the different connective ways, there are critical IoT and massive IoT with licensed band and massive IoT with unlicensed band. Distinct protocols compete with each other and fit varied needs of data rate, energy cost, coverage range, reliability, mobility and stability, etc.

Table 1.1: IoT Connections (Billion)

IoT	2019	2025	CAGR[1]
Wide-area IoT	1.4	5.4	24%
Cellular IoT	1.3	5.0	25%
Short-range IoT	9.3	19.5	13%
Total	10.8	24.9	15%

[1] CAGR: Compound Annual Growth Rate
[2] Data reference [52]

According to *Ericsson Mobility Reports* [52], the IoT market is growing rapidly. In the report [53], it predicts there will be 20 billion IoT connected objects in 2023. In its latest report [52], based on the number of connected IoT devices worldwide, there was approximately 10.8 billion devices connected to IoT networks in 2019. This number will continue to grow in the coming years, with a prediction of 24.9 billion devices connected by 2025. The Compound Annual Growth Rate (CAGR) is 15%. As shown in Table 1.1, the number of IoT device connections is expected to increase in three main categories, including wide-area IoT, cellular IoT and short-range IoT.

The general architecture of IoT is depicted in Figure 1.1. IoT network usually contains a large number of connected devices such as sensors. It enable communications between different devices or between devices and the core network. Depending on the different use cases, these devices may be used for simple sensing of environmental parameters such as CO_2 concentration, air humidity, etc., or they may be used for more complex detection and execution of instructions. Nodes can be connected to the Internet either through a sink node (or gateway) for short-range to mid-range communications or directly through Low Power Wide Area (LPWA) communication technologies [54, 55, 56]. Nodes can transmit the collected information to a backbone network or to the cloud via an uplink. After

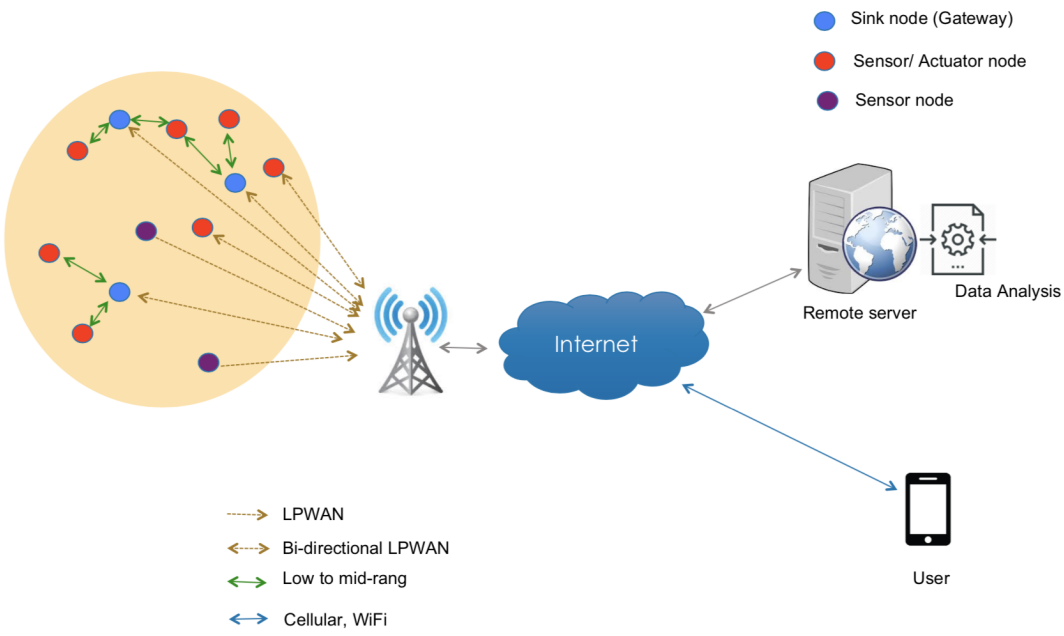

Figure 1.1: General Architecture of IoT Networks

the information being analyzed and processed remotely by the terminals, the appropriate operations can be transmitted to the device via a downlink. The downlink can also be used to acknowledge the reception of information. Authorized users have access to the data stored on the remote server.

IoT networks face many challenges [57, 58, 59, 60]. For example, the number of large-scale connections and the resulting high bandwidth requirements are a big challenge for it as we only have limited spectrum. Large amount of problems need to be solved in the system to improve the network service. The conventional IoT networks rely mostly on short-range communications with multi-hop communications schemes to connect the sensors to the local Gateway. Wide-range communication technologies are less complex to implement as they require only one-hop to connect the devices and the core network. They simplify the protocols and improve the communication efficiency. In addition, the coverage area of short-range communication technologies is insufficient compared to long-range technologies. For massive IoT network deployment, Low Power Wide Area Network (LPWAN) technologies are more suitable as they simplify the design of protocol stacks and reduce the delay of the message because it is no longer necessary to go through a gateway.

LPWAN technology meets the requirements of coverage and battery life of IoT networks. It of-

fers a long range of coverage while consuming very low energy consumption and sacrificing a small amount of data rates. Licensed LPWAN technologies, such as Narrow-Band IoT (NB-IoT) [14, 15] or LTE-M supported by 3rd Generation Partnership Project (3GPP) which can make software upgrades to existing cellular infrastructure, such as upgrading existing LTE base stations and GSM base stations. Since traditional cellular networks are expensive, consume a lot of power, and require expensive hardware and services, many network providers use unlicensed spectrum to develop their own wireless networks, for example, LoRa [12] and Sigfox. Licensed and unlicensed LPWAN technologies have high link budgets, long battery life and non expensive modules. The main difference lies in the ecosystem around these technologies.

The rest of the chapter is organized as follows. Section 1.2 provides illustrations of the IoT application. Section 1.3 presents a state of art on the LPWAN technologies studied in this thesis namely the NB-IoT and the LoRa. Section 1.4 and 1.5 give a brief summary on the multiple input multiple output techniques used in the new generation of wireless communications and the mathematical tools used in the thesis. Finally, Section 1.6 concludes this chapter.

1.2 IoT Use Cases Examples

It is undeniable that IoT plays an important role in our era. Essentially, different IoT technologies are used to transmit information from a sensor and eventually to an actuator. Various application scenarios are driving the development of different IoT technologies [6, 7, 8, 9, 10]. Increasingly enhanced IoT technologies are in turn driving further market expansion. In this section, we will present some general application scenarios for IoT technologies and attempt to summarize the basic internal requirements of IoT networks in these scenarios.

Figure 1.2 shows IoT application fields classified into business or consumer market, that include: 1) alerts related to the contexts of smart home, metering, medical sensing, monitoring of temperature, gas, water, carbon; 2) tracking and control applications, especially for autonomous driving, robotics and logistics; 3) wearable devices incorporated into motion detection, navigation systems, advanced textiles, and smart healthcare. The scenario classifications are often complex systems, composed of multiple parts, each of which is possible with different IoT technologies. In the meantime, the existing IoT technologies are not entirely distinct and the application scenarios to which they correspond are

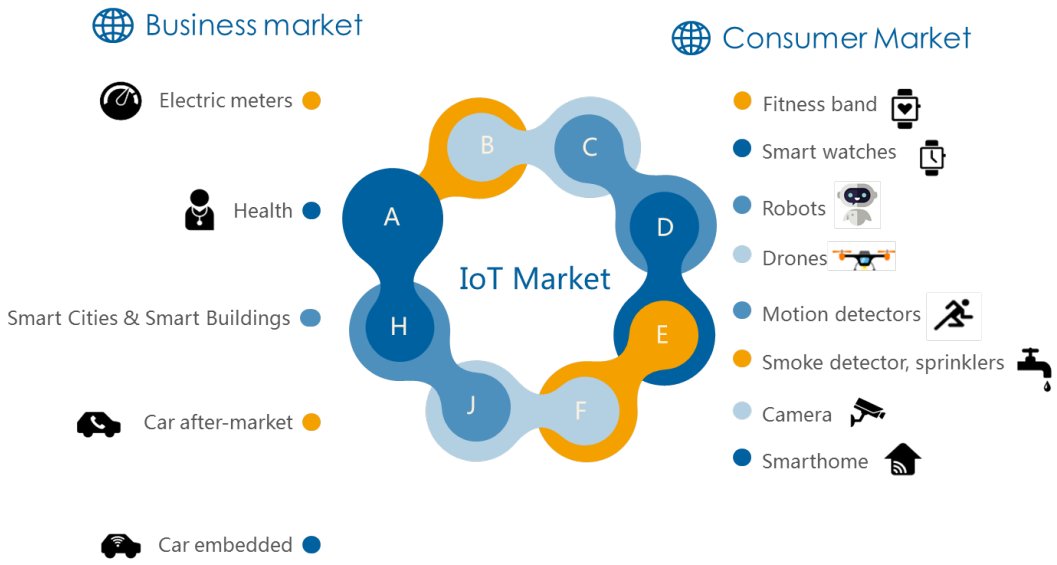

Figure 1.2: Internet of Things Applications

often intertwined. When considering a real-world scenario, there is often no absolute optimal technical choice, but rather a search for the appropriate IoT technologies. An IoT technology may be chosen for a particular case as long as it achieves desired objectives in terms of budget, data rate, coverage, Quality of Service (QoS), expected lifetime of the devices, etc. In most cases, it is not possible to achieve all the objectives but prioritize certain performance measures over others, making the system more efficient and reducing costs.

Autonomous driving

Autonomous driving is a complex technology that combines Artificial Intelligence (AI) and IoT technologies, requiring its communication systems to meet ultra-low latency and ultra-high reliability [61, 62]. With the concept of Industry 4.0 being proposed, industry digital transformation has been holding onto people's attention. Autonomous driving technology is an important part of it which has been catching people's eye. It can be foreseen that if Autonomous driving technology matures, it will bring many advances to industry and academia. It can further promote social and economic development, which in turn leads to technological innovation. The market and commercial value it creates will be enormous. Safety is the core concept of autonomous driving technology. The inter-vehicle communication system should be able to provide efficient, ultra-low latency and ultra-high reliability communication services. The vehicle has to proactively share and get real-time status

information about the surrounding vehicles and roads. Internet of vehicles should help to quickly analyze the global situation, coordinate the driving status of each vehicle or provide reliable operational alerts and dynamic information to the driver. If autonomous driving technology can meet the above conditions, it will be possible to break through the limits of human cognitive response and ensure road safety. In summary, the services that IoT networks should provide for this autonomous driving scenario include at least: mobility support and location support, uplink and downlink communications, real-time communications with ultra-low latency (guarantee latency to be 1 ms or less) [63], reliable communication links and High security and so on. Thanks to the development of 5G technology, its grand objective is to support three generic services with vastly heterogeneous requirements: enhanced Mobile Broadband (eMBB), massive Machine-Type Communications (mMTC), and Ultra-Reliable Low-Latency communications (URLLC) [64]. eMBB mainly corresponds to the scenarios of human-to-human communications. Different from eMBB, both mMTC and URLLC are IoT-related application scenarios. Among others, URLLC highly corresponds to the autonomous driving cases. 5G innovation helps to establish reliable IoT networks that may be able to achieve the harsh technical standards of autonomous driving in the near future.

Precision agriculture

Precision agriculture, or smart agriculture, is the future of the agricultural economy. It applies the IoT technologies to agricultural planting or breeding, combined with Internet technology, cloud computing, big data analysis, etc. to form an auxiliary system for agricultural production. It relies on various sensing nodes deployed in agricultural sites, IoT communication networks and cloud or computers or mobile devices to achieve intelligent sensing, early warning, decision-making, analysis and online guidance from experts in agricultural production environments. Precision agriculture can provide precision planting, visual management, and intelligent decision-making for agricultural production. Many IoT technologies are already being used in precision agriculture [65] [66]. Despite the variety of crops or livestock that farm operators need to manage, the basic requirements for IoT technologies in precision agriculture are very similar. The main focus is on data acquisition, data transmission, cost reduction and post-processing of data, etc. Here, IoT system is an automatic information detection and control system. Wireless sensor nodes should be installed in the farm to detect parameters such as soil moisture, temperature, air humidity, light intensity, plant nutrient content,

etc. In addition, a battery or solar-powered system and uplink/downlink are required to ensure that the collected data can be transmitted to analyze platform. Once the data has been intelligently analyzed by the platform or cloud, it shall be provided to the authorized user with various audio-visual or SMS alerts as required. In short, we can summarize some basic technical requirements for an IoT network for agriculture: low cost, sample devices, easy to operate (making it easy for everyone who is new to it), low power consumption, easy to set up the network, low data rate and high network robustness. Precision agriculture can significantly improve the efficiency of agricultural production and operations. This intelligent management not only solves the growing shortage of human resource, but also achieves a high degree of scale and factoryization of agricultural production. It improves the ability of agricultural production to respond to risks to the natural environment. With the continuous innovation of the IoT technologies, precision agriculture is sure to see more development.

1.3 State of the Art on LPWAN Technologies

LPWAN is a promising technology which is imperative for the expansion and development of IoT networks and their connectivity infrastructure [11]. It provides low-power, wide-area, low-cost IoT services for massively connected devices. It also has extremely long battery life expectations for the end devices. There exists different LPWAN technologies, such as LoRa, NB-IoT and LTE-M, etc. In this section, we will present the state of the art on LPWAN in detail. First, the difference between short-range and long-range communications will be explained. Then, specific LPWA technologies including LoRa, NB-IoT, and LTE-M will be described. The comparison between these three technologies will be analyzed in tabular form.

1.3.1 Short ranges vs long range communications

There are different types of communication technologies in IoT, which can be classified according to standards, frequency, coverage range and data transmission rate, etc. In terms of coverage, IoT communication technologies can be divided into short-range and long-range communication technologies. Roughly speaking, short-range IoT has a coverage radius ranging from several meters to a few hundred meters and depends on different short-range communication protocols. For long-range communications, it can easily reach several kilometers range. In rural areas, it generally performs better than in urban areas with respect to coverage. Short-range and long-range IoT communications differ

in terms of technical implementation, energy consumption and cost, etc. They can respond to different IoT communication needs. There are many short-range communication technologies and a wide range of applications, such as ZigBee, Bluetooth Low Energy (BLE) and Near Field Communication (NFC), etc [67]. In this thesis, we focus on long-range communication technologies, i.e. Low Power Wide Area networks (LPWAN). It contains licensed and unlicensed LPWAN communication technologies such as LoRaWAN, SigFox, Narrowband IoT (NB-IoT) and LTE-M, etc. Short-range IoT communications usually rely on multi-hops to connect the IoT devices to the backbone network through a local gateway.

1.3.2 LPWAN technologies

Different IoT applications have various specific requirements in terms of communication range, energy consumption, and cost effectiveness, etc. Compared to short-range IoT communications, LPWAN is a technology that meets both coverage and battery life needs. It offers longer coverage range, lower-power consumption, low-cost deployment options, but a drop in data rate [68]. The communication range is up to 40 km in rural areas and 10 km in urban areas[47], with a battery life of up to 10 years [69]. For deployment, the price of the device is controlled within the limit of $5 per device, the operator's subscription cost must be less than $1 per device per year [70].

LPWAN exploits both licensed and unlicensed frequency bands. For example, NB-IoT can coexist with Global System for Mobile communications (GSM) and LTE under licensed frequency bands (e.g., 900 MHz). LoRa operates on unlicensed Industrial Scientific Medical (ISM) bands (e.g., 868 MHz in Europe, and 915 MHz in the U.S.). The licensed IoT network are dedicated to critical IoT real time application requiring a certain level of QoS, security, reliability and latency. The unlicensed one is more suitable for massive IoT non critical and non real-time use-cases.

The most remarkable features of LPWAN are their wide range of coverage and low energy consumption. This long range of the LPWAN is made possible by a new design of the physical layer which allows considerably high receiver sensitivities. In addition, the data rate is sacrificed to achieve a longer transmission range. The data rate of LPWAN is limited to several hundreds or thousands of bits per second. To save energy and extend the battery life, LPWAN transmits small packets with a very low transmit power averaging 20 mW. Concerning network topology, most LPWAN adopts star topologies for the terminal devices connected to the core network. An end device is connected to a

collector (also referred as gateway) and then it acts as a bridge to the IP network [47, 69]. Thanks to the distinctive advantage of LPWAN, it has numerous applications of great commercial value. LPWAN fills the technology gap of cellular communications and short-range IoT communications based networks that require either high bandwidth or high power, or have a limited range of coverage.

1.3.3 LoRa Technology

LoRa technology is a wireless low-power wide-area communication technology. It defines two different layer designs, e.g. LoRa physical (PHY) layer based on Chirp Spread Spectrum (CSS) modulation and Medium Access Control (Mac) layer ALOHA protocols [71]. The PHY layer technique of LoRa is developed by Cycleo and acquired by Semtech [72]. Meanwhile, the MAC layer protocols are promoted by a non-profit association LoRa Alliance [12]. LoRa network provides long-range low-

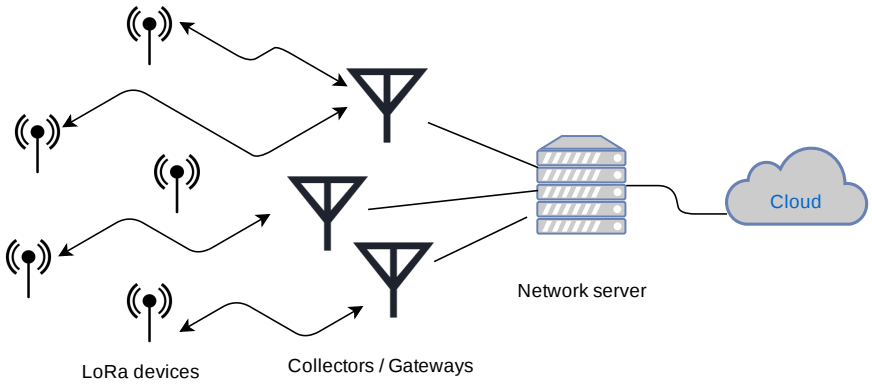

Figure 1.3: LoRa Network Topology

power communications. A number of coverage and capacity evaluation and analysis have been carried out, e.g. [73], [74], [75], [76]. The actual coverage range and network capacity depend on specific scenarios. Normally, in urban areas, the coverage radius is about 2 to 5 km. In rural areas, the coverage is extended to a radius of 5 to 15 km due to fewer obstacles. The data rate of LoRa network is about 0.3 to 5.5 kbps. LoRa network is deployed in a star topology. Each end node is connected to a collector/gateway. Then the terminal nodes can send information to the LoRa network server via the collector/gateway. The communication between the end nodes and the gateway is bidirectional and half-duplex. LoRaWAN protocol doesn't support direct communications between different end nodes. The architecture of LoRa network is shown in Figure 1.3. LoRa network operates on unlicensed ISM

band, e.g., 868 MHz in Europe, 433 MHz in Asia, and 915 MHz in the U.S.. By using CSS modulation, LoRa has a very low sensitivity down to −148 dBm [77].

Chirp Spread Spectrum

LoRa network adopts CSS modulation, which is a spread-spectrum modulation [17]. CSS modulation uses chirp pulses whose frequency varies linearly over the bandwidth to encode information. A chirp, also called a sweep signal, is a tone whose frequency increases or decreases with time. The increase one is called up-chirp and the decrease one is called down-chirp. Figure1.4 illustrates the comparison between up-chirp and down-chirp signals. CSS is commonly used in radar and underwater communications because of its high resistance to Doppler frequency shift. Since time synchronization is not required, it is also suitable for low data rate, low power LoRa systems. CSS increases the robustness of the system to against interference by spread the signal in the frequency domain [78]. It can also provide a scalable data rate for LoRa communications.

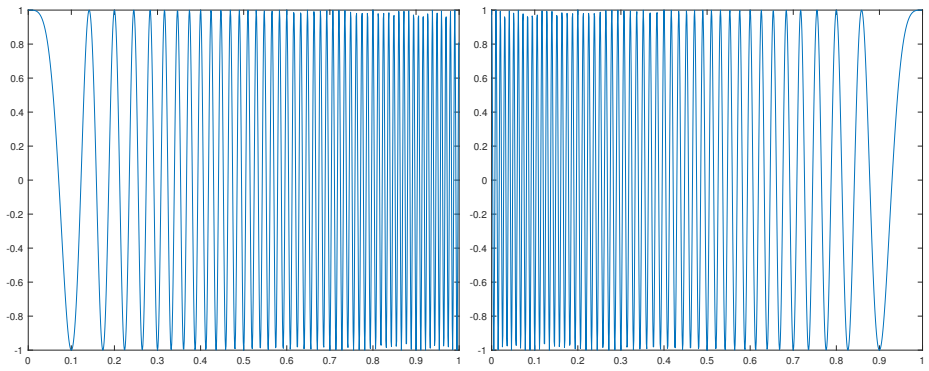

(a) Up-chirp (b) Down-chirp

Figure 1.4: Chirp Pulse Signal

In LoRa network, for a sensor node which is located far away from the collector, it suffers the collision caused by the other active sensors that simultaneously send information and are located closer to the collector. The CSS spreading technique can protect the cell edge sensor nodes from the nodes in the proximity of the network collector. It features 6 possible spreading factors (SF = 7 to 12) to the active sensors according to the receiver sensitivity and hence by the threshold communication ranges. Figure 1.5 illustrates the comparison between different spreading factors. Table 1.2 shows the corresponding SINR threshold according to the values of SF with the sub-bandwidth equal to 125

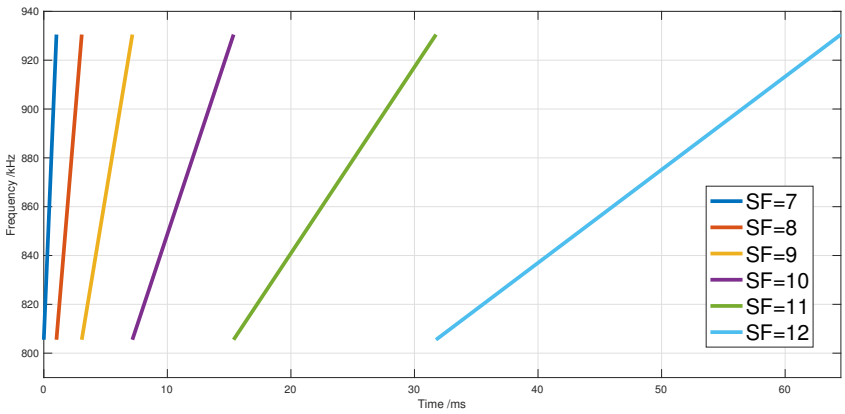

Figure 1.5: Comparison between different spreading factors (SF= $7 \sim 12$) in up-chirp case

kHz. For each SF value, it defines the number of raw bits that can be encoded by the symbol that holds 2^{SF} chips. With CSS modulation, each symbol transmits SF bits, has a time duration T and occupies a bandwidth B, such that,

$$2^{\mathrm{SF}} = T \times B \tag{1.1}$$

The symbol rate R_s (symbols/s) is,

$$R_s = \frac{1}{T} = \frac{B}{2^{\mathrm{SF}}}. \tag{1.2}$$

and the data rate R_b (bits/s) is,

$$R_b = \mathrm{SF} \times \frac{B}{2^{\mathrm{SF}}} \frac{4}{(4 + \mathrm{CR})} \tag{1.3}$$

with CR being the code rate. A high spreading factor better prevents transmission errors, but at the cost of a reduced data rate. LoRa network uses high spreading factors for the weak signal or the signal suffering high interference. Error correction bits are added to the transmit data to help the data become more resilient to the interference. These added redundant bits allow bits damaged during transmission to be recovered and corrected during the decoding process [79]. Theoretically, the more error correction bits are added, the easier it is to recover data corrupted by interference. But, adding too many bits leads to the shorten of battery life. In LoRa, it allows different code rates, e.g. 4/5, 4/6, 4/7 and 4/8 [80].

Table 1.2: SINR thresholds corresponding to different SF values

SF	7	8	9	10	11	12
SINR (dB)	−7.5	−10	−12.5	−15	−18	−21

1.3.4 LTE extensions for IoT: NB-IoT and LTE-M

In order to meet the requirements of IoT world, 3GPP has designed a set of solutions dedicated to connected objects. NB-IoT and LTE-M (also known as LTE-MTC, LTE-Machine Type Communications) are two LPWA technologies realized by 3GPP that provide narrow-band cellular IoT communications for connected devices. The specification of NB-IoT was frozen in 3GPP Release 13, in June 2016 [18]. LTE-M is specified by 3GPP in Releases 13 to 15 [18, 19, 20].

NB-IoT and LTE-M are both designed for low-power, wide-area IoT communications. They have a lot of specifications in common, for example, longer coverage range, low power consumption, easy network deployment, low cost (both hardware and subscription), etc. On the other hand, they also have a lot of difference in technique details. For example, compared to NB-IoT, LTE-M has higher uplink and downlink data rates. It also support VoLTE which is a standard for high-speed wireless voice communications. LTE-M is also compatible with the high-mobility scenarios. In this subsection, we will detail the specifications of NB-IoT and LTE-M.

Physical radio resources blocks

In LTE networks, Single-Carrier Frequency Division Multiple Access (SC-FDMA) and Orthogonal Frequency Division Multiple Access (OFDMA) are used for the uplink and downlink, respectively. These two techniques are derived from the Orthogonal Frequency Division Multiplexing (OFDM) technique that divides the large LTE bandwidth into small subcarriers of 15 kHz each. By this division, smaller bandwidth are used to transmit information between the User Equipment (UE) and the Base Station (BS). It helps reduce inter-symbol interference which is caused by echoes from its channels. Consequently, communication reliability is improved. The smallest transmission unit of this divided bandwidth is called the radio Resource Block (RB). It consists of 12 OFDM subcarriers with total bandwidth $B = 180$ kHz and with a duration of $T = 0.5$ ms. Within each RB duration of 0.5 ms, $N_s = 7$ (or $N_s = 6$) OFDM symbols with a short Cyclic Prefix (CP) (or long CP) are transmitted. For the short CP case, each RB contains 84 symbols that are carved from coded Quadrature Amplitude Modulation (QAM) constellation and carrying information bits.

NB-IoT

NB-IoT can be deployed directly on existing cellular networks, e.g., GSM, Universal Mobile Telecommunications System (UMTS) or LTE networks. The IoT terminals are connected to the operator's network by being equipped with wireless communication modules and SIM cards. It builds various types of centralized industrial applications.

In June 2016, the 72th meeting of the 3GPP Radio Access Network (RAN) Plenary was successfully held. The corresponding 3GPP protocol-related content has been approved by the RAN Plenary at the meeting, officially proclaiming this NB-IoT widely supported by the wireless industry. The standard core protocol has been fully completed after more than two years of research. Global operators finally have a proprietary IoT-based protocol. Products and solutions based on this protocol will be able to serve the IoT market in a wide range of industries. The successful completion of the standardization work also marks the upcoming commercial phase of NB-IoT.

NB-IoT offers significant advantages in wireless IoT communications. According to the survey in [81, 82, 83], they can be summarized in four main parts. First of all, it provides a wide range of coverage. It also improves indoor coverage. In the same frequency band, NB-IoT networks gain about 20 dB more than legacy General Packet Radio Service (GPRS) networks, increasing the coverage area. Secondly, NB-IoT has a strong ability to support a large number of connections. One sector of NB-IoT network can support thousands of connections with low latency and an improvement in sensitivity. In addition, it also supports very low power consumption. NB-IoT modules are usually battery-powered and can have up to 10 years of standby time. Last but not least, it is very low cost. A single connected module is expected to cost no more than $5.

To achieve better performance of frequency deployment with different wireless network services, NB-IoT defines three different modes of operation: 1) stand-alone mode, it is deployed on dedicated frequency bands, e.g. NB-IoT can occupy one GSM channel (the bandwidth is equal to 200 kHz); 2) in-band mode, within the occupied bandwidth of a wide-band LTE carrier; 3) guard-band mode, within the guard-band of an existing LTE carrier. For both in-band and guard-band modes, it uses one Physical Resource Block (PRB) of LTE networks with a bandwidth of 180 kHz. Figure 1.6 illustrates these three different modes.

NB-IoT network employs Quadrature Phase Shift Keying (QPSK)/Binary Phase Shift Keying

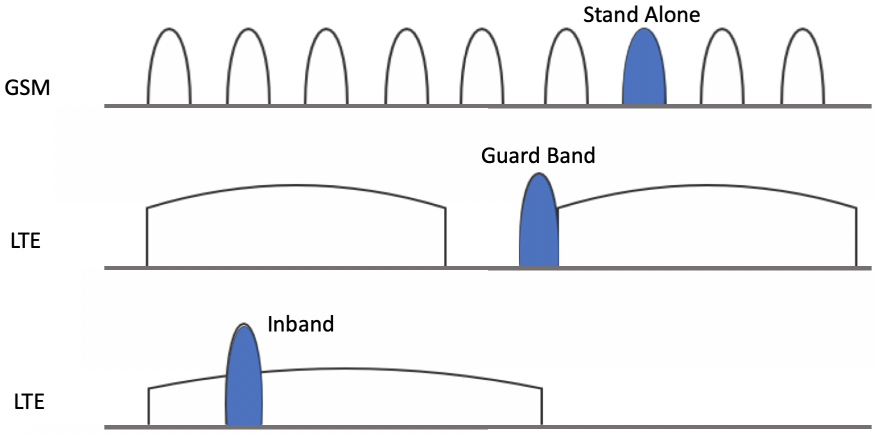

Figure 1.6: Three Different Deployment Modes of NB-IoT.

(BPSK) modulations. Both of them are digital phase modulations with good performance in anti-noise. The link budget of NB-IoT is about 150 dB. Based on existing LTE channels, NB-IoT has distinct channels for various usage purposes. For the uplink, there are Narrowband Physical Uplink Shared Channel (NPUSCH) and Narrowband Physical Random Access Channel (NPRACH). The former is used for uplink transmissions of dedicated data and the latter is for random access. For the downlink, Narrowband Synchronization Signal (NPSS/NSSS) is for time and frequency synchronization. Narrowband Physical Downlink Control Channel (NPDCCH) can transmit the uplink and downlink scheduling information. Narrowband Physical Broadcast Channel (NPBCH) can broadcast system access information.

LTE-M

LTE-M has salient features in wireless IoT communications, such as low-cost, long battery life and wide-coverage, etc. It is also carried out by 3GPP. Same as NB-IoT network, it can coexist with GSM and LTE systems by using the GSM or LTE spectrum. It can be easily deployed by upgrading an existing cellular network. The peak data rates of LTE-M is larger than 200 kbps. By using Maximum Coupling Loss (MCL), the maximum link budget of LTE-M can be up to 156 dB [16]. For uplink and downlink, LTE-M has a set of channels prepared for different transmission purposes. For the uplink, there are Physical Uplink Shared Channel (PUSCH), Physical Random Access Channel (PRACH) and Physical Uplink Control Channel (PUCCH). For downlink, Physical Downlink Shared Channel

Table 1.3: Comparison between Physical Features of LoRa, NB-IoT and LTE-M

Parameters	LoRa	NB-IoT	LTE-M
Standard	LoRaWAN	3GPP Release 13	3GPP Release 12-14
Modulation	CSS	QPSK / BPSK	BPSK / QPSK 16QAM / 64QAM
Frequency band	Sub-GHz ISM	Licensed	Lisensed
Bandwidth	125 kHz -500 kHz	180 kHz	180 kHz
Medium Access Control	ALOHA	SC-FDMA	SC-FDMA
Data rate	290 bps - 50 kbps	$\sim$ 50 kpbs	$\sim$ 1000 kbps
Duplex mode	Simplex Half-duplex Full-duplex	Half-duplex	Half-duplex Full-duplex
Power efficiency	Very high	Medium high	Lower than NB-IoT
Mobility	Better than NB-IoT	No mobility (only idle mode reselection)	High-mobility
Link budget	154 dB	164 dB	156 dB
Battery life	$>$ 10 years	$>$ 10 years	10 years
Voice	No	No	Yes

(PDSCH) is for mapping across sub-frames. Synchronization Signal (SS/SSS) is for time synchronization. Physical Broadcast Channel (PBCH) broadcasts the mapping information for terminal devices. Enhanced Physical Downlink Control Channel (EPDCCH) transmits control information. Table 1.3 shows the comparison between physical features of LoRa, NB-IoT and LTE-M technologies.

1.3.5 5G New Radio and IoT

5G is the fifth generation of mobile communication systems that has become a hot topic in the communications industry and academia. 5G innovation also opens up more possibilities for the IoT [21, 22, 23]. In this subsection, we will introduce the state of the art of 5G and how 5G New Radios (NR) will contribute to the development of IoT technologies. It provides an ecosystem and solid technical support to IoT. Recently, the request for mobile data has exploded rapidly. The existing 4G mobile communication systems can hardly meet future demands. There is therefore an urgent need to develop a new generation of communication systems that is 5G. According to the latest Ericsson Mobility Report [52], 5G is expected to have 2.6 billion subscriptions covering up to 65% of the world,Äôs population and generating 45% of the world,Äôs total mobile data traffic by 2025. The strong expansion of 5G is based on its innovation in technology, further improving the stability and reliability of communication networks, being able to carry a large amount of mobile data traffic and reducing network latency [84, 85]. This makes 5G suitable for more application scenarios. In the short future, smartphone will continue to be the epicenter of the fast-growing mobile data traffic. But it should not be overlooked that IoT will also rely on the 5G ecosystems to develop at high speed at the same time. The massive IoT technologies like NB-IoT continues to be rolled out around the world.

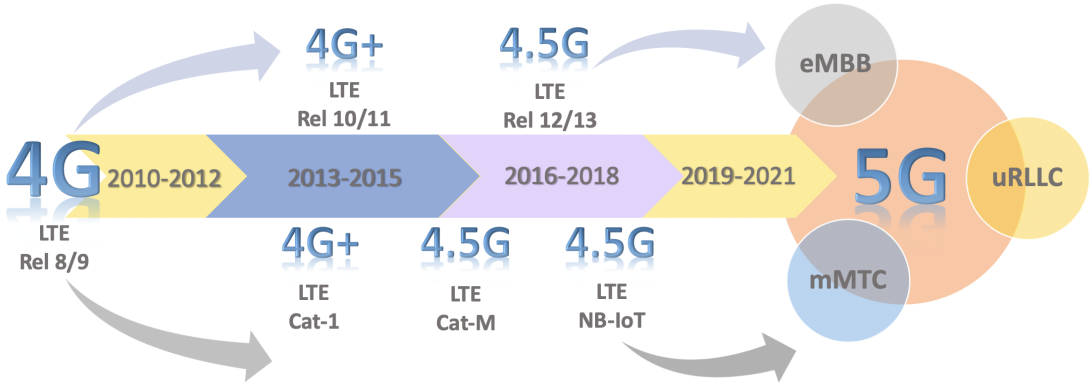

Figure 1.7: 3GPP Connectivity Overview

The establishment of the 5G standard has taken several years thanks to the efforts of multiple organizations. The International Telecommunication Union (ITU) defines the standardization for International Mobile Telecommunication (IMT). In June 2015, ITU has established the overall roadmap for the development of 5G mobile. IMT-2020 and beyond is proposed to meet the requirements for the development of 5G [86]. The 3rd Generation Partnership Project (3GPP) defines the technical solution to achieve the objective of the ITU. The IMT-2020 defines 3 main types of communications, massive Machine Type Communications (mMTC), critical Machine Type Communications (cMTC) and enhanced Mobile Broadband (eMBB) [24, 25]. mMTC is corresponding to massive IoT communications which should have wide area coverage, large number of devices, low equipment cost, low energy cost and high security. cMTC is prepared for critical IoT networks with high requirements in network latency, reliability and security. It is also referred as Ultra-Reliable Low-Latency Communications (URLLC). eMBB is designed for high data rate and low latency communications. The evolution of communication protocols is illustrated in Figure 1.7.

In order to successfully launch 5G, a complete preparation has been made in terms of an explosion of database services and machine-type communication (MTC). There are two different scenarios for 5G networks. One is Non,ÄìStandalone (NSA) 5G network and the other is Standalone (SA) 5G network. They also correspond to different periods of research and deployment. The early-drop is for NSA 5G networks. It addresses the most urgent deployment needs for enhanced Mobile Broadband (eMBB). In December 2017, the 3GPP standards defined 5G New Radio (NR) in NSA operation, enabling 5G NR deployments using existing 4G systems. It helps to accelerate specification to ensure a global ecosystem. After the early-drop, the main-drop is intended for SA 5G which should contain full standalone 5G support with 5G Core. The late-drop aims to speed up the migration. Specifications of all potential migration options should be contained.

The comparison of 5G and 4G networks may give us more intuitive experience on the performance of this new generation communication technologies. For the peak data rate, 5G network is set to handle 20 Gbit/s versus 1 Gbit/s for the 4G network. The user experience data rate is 100 Mbit/s for 5G and 10 Mbit/s for 4G. The network latency should be reduced to 1 ms for 5G while for 4G it is 10 ms. The connection density of 5G can be up to 10^6 number of objects/km^2, 10 times the 4G. In terms of energy consumption, 10 times longer battery life is ensured for low power devices in 5G compared to 4G. It is these tremendous improvements in network performance that ensure that

5G networks can enable applications with high communication requirements such as auto-drive and industrial automation. Compared to LTE, 5G NR has a much more complex numerology considering 5 possible sub-carrier spacing $\Delta f = 2^{\mu} \cdot 15$ kHz with $\mu = [0, 1, 2, 3, 4]$. The numerlogy $\mu = 0$ represents 15 kHz which is identical to LTE. NR has to cover a very wide operating frequency range, e.g., $f \leq 3$ GHz, 3 GHz $< f \leq 6$ GHz and millimeter wave (over 30 GHz) [87]. In short, 5G offers new opportunities for large-scale IoT connectivity by providing a higher level of technical support. It aims to enable IoT networks to connect more devices, improve network reliability, reduce power consumption, and more. Many technical details about 5G are worth mentioning, but were not addressed in this thesis.

1.4 Background on multi-antenna systems

The use of multiple antenna systems in wireless communication has been extensively studied in literature [88, 89, 90, 91, 92, 93, 94, 95]. In LPWAN networks, the use of multiple antennas is limited to the collector side due to low complexity of the sensor devices. In the following, we will review single-user and multi-user scheme using the Single Input Multiple Output (SIMO) in the uplink or Multiple Input Single Output (MISO) in the downlink. We focus on the uplink processing and the equivalent fading distribution.

1.4.1 Single-user communication

In this subsection, we describe the wireless communication system additive and multiplicative perturbation when a single user is multiplexed over one radio resource.

1.4.1.1 SISO system

The received signal on a given radio resource is modeled as,

$$y = \sqrt{\frac{P_t}{P_n + I}\, \alpha r^{-\beta} A_s}\, hx + (z + i)$$

where P_t is the transmission power, P_n is the noise power, I is the interference power, α the path-loss attenuation coefficient, β the path-loss exponent, A_s the shadowing power loss, h is the fading coefficient, x the transmitted signal, $(z+i)$ the normalized additive noise and interference with variance of 1. We considering the average behavior of the shadowing, and consider a non line-of-sight fading channel with h distributed as a complexe Gaussian random variable with zero mean and variance

equal to 1. We denote by $A_f = |h|^2$ the power attenuation coefficient that becomes exponentially distributed.

1.4.1.2 SIMO/MISO system

The SIMO/MISO system are used to enhance the reliability of the transmission by increasing the receiver/transmitter diversity. We assume an antenna configuration with n antennas at the collector side and a single antenna at the sensor side.

Uplink In this case, the n observations at the collector side are such that,

$$\mathbf{y}^{[n\times 1]} = \sqrt{\frac{P_t}{P_n + I}\,\alpha r^{-\beta} A_s}\;\mathbf{h}^{[n\times 1]} x + (\mathbf{z}^{[n\times 1]} + \mathbf{i}^{[n\times 1]})$$

1. **Antenna selection:** The receiver selects the best received signal among the n observation. The equivalent fading coefficient is $A_f = \max_{1\leq k\leq n} |h|^2$ and is distributed as the maximum among n random exponential variables.

2. **Maximum Radio Combiner (MRC):** We assume that the receiver is not aware of the instantaneous value of the interference at each branch. The used MRC projects the received signal into the unitary vector $\mathbf{u} = \mathbf{h}^{*[1\times n]}/\|\mathbf{h}^{*[1\times n]}\|$,

$$\langle \mathbf{u}, \mathbf{y}\rangle = \sqrt{\frac{P_t}{P_n + I}\,\alpha r^{-\beta} A_s}\;\|\mathbf{h}\| x + \langle \mathbf{u},\ \mathbf{z} + \mathbf{i}\rangle$$

   with $\langle .,. \rangle$ being the scalar product between two vectors. The equivalent received signal $\tilde{y}$ is,

$$\tilde{y} = \sqrt{\frac{P_t}{P_n + I}\,\alpha r^{-\beta} A_s}\;\|\mathbf{h}\| x + (\tilde{z} + \tilde{i})$$

   with $\|\mathbf{h}\|$ being the norm of the vector $\mathbf{h}$ and $(\tilde{z}+\tilde{i})$ the normalized additive noise and interference with variance of 1. The equivalent power attenuation fading coefficient for MRC is $A_f = \|\mathbf{h}\|^2$ that is distributed as the sum of n independent exponential random variables which is a chi-squared random variable with $2n$ degrees of freedom.

Downlink A single observation is obtained at the sensor side, such as,

$$y = \sqrt{\frac{1}{n}\frac{P_t}{P_n + I}\,\alpha r^{-\beta} A_s}\;\mathbf{h}^{[1\times n]} x^{n\times 1} + (z + i)$$

The antenna diversity is extracted at the transmitter side using space time coding schemes that will not be detailed in the scope of this thesis.

1.4.2 Multi-user communication

Another advantage of MIMO communications is the possibility to multiplex n_u users on the same radio resource. We assume that n_u users are multiplexed on a single radio resource with $n_u \leq n$.

1.4.2.1 Uplink

The received signal at the collector side is,

$$\mathbf{y}^{[n\times 1]} = \sum_{k=1}^{n_u} \sqrt{\frac{P_t}{P_n + I}\ \alpha\ r_k^{-\beta} A_{s,k}}\ \mathbf{h}_k^{[n\times 1]} x_k + (\mathbf{z}^{[n\times 1]} + \mathbf{i}^{[n\times 1]})$$

To decode the information of a user k, we use a multi-user Zero Forcing (ZF) that cancels the interference generated by the $(n_u - 1)$ users. The multi-user ZF projects the user channel vector $\mathbf{h}_k$ on the kernel $\mathbf{V}_k$ of the space composed of the other $\mathbf{h}_j$ with $j \neq k$, *i.e.*

$$\mathbf{V}_k^{[(n-n_u+1)\times n]} \perp \left[\ \mathbf{h}_{i\neq k}\ \right]^{n\times(n_u-1)}.$$

The information of user k is then decoded on a channel

$$\mathbf{h}_{e,k}^{[n\times 1]} = \mathbf{V}_k^{[(n-n_u+1)\times n]} \mathbf{h}_k^{[n\times 1]}$$

that is distributed as $(n - n_u + 1) \times 1$ Gaussian vector. To extract the remaining diversity, a MRC is used and the equivalent fading is a chi-squared random variable with $2(n - n_u + 1)$ degrees of freedom.

1.4.2.2 Downlink

In the downlink the collector should estimate the channel state of information between the collector and the n_u multiplexed users. A ZF precoder can be used to beam the signal in the direction of the sensor device.

1.5 Mathematical Tools Used in Thesis

In this thesis, we use mathematical tools to model wireless communication systems or for computation, to solve problems. The Poisson Point process, is used to model the distribution of active

sensors in an IoT network over a given range. We also use machine learning tools, such as Q-learning algorithm, to allocate power and data rates in LoRa networks. In this section, we will briefly introduce these two mathematical tools.

1.5.1 Poisson Point Process

Stochastic geometry is often used to model communication networks. It can efficiently simulate the location of nodes and analytically characterize the network performance metrics such as outage, capacity, interference modeling[27, 96, 97, 98, 99]. In the following, we shortly overview the main theorems and properties that will be used for further development in this thesis.

1.5.1.1 Poisson distribution

The Poisson distribution is the limit distribution of the binomial distribution. Suppose there is a series of binomial distributions $B(n, p_n)$, with a mean of λ, for any non-negative integer k (i.e. the probability of occurrence k times), there is,

$$\lim_{n\to\infty} b(k; n, p_n) = \lim_{n\to\infty} C_n^k p_n^k (1-p_n)^{n-k} = e^{-\lambda}\frac{\lambda^k}{k!} \tag{1.4}$$

1.5.1.2 PPP definition

Definition 1.1 ***Spatial PPP and Marked PPP*** *A random distribution of points Φ is called an homogeneous PPP of intensity λ if:*

- *The number of points of Φ in any set $\mathcal{S}$, $|\Phi(\mathcal{S})|$, is a Poisson random variable with mean λ times the surface of $\mathcal{S}$.*

- *The numbers of points $\Phi(\mathcal{S}_i)$ of Φ in disjoint sets $\mathcal{S}_i$ are independent random variables.*

An independent Marked Poisson Point Process is the collection of pairs $\tilde{\Phi} = \{(x_i, m_i)\}_i$, where $\{x_i\}$ is the set of points and $\{m_i\}$ the set of independent marks.

A PPP is characterized via the Poisson distribution. A spatial PPP Φ in the 2-dimension Euclidean space $\mathbb{R}^2$ is a Poisson random variable. A realization ϕ of a point process can be considered as a discrete

subset $\phi = \{x_i\} \subset \mathbb{R}^2$, then,

$$\phi = \sum_i \epsilon_{x_i},$$

where ϵ_x is the Dirac measure at x,

$$\epsilon_x(A) = \begin{cases} 0 & \text{if } x \notin A \\ 1 & \text{if } x \in A \end{cases}$$

Thus, the number of point of ϕ in a given area A is written as $\phi(A)$.

For $A \in \mathcal{B}$, in which $\mathcal{B}$ is the bounded Borel subsets of $\mathbb{R}^2$, the point process can be considered as a stochastic process, $\Phi = \{\Phi(A)\}_{A \in \mathcal{B}} \in \mathbb{N}$. Let Φ be a Poisson point process with intensity measure Λ, by means of its finite-dimensional distribution, Φ is defined as,

$$\mathbb{P}\left\{\Phi\left(A_1\right) = n_1, \ldots, \Phi\left(A_k\right) = n_k\right\} = \prod_{i=1}^{k} \exp\left(-\Lambda\left(A_i\right) \frac{\Lambda\left(A_i\right)^{n_i}}{n_i!}\right), \tag{1.5}$$

with $k \in \mathbb{N}^*$ and $\Lambda(dx) = \lambda dx$.

1.5.1.3 The point process of active nodes location

Assume that the network nodes localizations are independent and identically distributed (i.i.d), the service time is exponentially distributed with mean value v^{-1} and the time between two consecutive demands for service is also exponentially distributed with a surface density ρ. The point process of active nodes location is then a Poisson point process with intensity $d \wedge (x) = \rho \cdot v^{-1} dx$. For example, consider a massive IoT network with thousands of sensors. Each sensor is active n_a times per day, the mean service time is v^{-1} (s) and the inter-arrival rate is ρ per second and per km^2. The active sensors nodes form then a spatial PPP with intensity,

$$\lambda = \frac{n_a}{24 \times 60 \times 60}\ \rho\ v^{-1}.$$

1.5.1.4 PPP theorems

Theorem 1.1 (Distribution of the n^{th} neighboor) *Let Φ be a PPP of density λ defined in $\mathbb{R}^2$, and Let R_n be the random variable denoting the distance from a randomly chosen location up to the n-th point. The probability distribution function of R_n is,*

$$f_{R_n}(r) = \frac{2(\pi\lambda)^n}{(n-1)!} r^{2n-1} e^{-\lambda\pi r^2}. \tag{1.6}$$

For $n = 1$, this $f_{R_1}(r)$ is known as the contact distance distribution.

Theorem 1.2 (Campbell's formula) *Let Φ a Poisson point process on $\mathbb{R}^2$ with intensity $\wedge$ and $f : \Phi \to \mathbb{R}$ a measurable function. The random sum $F = \sum_{x\in\Phi} f(x)$ is a random variable with expectation:*

$$\mathbb{E}\left[\sum_{x\in\Phi} f(x)\right] = \int_{\mathbb{R}^2} f(x) \wedge (dx) \tag{1.7}$$

Theorem 1.3 (Slivnyak-Mecke Theorem) *Let Φ be a PPP with intensity measure Λ. For Λ almost all $x \in \mathbb{R}^d$*

$$P_x^!(\bullet) = \mathbf{P}\{\Phi \in \bullet\} \tag{1.8}$$

that is, the reduced Palm distribution of the Poisson p.p. is equal to its (original) distribution.

Theorem 1.4 (Probability Generating Functional (PGFL)) *Let Φ be a PPP of density λ and $f(x) : \mathbb{R}^2 \to [0, 1]$ be a real value function. Then,*

$$\mathbb{E}\left\{\prod_{x\in\Phi} f(x)\right\} = \exp\left(-\lambda \int_{\mathbb{R}^2} (1 - f(x))dx\right).$$

1.5.1.5 Properties of PPP

(1) Superposition of independent PPPs with intensities λ_k is a PPP and its intensity is $\sum_k \lambda_k$;

(2) Independent Thinning of a PPP with a constant factor p is a PPP and its intensity is $p\lambda$;

(3) By Slivnyak's theorem, adding a singleton to a PPP preserves the PPP.

1.5.2 Bennett's concentration inequality

Theorem 1.5 (Bennett's concentration inequality) *Let X_i be a bounded independent random variable $X_i < a$ with an average $m_x = \sum_{i=1}^N \mathbb{E}(X_i)$ and let $v_x = \sum_{i=1}^N \mathbb{E}(X_i^2)$. For $\alpha \geq 1$ the complementary cumulative distribution function of $X = \sum_{i=1}^N X_i$ is such that:*

$$\text{Prob}\{X > \alpha m_x\} \leq \exp\left(-\frac{v_x}{a^2} g\left(\frac{(\alpha - 1)m_x a}{v_x}\right)\right) \tag{1.9}$$

with $g(t) = (1 + t)\log(1 + t) - t$.

1.5.3 Q-Learning

Machine Learning (ML) is part of Artificial Intelligence (AI) which is considered one of the most promising techniques for the future. It analyzes and interprets patterns/structures of data to enable learning, reasoning, and decision-making without human interaction. Based on its great potential, ML attracts a lot of attention in many fields. There are different types of ML, e.g. supervised learning, unsupervised learning, Reinforcement Learning (RL), etc.

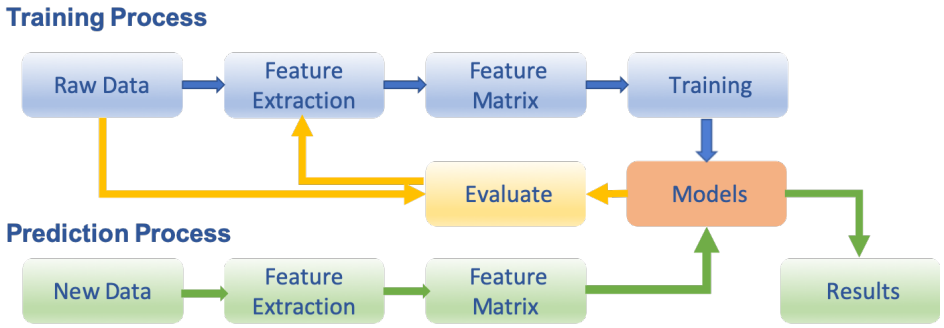

Figure 1.8: Supervised Learning Iterative Process

Supervised learning is a kind of ML which learns a model from a given set of training data, and when new data arrives, it can predict the outcome based on the generated model. The training set requirements for supervised learning include input and output which can also be said to be features and targets. Common supervised learning algorithms include regression analysis and statistical classification. Figure 1.8 illustrates the general process of supervised learning. Unsupervised learning refers to finding hidden patterns in unlabeled data, usually used for clustering. The main difference between supervised and unsupervised learning is that unsupervised learning can extract features and patterns on its own, whereas supervised learning requires tagged data set to start the extraction or classification. In contrast to supervised or unsupervised learning, reinforcement learning relies on the interaction between the agent and the environment, which uses positive/negative rewards to enable the agent to respond to different states. The structure of reinforcement learning is shown in Figure 1.9.

In this thesis, we applied the Q-learning algorithm to solve resource management problems in unlicensed LoRa networks. The Q-learning is a model-free RL algorithm and follows the framework of RL. Q represents the action value function $Q(s, a)$ (The action value function is also called the Q-function where s denotes the state, a denotes the action) that returns the reward to the agent.

Q-learning is a Temporal-Difference (TD) learning algorithm. TD learning algorithms are suitable for solving the model-free reinforcement learning problems. The learning reference of classical model-free RL tools consists only of scalar rewards. A lot of information contained in state transition tuples is ignored during the learning process [100]. In TD algorithms, the agent learns how to solve the RL task using temporal-difference data generated by the time steps in the environment. Compared to the classical RL algorithm, it takes full advantage of this information and solves the RL problem more accurately and efficiently. There are two common TD algorithms, e.g. the on-policy Sarsa algorithm and the off-policy Q-learning algorithm. The policy followed by the Sarsa algorithm for action selection is the same as that followed for the update of the action value function. The Q-learning algorithm, on the other hand, uses a different policy in updating the action value function from the one followed in selecting the action. Thus, the first is called on-policy and the second is called off-policy.

In the Q-learning algorithm, it is essential to keep updating the Q-function as follows:

$$Q\left(s,a\right) = Q\left(s,a\right) + \sigma \left\{ \underbrace{\underbrace{r(s,a) + \gamma \max_{a \in A} Q\left(s',a'\right))}_{\text{TD Target}} - Q(s,a)}_{\text{TD Error}} \right\}, \tag{1.10}$$

where $\sigma \in [0,1]$ is a learning rate. When the action a is performed with the state s, the agent earns a reward $r(s,a)$ and the environment turns to a new state s'. Besides, a' represents the next possible action chosen by the agent. γ is the discount factor which is a constant, $\gamma \in [0,1]$.

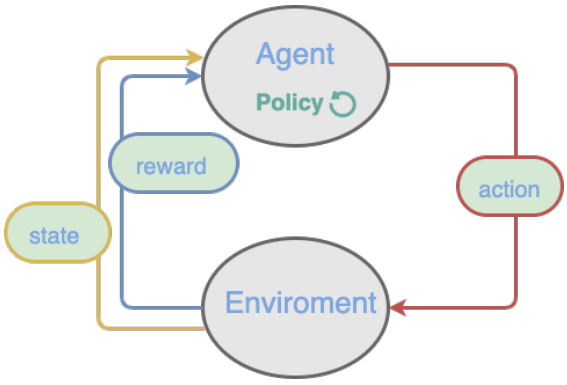

Figure 1.9: Reinforcement Learning Framework

The classical Q-learning algorithm, as shown in the Figure 1.9, typically has only one agent and

one environment that interact and then update the Q-function in the agent. Multi-agent Q-learning, as its name suggests, it adopts multiple agents in an environment-agent interaction scheme while maintaining a single environment. In [101], the authors present a survey on the multiple agent RL algorithms including the multi-agent Q-learning algorithm. The agents interact with environment at the same time. Through the training, each agent is able to find a policy to achieve its goal. Compared to the single-agent Q-learning algorithm, the multi-agent Q-learning algorithm is more efficient and more complex. It can be used to solve more complicated RL problems by dividing a big problem into several smaller, related parts. Each agent has a choice between a relatively smaller number of possible actions, and by observing changes in the state of the environment, it can indirectly acquire the impact of the actions of other agents on the environment. It would not be necessary to increase memory exponentially to accommodate all global scenarios in a single agent, which is often more economical.

1.6 Conclusion

In this chapter, we have situated the IoT context of this thesis by introducing the IoT market, the IoT low power wide area technologies as well as the mathematical tools used to model the IoT network. We first presented the development process, the growth rate and some of the challenges facing IoT. Then, we gave some insight into applications of IoT technology through several examples, such as IoT applications in autonomous driving, precision agriculture, etc. We highlight some specifications of multiple antennas systems, LPWAN technologies, namely LoRa, NB-IoT and LTE-M technologies and compared them in various aspects. The 5G NR is also presented to illustrate the direction of IoT technology development in the 5G era. The mathematical tools used in this thesis to model the IoT network, the PPP and Q-learning techniques, are finally described.

Chapter 2

Statistical Dimensioning for Low Access Delay in Licensed OFDMA IoT Networks

In this chapter, we focus on radio resource planning in the uplink of licensed Orthogonal Frequency Division Multiple Access (OFDMA) based IoT networks. The average behavior of the network is considered by assuming that active sensors and collectors are distributed according to independent random Poisson Point Process (PPP) marked by channel randomness. Our objective is to statistically determine the optimal total number of Radio Resources (RRs) required for a typical cell. On one hand, the allocated bandwidth should be sufficiently large to support the traffic of the devices and to guarantee a low access delay. On the other hand, the over-dimensioning is costly from an operator point of view and induces spectrum Laplace transformwastage. For this sake, we propose statistical tools derived from stochastic geometry to evaluate, adjust and adapt the allocated bandwidth according to the network parameters, namely the required Quality of Service (QoS) in terms of rate and access delay, the density of the active sensors, the collector intensities, the antenna configurations and the transmission modes. The optimal total number of RRs required for a typical cell is then calculated by jointly considering the constraints of low access delay, limited power per RR, target data rate and network outage probability. Different types of networks are considered including Single Input Single Output (SISO) systems, Single Input Multiple Output (SIMO) systems using antenna selection or Maximum Ratio Combiner (MRC), and Multi-User Multiple Input Multiple Output (MU-MIMO) systems using Zero-Forcing decoder.

2.1 Introduction

Cellular licensed IoT technology has been an emerging and evolving Low Power Wide Area (LPWA) technology which provides long range, low power, and low cost connectivity for IoT devices [102]. It can be deployed in existing cellular networks from which it inherits many of the features that determine its behavior [103], such as Long Term Evolution (LTE) networks.

With the booming development of Fifth Generation (5G) technology, evolutions of cellular IoT standards have been proposed and put into practice by 3rd Generation Partnership Project (3GPP) [14]. It will further promote the development of IoT technology. 5G technologies primarily include Non-Standalone (NSA) and Standalone (SA) technologies. The former is the early-drop technology that operators plan to connect New Radio (NR) 5G base stations (called gNB) to the Fourth Generation (4G) core network. Until NR 5G connectivity migrates to the native 5G Core network (5GC) mode which means shifts to SA mode [104]. For the 4G and NSA 5G connections, Orthogonal Frequency Division Multiple Access (OFDMA) technology can be employed to enable multi-carrier transmission and network access. OFDMA can take advantage of multi-user diversity and robustness to multipath fading for the uplink communications. Moreover, it also provides more degrees of freedom for resource allocation and facilitates multiplexing and diversity gains [105, 106]. Due to the limited spectrum of licensed IoT, as the network gradually scales up, one of the key issues we face is how to effectively use these resources to support large-scale IoT devices. In addition, the cost of IoT has been a major concern, and the improvement of spectrum efficiency can help reduce the cost of cellular IoT networks.

In this chapter, we focus on the uplink of OFDMA-based cellular IoT networks with multiple antennas receiver. The average statistical behavior of the network is considered where the active sensors and collectors are randomly distributed in a given area according to a random Poisson Point Process (PPP). The randomness of the wireless channel is considered as a mark of the Poisson position and results from stochastic geometry using marked PPP as in [26, 27, 28, 29, 30, 31, 32, 33, 34, 35, 36, 37, 38] will be invoked. These tools were investigated in [107, 108, 109, 110] to compute an upper-bound on the resource outage probability in a cellular network considering random PPP marked by the random fading. Unlike the previous contributions in [107, 108, 109, 110] where the network is considered as noise limited, this study is more general as it takes into account the impact of interference on the statistical dimensioning.

This chapter considers both the single user communication as well as the MU-MIMO communications where multiple users can be scheduled over one RR. It introduces indeed a new criterion for performing dimensioning based upon low delay access. We provide also a comparison between the energy consumption of the different considered transmission modes.

We consider first Single-User (SU) communication with receiver diversity transmission modes such as antenna selection and the Maximum Ratio Combining (MRC). Next, we consider Multi-User (MU) transmission where a distance-based scheduling algorithm is proposed with neighboring sensors nodes that are scheduled on the same RR. The inter-user interferences are cancelled using a Zero-Forcing decoder. The remaining diversity when not all the degrees of freedom are consumed is extracted using a MRC. The number of RR required by a single node in the SU case of by a group of nodes in the MU case is limited by the lowest Modulation and Coding Scheme (MCS). We define the network outage as the event that occurs when the number of request RRs exceed the number of the available ones. Whenever this event occurs, the sensor node has to delay its transmission to the next Time Transmission Interval (TTI). Our goal is to determine the number of required RR to be allocated at the network side depending on the network load and the collector density in order to guarantee that the average delay access does not exceed a preset threshold.

The rest of the chapter is organized as follows. We introduce in Section 2.2 the network model and its properties. In Section 2.3, we review first the dimensioning concentration inequality used in [108, 109, 110, 111] that provides an upper-bound on the network outage probability and hence on the number of required RR. This upper-bounds depends on the average total number of required RR that we computed for the single-user case as in [111] and for the multi-user case that we introduce in this chapter. We also characterize in each case the power distribution. The results presented in this section are general and are not related to the transmission mode fading distribution observed by the collector or the statistical behavior of interference that are characterized in Section 2.4. Numerical results are provided in Section 2.5 to compare the transmission mode in terms of required RRs and energy consumption in function of the collectors density and the average required delay. Finally, Section 2.6 concludes the paper.

2.2 IoT Network Model

We consider a sensor network depicted in which a random number of active nodes sensors and collectors are distributed in a given area $\mathcal{A}$ according to two independent homogeneous PPP with intensities λ_a and λ_b. We assume that the sensors are equipped with a single antenna and that the collector is equipped with n_r receiver antennas. We assume that a sensor is active n_a times per day, the mean service time is ν^{-1} (s) and the inter-arrival rate is $\frac{n_a}{24\times60\times60}\ \rho$ per second and per km^2. The active sensors nodes form then a spatial PPP Φ_a with intensity

$$\lambda_a = \frac{n_a}{24 \times 60 \times 60}\ \rho\ \nu^{-1}.$$

The frequency reuse pattern in the network is equal to 1. At a given collector situated at $y_0 \in \Phi_b$, the received power on a given Radio Resource (RR) from a sensor $x \in \Phi_a$ transmitting with power P_{RR} (mW per RR) is computed as, $P_r(y_0, x) = P_{\text{RR}}\ \alpha\ |y_0 - x|^{-\beta}\ A_f$ where α and β are respectively the attenuation factor (that includes the average shadowing) and the path-loss exponent that are computed from the Okumura-Hata model, A_f is the fading coefficient with distribution depending on the antenna configuration and the used transmission mode (single-user or multi-user). The sensor nodes are considered as static and the fading channel is considered as flat during the transmission. The Channel State Information (CSI) is only available at the receiver side and not at the transmitter side. Each sensor is connected to the collector on which the average received power (by averaging over the fading and the shadowing) is the highest. This is equivalent to connect the sensor to the nearest collector. Assuming a collector y_0, the set of the sensors connected to this latter is defined as $\Phi_c(y_0) = \{x \in \Phi : \forall y \in \Phi_b - \{y_0\} : |y_0 - x| < |y - x|\}$. Nodes transmitting in the same frequency band generate additive interference with power

$$I\left(y_0\right) = \sum_{x_i \in \Phi_I(y_0)} P_{\text{RR}} \alpha\, |y_0 - x_i|^{-\beta}\, A_{f,i}, \tag{2.1}$$

with

$$\Phi_I\left(y_0\right) = \cup_{y \in \Phi_b, y \neq y_0} \left\{x_i : x_i \text{ randomly selected in } \Phi_c(y)\right\}. \tag{2.2}$$

The received SINR at the given collector y_0 is,

$$\text{SINR}(y_0, x) = \frac{P_{\text{RR}}\ \alpha\ |y_0 - x|^{-\beta}\ A_f}{P_n + I(y_0)} \tag{2.3}$$

with P_n being the random noise with mean power of $\bar{P}_n = KTB$ where K is the Boltzmann's constant $K = 1.379 \times 10^{-23}$ W Hz^{-1} K^{-1}, T the absolute temperature in kelvins $T = 290$ K and B the bandwidth. The power of the random noise power is characterized by its Laplace transform in [27],

$$\mathcal{L}_{P_n}(s) = \mathbb{E}\left[e^{-sN}\right] = \frac{1}{s\bar{P}_n + 1}. \tag{2.4}$$

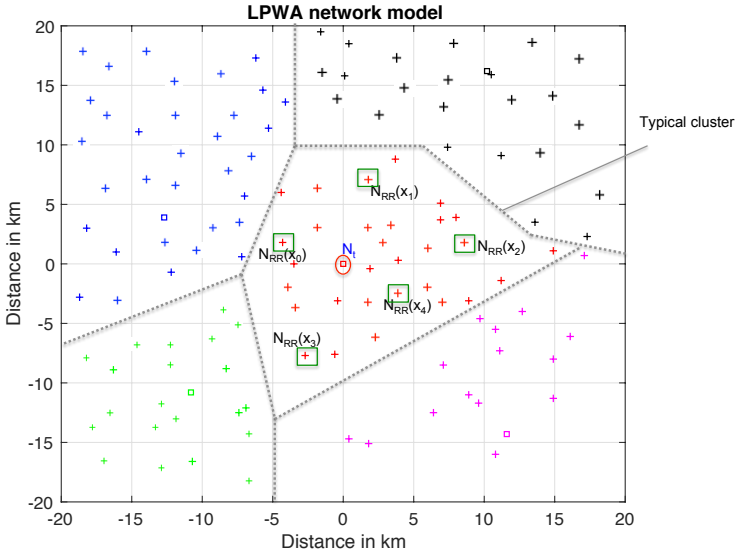

Figure 2.1: Network model: typical cell and active nodes

Due to Slivnyak-Mecke Theorem in [27], the statistical behavior in the PPP remains unchanged when adding a collector at the center of this region. This defines the typical cell centered at the origin $\Phi_c(0)$ as illustrated in Figure 2.1. The typical clusters properties are reviewed in Proposition 2.1.

Proposition 2.1 (Typical cell properties) *The typical cell average number of sensors is,*

$$N_s \triangleq \mathbb{E}\left[\sum_{x\in\Phi_a} \mathbb{1}_{\{x\in\Phi_c(0)\}}\right] = \frac{\lambda_a}{\lambda_b} \tag{2.5}$$

The probability distribution function of $r = |x|$ the distances between $x \in \Phi_c(0)$ and the o collector is,

$$f(r) = 2\pi\lambda_b \exp(-\lambda_b \pi r^2). \tag{2.6}$$

The average radius of the typical cell is $1/(2\sqrt{\lambda_b})$.

Proof: We provide for completeness the proof in Appendix 2.7.1. □

2.3 Statistical Dimensioning in the Uplink of IoT Networks

Given the density of collectors in the network, we propose a statistical method for resource planning in the uplink of cellular IoT networks. We assume the network access is an OFDMA and consider only the Narrowband Physical Uplink Shared Channel (NPUSCH) which carries the uplink user data and uplink control information. In an NB-IoT network, identical to the LTE network, the smallest block of radio resource elements that can be invoked is called the Resource Block (RB) or Radio Resource Block (RRB). It contains several OFDM symbols. Each RR corresponds to 180 kHz in the frequency domain and 0.5 ms in the time domain. For the single-user and multi-user cases, our main objective here is to statistically determine the total number of required RRs to minimize the occurrence of the network outage event. When the total number of RRs required is larger than the number of RRs available on the collector side, this is considered as an outage event.

2.3.1 Dimensioning objectives in a typical cell

In the typical cell illustrated in Figure 2.1, the collector o allocates according to the level of the received SINR, 1 to $N_{\max}$ RRs to the sensor node in order to achieve its target data rate C_0. The required number of RRs is,

$$N_{\mathrm{RR}}(x, A_f, I, P_n) = \sum_{k=1}^{N_{\max}} k \times \mathbb{1}_{\left\{ \mathrm{SINR}(x) \in [\gamma_k \, ; \, \gamma_{k-1}[\right\}}. \tag{2.7}$$

with γ_k being the threshold SINR required to achieve a target rate of C_0/k within a single RR and $\gamma_0 > \gamma_1 > ... > \gamma_{N_{\max}}$ and $\gamma_0 \to \infty$. Note that γ_0 (respectively $\gamma_{N_{\max}}$) is the threshold SINR to decode the highest (respectively lowest) Modulation and Coding (MCS) scheme. If $\mathrm{SINR}(0, x) < \gamma_{N_{\max}}$, the sensor will not be able to decode the lowest MCS and the collector does not attribute any RR to this user. This event of having insufficient SINR occurs with probability [1],

$$\mathbb{P}_{\mathrm{off}} = \mathrm{Prob}\{\mathrm{SINR}(0, x) < \gamma_{N_{\max}}\}.$$

By setting

$$A_{f,k} = \gamma_k \alpha^{-1} r^{\beta} (P_n + I), \qquad \forall 1 \leq k \leq N_{\max}, \tag{2.8}$$

[1] We intentionally do not refer to this probability as outage to avoid confusion with the network outage probability.

with $A_{f,0} = \infty$ the threshold fading to achieve a rate $C_k \in [C_0/k \ ; \ C_0/(k-1)]$ over one RR, the number of RR can be re-written as,

$$N_{\mathrm{RR}}(x, A_f, I, P_n) = \sum_{k=1}^{N_{\max}} k \times \mathbb{1}_{\left\{A_{f,k} \leq A_f \leq A_{f,k-1}\right\}}. \tag{2.9}$$

The total of required RR in this typical cell depicted in Figure 2.1 is,

$$N_{RR,t}(0) = \sum_{x \in \Phi_c(y_0)} N_{RR}(x, A_f, I, P_n).$$

The network is in outage if,

$$\mathbb{P}_{\mathrm{out},c}(N_t) = \mathrm{Prob}\{N_{RR,t}(0) > N_t\}.$$

In order to ensure an optimized network dimensioning, the number of total radio resources N_t that ensure a network outage probability of $p_{\mathrm{th},n}$, should be found. Using the concentration inequality, the typical cell outage probability is upper-bounded by,

$$\mathbb{P}_{\mathrm{out},c}(N_t) \leq \mathbb{P}_{\mathrm{sup}}(N_t),$$

where

$$\mathbb{P}_{\mathrm{sup}}(N_t) = \exp\left(-\frac{v_N}{N_{\max}^2} g\left(\frac{N_{\max}(N_t - m_N)}{v_N}\right)\right),$$

with

$$m_N = \mathbb{E}\Big[\sum_{x \in \Phi_c(o)} N_{RR}(x)\Big], \tag{2.10}$$

$$v_N = \mathbb{E}\Big[\sum_{x \in \Phi_c(o)} N_{RR}^2(x)\Big], \tag{2.11}$$

the function $g(t) = (1+t)\log(1+t) - t$ and $N_t > m_N$. By setting a threshold $p_{th,n}$ on the network outage,

$$N_t = m_N + \frac{v_N}{N_{\max}} g^{-1}\left(\frac{N_{\max}^2}{v_n} \log\left(\frac{1}{p_{\mathrm{th},n}}\right)\right).$$

2.3.2 Average delay and choice of the network threshold

In this subsection, we compute the average delay to connect the sensor device to the network independently of its transmitting rate. This average delay should not exceed a maximal delay $\tau_{\max}$ that we assume proportional to the Time Transmission Interval (TTI). As long as the sensor is not

accepted by the network due to the lack of resource, a new trial will be performed after TTI. We assume that the probabilities of being rejected after $i \times$ TTI are independent and are equal to $\left(\mathbb{P}_{\text{out},c}(N_t)\right)^i$. The average delay to access to the network is hence,

$$\bar{\tau} = \left(\sum_{i=0}^{\infty} i \times \text{TTI} \times \left(\mathbb{P}_{\text{out},c}(N_t)\right)^i\right) \leq \left(\sum_{i=0}^{\infty} i \times \text{TTI} \times p_{th,n}^i\right).$$

This expression can be simplified to,

$$\bar{\tau} \leq \text{TTI} \frac{p_{th,n}}{(1-p_{th,n})^2}.$$

By choosing $p_{th,n}$ such that

$$\text{TTI} \frac{p_{th,n}}{(1-p_{th,n})^2} \triangleq \tau_{\max}, \tag{2.12}$$

we make sure that the average delay in the network does not exceed $\tau_{\max}$. By letting $\kappa = \tau_{\max}/\text{TTI}$, the network threshold is,

$$p_{th,n} = \frac{(2\kappa+1) - \sqrt{1+4\kappa}}{2\kappa} < 1. \tag{2.13}$$

2.3.3 Expressions of m_N and v_N

In this subsection, we derive the expressions of m_N and v_N in (2.10) and (2.11) considering the single-user and multi-user cases. We recall that all sensor devices are equipped with a single antenna and the number of antennas at the collector is n_r. The distribution of the fading coefficient in (3.28) will be specified in the next section depending on the antenna configuration and transmission mode.

2.3.3.1 Single-user case

Proposition 2.2 (Single-user case) *The expressions of m_N and v_N are,*

$$m_N = N_s \times \sum_{k=1}^{N_{\max}} k \times \mathbb{E}_r \, \mathbb{E}_{I,P_n} \, \mathbb{E}_{A_f}[\mathbb{1}_{\{A_{f,k} \leq A_f < A_{f,k-1}\}}] \tag{2.14}$$

$$v_N = N_s \times \sum_{k=1}^{N_{\max}} k^2 \times \mathbb{E}_r \, \mathbb{E}_{I,P_n} \, \mathbb{E}_{A_f}[\mathbb{1}_{\{A_{f,k} \leq A_f < A_{f,k-1}\}}] \tag{2.15}$$

with $N_s = \lambda_a/\lambda_b$ the average number of sensors as shown in (2.5), and $\mathbb{E}_r[(.)] = \int_0^\infty (.) f(r) dr$ with $f(r)$ defined in (3.1).

Proof: Please refer to Appendix 2.7.2. □

Note that (2.14) can be interpreted as following: $\frac{\lambda_a}{\lambda_b}$ is the average number of sensor in the typical cell; Each sensor requires each 1 to $N_{\max}$ RRs depending on their distance to the collector, the channel conditions and the additive interference and noise.

2.3.3.2 Multi-user case

In the multi-user case, we assume that each RR is shared by n_u users simultaneously as depicted in Figure 2.2. To cancel the inter-user interference, the collectors uses a Zero-Forcing (ZF) decoder. The equivalent fading observed by each sensor j device is denoted by $A_f^{(j)}$ having a distribution that will be specified in the next section.

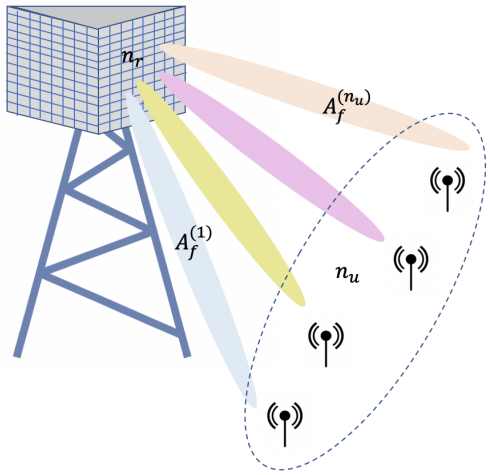

Figure 2.2: MU MIMO: n_u users are simultaneously scheduled on the same radio-resource

Distance based multi-user scheduling scheme: In this scheme, the active users are sorted according to their proximity to the collector into different groups of n_u users, each *independently* of their fading. As shown in Figure 2.3, the first group contains the n_u nearest neighbor to the typical collector, the second group the $(n_u+1)^{\text{th}}$ to $2n_u^{\text{th}}$ collector neighbor and so on. We adjust the number of allocated RRs to the furthest user from the collector in each group independently of the fading coefficient experienced by other users. The furthest node x in each group i is the $i \times n_u^{\text{th}}$ neighbor of the collector and it corresponds to the radius of the ball $\mathcal{B}(|x|)$ with radius $|x|$ containing $i \times n_u$ nodes.

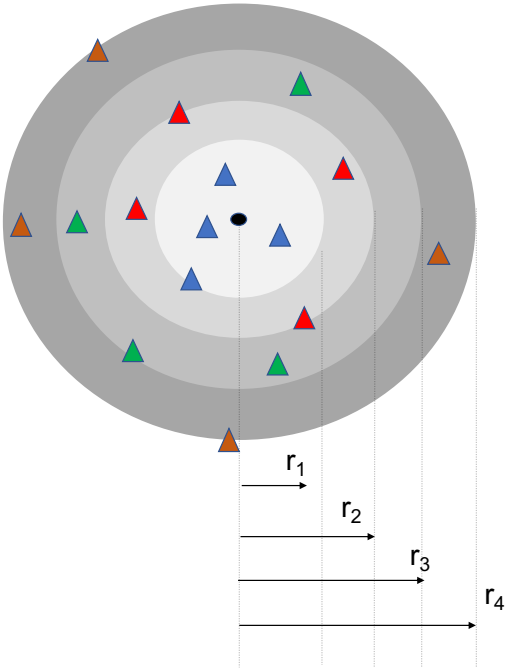

Figure 2.3: Illustration of the scheduling with $n_u = 4$. The number of RR is adjusted with respect to the furthest node in each group, to say i, situated at distance r_i corresponding to the radius of the ball containing $in_u - 1$ nodes.

Proposition 2.3 (Multi-user case) *The expressions of m_N and v_N are*

$$m_N = N_s \times \sum_{k=1}^{N_{\max}} k \times \mathbb{E}_r \, \mathbb{E}_{I,P_n} \, \mathbb{E}_{A_f} \left[\mathbb{1}_{\{A_{f,k} \leq A_f < A_{f,k-1}\}} \sum_{i \in \mathbb{N}^*} \text{Prob}\left\{ |\mathcal{B}(r)| = in_u - 1 \right\} \right] \quad (2.16)$$

$$v_N = N_s \times \sum_{k=1}^{N_{\max}} k^2 \times \mathbb{E}_r \, \mathbb{E}_{I,P_n} \, \mathbb{E}_{A_f} \left[\mathbb{1}_{\{A_{f,k} \leq A_f < A_{f,k-1}\}} \sum_{i \in \mathbb{N}^*} \text{Prob}\left\{ |\mathcal{B}(r)| = in_u - 1 \right\} \right] \quad (2.17)$$

where $\mathcal{B}(r)$ is the ball with radius r, and

$$\sum_{i \in \mathbb{N}^*} \text{Prob}\left\{ |\mathcal{B}(r)| = in_u - 1 \right\} = \exp(-\lambda_a \pi r^2) \sum_{i \in \mathbb{N}^*} \frac{(\pi \lambda_a r^2)^{(in_u - 1)}}{(in_u - 1)!}.$$

The distribution of r in the typical cell is given by $f(r)$ defined in (3.1).

Proof: Please refer to Appendix 2.7.5. □

Note that Proposition 2.3 is a generalization of Proposition 2.2 with $n_u = 1$. For $n_u = 1$,

$$\sum_{i \in \mathbb{N}^*} \frac{(\pi \lambda_a r^2)^{(i-1)}}{(i-1)!} = \exp(-\lambda_a \pi r^2)$$

and the expressions of m_N in (2.16) becomes equal to (2.14).

2.3.4 Distribution of the sensor power consumption

We assume that the transmitted power is fixed to P_{RR} per RR and the total power over $N_{\max}$ RRs does not exceed $P_{\max} = N_{\max} P_{\mathrm{RR}}$. The power is then a discrete random variable and its Probability Mass Function (PMF) is given in Proposition 2.4.

Proposition 2.4 (Total sensor power PMF) *For the general case, the sensor power PMF is,*

$$\mathrm{Prob}\{P_t = kP_{\mathrm{RR}}\} = \frac{N_s}{N_g}\, \mathbb{E}_r\, \mathbb{E}_{I,P_n}\, \mathbb{E}_{A_f} \left[\mathbb{1}_{\{A_{f,k} \leq A_f < A_{f,k-1}\}} \sum_{i \in \mathbb{N}^*} \mathrm{Prob}\left\{ |\mathcal{B}(r)| = in_u - 1 \right\} \right],$$

with $1 \leq k \leq N_{\max}$, N_g *the number of the groups of* n_u *sensors in the typical cell such that,*

$$N_g = \int_0^\infty 2\pi\lambda_a r \exp(-\lambda_b \pi r^2) \exp(-\lambda_a \pi r^2) \sum_{i \in \mathbb{N}^*} \frac{(\pi\lambda_a r^2)^{(in_u - 1)}}{(in_u - 1)!} dr$$

and $N_s = \lambda_a / \lambda_b$.

Proof: The proof is similar to Proposition 2.3 and the PMF can be obtained by averaging over the whole power in the typical cell normalized by the size of this latter. In each ring delimited by the $(i-1) \times n_u^{\mathrm{th}}$ and $i \times n_u^{\mathrm{th}}$ neighbor, the n_u sensors adjust their power to the the $i \times n_u^{\mathrm{th}}$ furthest neighbor. □

2.4 Interference and fading characterization

In this section, we compute the average number of RR considering different antenna configuration using Single-User and Multi-User (MU-MIMO) communications.

2.4.1 Single-user: Case of single antenna receiver

In this subsection, we review first the characterization of the Laplace transform of interference and the distribution of the fading in the SISO case averaged on the random noise plus interference.

2.4.1.1 Interference Laplace transform

Considering a SISO antenna configuration, the Laplace transform of the interference is,

$$\mathcal{L}_I(s) = \mathbb{E}\left[e^{-sI}\right] = \mathbb{E}\left[\prod_{x_i \in \Phi_I} e^{-sP_{\mathrm{RR}}\, \alpha |x_i|^{-\beta} A_{f,i}} \right], \tag{2.18}$$

in which Φ_I is the set of the interfering nodes that transmit on the same RR as shown in (2.2). The set of interfering nodes Φ_I cannot be considered as homogeneous PPP and its exact statistical distribution is generally a difficult problem to model. For this, we use the same approximation proposed in [26] that is shown to almost capture the statistical behavior of the interference field. Let d_i be the distance between the interferer and the intended collector. The probability of finding at least one collector in the ball with radius d_i centered at the interferer is $(1 - e^{-\lambda_b \pi d_i^2})$. In this case, a node at distance d_i from the intended collector is considered as interfering with probability of $(1 - e^{-\lambda_b \pi d_i^2})$. It was shown in [26], that the effective interference observed at the tagged collector can be approximatively modeled as a non-homogeneous PPP with intensity $\lambda_b(1 - e^{-\lambda_b \pi d_i^2})$.

Considering exponential power fading attenuation coefficients, the interference Laplace transform from (2.18) for the SISO case is,

$$\mathcal{L}_I(s) = \mathbb{E}\left[\prod_{x_i \in \Phi_I} \frac{1}{1 + sP_{\mathrm{RR}}\ \alpha\ |x_i|^{-\beta}}\right].$$

Using the Probability Generating Functional (PGFL) property, the Laplace transform is then,

$$\mathcal{L}_I^{\mathrm{SISO}}(s) \approx \mathcal{L}_I(s) \triangleq \exp\left(-2\pi\lambda_b \int_0^{\infty} \left[\frac{sP_{\mathrm{RR}}\ \alpha\ u^{-\beta}}{1 + sP_{\mathrm{RR}}\ \alpha\ u^{-\beta}}\right](1 - e^{-\lambda_b \pi u^2})udu\right). \tag{2.19}$$

2.4.1.2 Average fading distribution

Proposition 2.5 (SISO case) *Given a node position $r = |x|$, the SISO fading distribution averaged on the random noise and interference,*

$$\mathbb{E}_{I,P_n}\ \mathbb{E}_{A_f}[\mathbb{1}_{\{A_{f,k} \le A_f < A_{f,k-1}\}}] \quad = \quad \mathcal{L}_{P_n}(s_k)\mathcal{L}_I(s_k) - \mathcal{L}_{P_n}(s_{k-1})\mathcal{L}_I(s_{k-1}), \tag{2.20}$$

with $s_k = \gamma_k P_{\mathrm{RR}}^{-1} \alpha^{-1} r^{\beta}$.

Proof: Please refer to Appendix 2.7.4. □

2.4.2 Single-user case with multi-antenna receiver

We assume a SIMO configuration depicted in Figure 2.4 which n_r antennas are used at the receiver and only a single antenna at each sensor node. Let $F_1, \ldots, F_{n_r}$ denote the fading coefficients between the sensor device and the n_r receive antennas. Assume that the receiver antennas are sufficiently

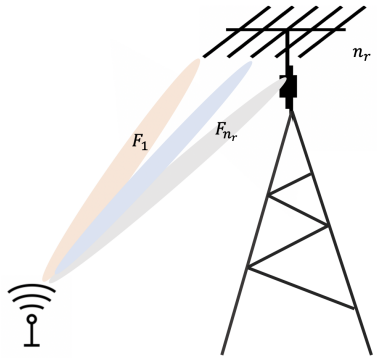

Figure 2.4: Receiver diversity with SIMO configuration

separately to assume that the random exponential fading coefficients are independent. Two transmission modes are considered: the first transmission is the antenna selection in which the transmission is performed on the path with highest fading coefficient. The second transmission is the Maximum Ratio Combiner (MRC), in which the received signals at the different antenna are combined.

2.4.2.1 Antenna selection

Given a node position $r = |x|$, the SIMO fading distribution with antenna selection averaged on the random noise and interference, $A_f = \max(F_1, \ldots, F_{n_r})$ is distributed as the maximum between n_r i.i.d exponential variables. The CDF function is then,

$$\text{Prob}\{A_f \leq u\} = (1 - e^{-u})^{n_r} = \sum_{p=0}^{n_r} (-1)^p \binom{p}{n_r} e^{-pu}. \tag{2.21}$$

Proposition 2.6 (Antenna selection) *The interference Laplace transform with antenna selection is identical to the SISO case in (2.19),*

$$\mathcal{L}_I^{sel}(s) = \mathcal{L}_I(s).$$

Given a node position $r = |x|$, the SIMO fading distribution with MRC averaged on the random noise and interference,

$$\mathbb{E}_{I,P_n}\, \mathbb{E}_{A_f}[\mathbb{1}_{\{A_{f,k} \leq A_f < A_{f,k-1}\}}] = \sum_{p=0}^{n_r} (-1)^p \binom{p}{n_r} \left[\mathcal{L}_{P_n}(ps_{k-1})\mathcal{L}_I(ps_{k-1}) - \mathcal{L}_{P_n}(ps_k)\mathcal{L}_I(ps_k)\right] \tag{2.22}$$

Proof: The interfering signal is received on a random fading coefficient that is exponentially distributed as in the SISO case. The identify in (2.22) can be deduced from the distribution of A_f given in (2.21). □

2.4.2.2 Maximum Ratio Combiner (MRC)

Using a MRC, the equivalent fading coefficient $A_f = F_1 + \ldots + F_{n_r}$ is the sum of n_r random exponential i.i.d. random variables and it is distributed as chi-squared random variable with $2n_r$ degrees of freedom. The CDF of A_f is,

$$\text{Prob}\{A_f \leq u\} = 1 - \sum_{p=0}^{n_r-1} \frac{1}{p!} u^p e^{-u}. \tag{2.23}$$

Proposition 2.7 (MRC decoder) *The interference Laplace transform with MRC is identical to the SISO case in (2.19)*

$$\mathcal{L}_I^{MRC}(s) = \mathcal{L}_I(s).$$

Given a node position $r = |x|$, the SIMO fading distribution with MRC averaged on the random noise and interference,

$$\mathbb{E}_{I,P_n}\, \mathbb{E}_{A_f}[\mathbb{1}_{\{A_{f,k} \leq A_f < A_{f,k-1}\}}] = \sum_{p=0}^{n_r-1} \frac{1}{p!} \Big(\Xi_p(s_k) - \Xi_p(s_{k-1}) \Big) \tag{2.24}$$

with

$$\Xi_p(s) = (-1)^p \sum_{j=0}^{p} s^p \binom{j}{p} \frac{d^j \mathcal{L}_{P_n}(s)}{ds^j} \frac{d^{p-j} \mathcal{L}_I(s)}{ds^{p-j}}, \tag{2.25}$$

where $\frac{d^j f(s)}{ds^j}$ is the derivative of order j of the function $f(s)$ for $j \in \mathbb{N}^*$ and $\frac{d^0 f(s)}{ds^0} = f(s)$.

Proof: The proof of this proposition is detailed in Appendix 2.7.5. □

2.4.3 Multi-user with multi-antenna receiver

In order to cancel the multi-user interference, a Zero-Forcing decoder is used by projecting the $n_r \times 1$ received signal on the kernel of the space formed by the $n_r \times 1$ fading vectors of the $(n_u - 1)$ other scheduled users. As stated by [112], the orthogonality constraints consume $(n_r - n_u + 1)$ degrees of freedom. The receiver diversity for each sensor device is limited then to $(n_r - n_u + 1)$.

To extract this diversity, we assume that the ZF decoder is followed by a MRC that combines the $(n_r - n_u + 1)$ received observation. The fading coefficient $A_f^{(j)}$ observed by each sensor in Figure 2.2 is then chi-squared distributed with $2(n_r - n_u + 1)$ degrees of freedom.

Proposition 2.8 (MU case with ZF-MRC decoder) *For the MU-MIMO case with ZF decoder followed by a MRC, the equivalent fading distribution averaged on the random noise and interference,*

$$\mathbb{E}_{I,P_n}\,\mathbb{E}_{A_f}[\mathbb{1}_{\{A_{f,k}\leq A_f<A_{f,k-1}\}}] = \sum_{p=0}^{n_r-n_u}\frac{1}{p!}\Big(\Xi_p(s_k)-\Xi_p(s_{k-1})\Big). \tag{2.26}$$

The interference Laplace transform is approximated by,

$$\mathcal{L}_I^{MU}(s) \approx \mathcal{L}_I(n_u s).$$

Proof: For the multi-user case, n_u users in each cell transmit in the same RR. The interference becomes higher than the SISO case. As all neighboring users are multiplexed on the same RR, we approximate the sum of interference coming from the group of n_u users by an interfering signal generated by a random interferer transmitting with $n_u P_{\mathrm{RR}}$. We have validated this approximation using numerical results as it will be shown in the next section.
The rest of the proof is similar to Proposition 2.7 considering $2(n_r - n_u + 1)$ degrees of freedom. □

2.5 Numerical Results

In this section, we consider the uplink of a sensor network corresponding to the licensed IoT with parameters summarized in Table 2.1. We assume that the density of nodes $\rho = 500$ sensors per km^2 transmitting in average once each half-an-hour, $n_a = 48$ during 20 seconds. The active node density is then $\lambda_a = 5.5$ sensors per km^2. We consider a cellular network with ranges between 500 m to 1.5 km corresponding to a collector density of $\lambda_b = 0.9$ nodes per km^2 down to 0.1 nodes per km^2 (the ranges are obtained with a confidence margin of 95%). The maximal power is limited to 14 dBm and is uniformly distributed among the allocated RRs. Table 2.2 gives the matching between the SINR range with the required number of RRs to achieve a target rate of $C_0 = 500$ bps. This data are derived from the Link Layer Simulation (LLS) provided in [113] on the Physical Uplink Shared Channel (PUSCH) of LTE-Cat M. To evaluate network performances, we consider a path-loss in an urban/sub-urban

Parameters	**Value**
Intensity of active nodes	$\lambda_a = 5.5$ nodes per km^2
Intensity of collectors	$\lambda_b = 0.1$ to 0.9 nodes per km^2
Transmission power	$P_{\mathrm{RR}} = 6.3$ dBm
RR per node	1 to 6 RRs
Configuration	SISO, single-user 1×8 SIMO,
	1×8 MU-MIMO with $n_u = 2$ or 4
Okumura-Hata model	$\alpha = 10^{-14.1}$, $\beta = 3.5$
Target data rate	≥ 500 bps

Table 2.1: Network Parameters

environment with $\alpha = 10^{-14.1}$ and $\beta = 3.5$. We consider the following antenna configurations: SISO, single SIMO with $n_r = 8$, multi-user SIMO with $n_r = 8$ and $n_u = 2$ or $n_u = 4$.

RR per node	SINR range (dB)
1	[-20.6; $+\infty$[
2	[-22.6; -20.6[
3	[-23.6; -22.6[
4	[-23.7; -23.6[
5	[-23.9; -23.7[
6	[-25.1; -23.9[

Table 2.2: MCS table: SINR versus RR required to achieve R = 500 bps

2.5.1 Accuracy of the theoretical model

Table 2.3 indicates the percentage difference between the mean number of RRs required in the typical cell derived by using our statistical dimensioning tools and the empirical network simulation results. The mean number of required RRs using former method is denoted as m_N, the simulation one is denoted as $m_{N,s}$. Consequently, the percentage difference is $\Delta m_N/m_{N,s} = |m_N - m_{N,s}|/m_{N,s}$. We consider different collector intensities (from 0.1 to 0.9 nodes/km^2) and different antenna configurations as well as transmission modes. As presented in the Table 2.3, the comparison shows that the difference between the results obtained by our statistical tools and the simulated values is very small, which

verifies the accuracy of our model and approach.

λ_b	SISO	1×8 SIMO selection	1×8 SIMO MRC	1×8 MU-MIMO $n_u = 2$	1×8 MU-MIMO $n_u = 4$
0.1	0.0012	0.0120	0.0417	0.0157	0.0392
0.3	0.0395	0.0435	0.0239	0.0144	0.0050
0.5	0.0201	0.0041	0.0398	0.0208	0.0916
0.7	0.0006	0.0080	0.0070	0.0206	0.2001
0.9	0.0206	0.0593	0.0292	0.0757	0.2811

Table 2.3: The percentage change $\Delta m_N/m_{N,s}$ of the theoretical values m_N and the empirical values $m_{N,s}$.

2.5.2 Average and total number of RR

Figure 2.5 further illustrates the specific value of m_N considering different network configurations. As shown in the figure, for the given active sensor and collector intensities λ_a and λ_b, respectively, assuming a maximum delay of 1 ms, the SISO system always requires the highest mean number of RRs. With the use of SIMO and MU-MIMO, multi-antenna techniques achieve higher data rates through increased spectral efficiency, with a corresponding reduction in the required RRs. The multiple receive antennas system has the potential to enhance signal robustness and increase system capacity. In particular, the MU-MIMO system significantly reduces the mean number of RRs required in a typical cluster. Meanwhile, as collector intensity λ_b increases, the mean number of RRs required for various configurations decreases. When λ_b increases, the radius of the typical cell will decrease, while the number of active sensor nodes per unit area remains the same, which means that each collector needs to serve fewer nodes in the cell and thus the number of RRs required decreases.

Figure 2.6 presents the total number of required RRs in a typical cell versus the collector intensity. It maintains the same trend as in Figure 2.5, with MU-MIMO being the best performing case, followed by SIMO and then SISO.

2.5.3 Empirical distribution and actual average delay

Figure 2.7 illustrates the empirical Cumulative Distribution Function (CDF) of the total number N_t of RRs required for the typical cell with $\lambda_a = 5.5$ nodes/km^2 and $\lambda_b = 0.5$ nodes/km^2. For example, according to Figure 2.6, for the same value of λ_a, λ_b, we find that the N_t value required for

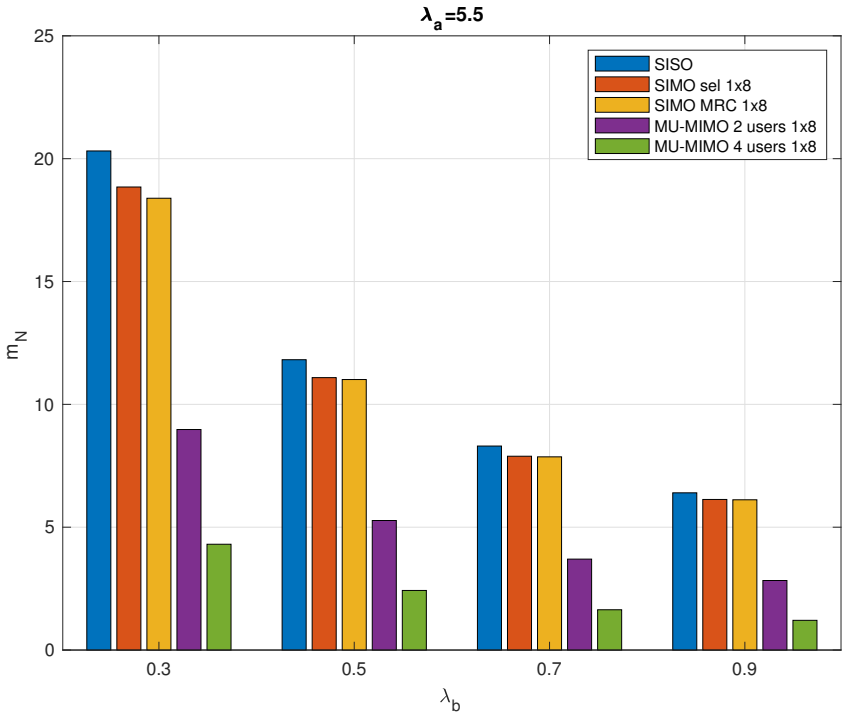

Figure 2.5: Mean number of required RRs in a typical cell considering λ_b ranges from 0.3 to 0.9 nodes/km^2 with $\lambda_a = 5.5$ nodes/km^2, $\tau_{max} = 1$ ms.

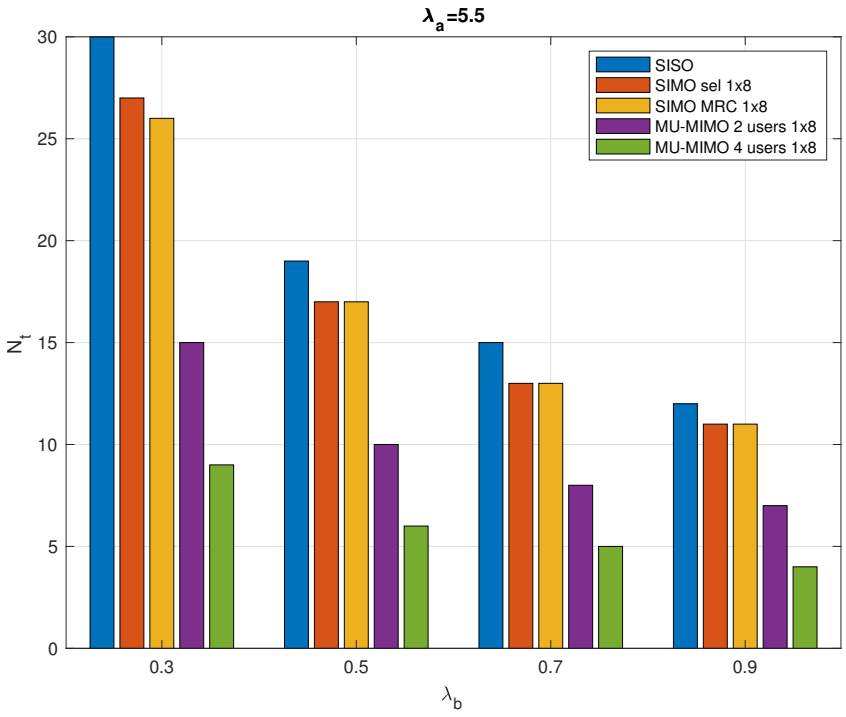

Figure 2.6: Total number of required RRs in a typical cell versus the collector intensity λ_b with $\lambda_a = 5.5$ nodes/km^2, $\tau_{max} = 1$ ms.

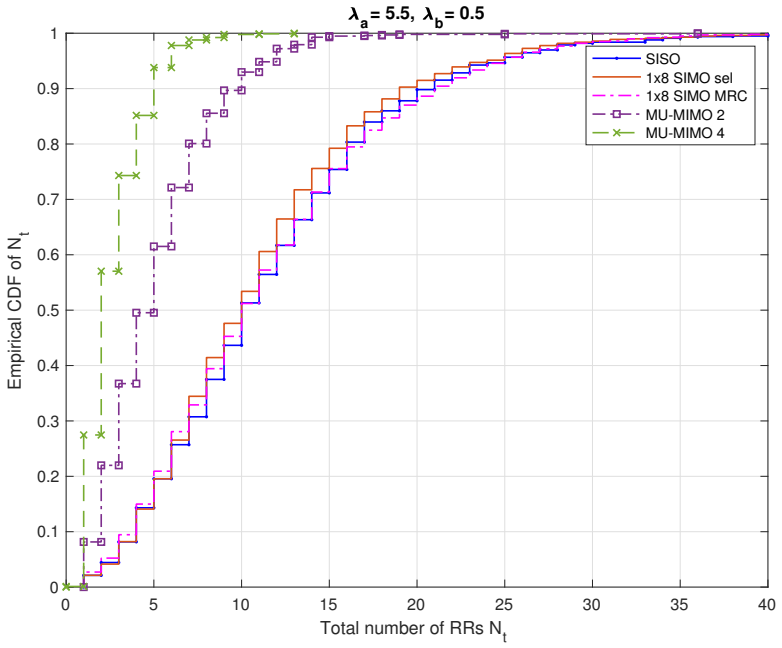

Figure 2.7: The empirical Cumulative Distribution Function (CDF) of N_t total number of RRs required for the typical cell in which the maximal delay $\tau_{max} = 1$ ms, $\lambda_a = 5.5$ nodes/km^2 and $\lambda_b = 0.5$ nodes/km^2.

the SISO system is 19. In Figure 2.7, we can see that $N_t = 19$ corresponds to a CDF value of 0.88. This means that there is a network outage probability of $1 - 0.88 = 0.12$ meaning that the network cannot attributed RR to 12% of nodes in the typical cell. The corresponding average delay can be then computed using (2.12).

Figure 2.8 show the actual average access delay corresponding to different antenna configurations and transmission modes for given intensities of active sensors and collectors λ_a, λ_b, and the maximum access delay $\tau_{max} = 1$ ms. It can be seen from the figure that the average access delay τ is less than the maximum access delay τ_{max}. SIMO with MRC transmission mode requires the longest access time because it has the lowest individual off probability i.e., it serves the largest percentage of active nodes. The second highest access delay is the SIMO with antenna selection scheme. For the SISO configuration, the average access delay is relatively lower because in this mode, many nodes are in off state and not served. For the MU-MIMO system, each time there are n_u nodes transmitting information simultaneously and being processed by the collector. The larger the n_u is, the shorter the average access delay required.

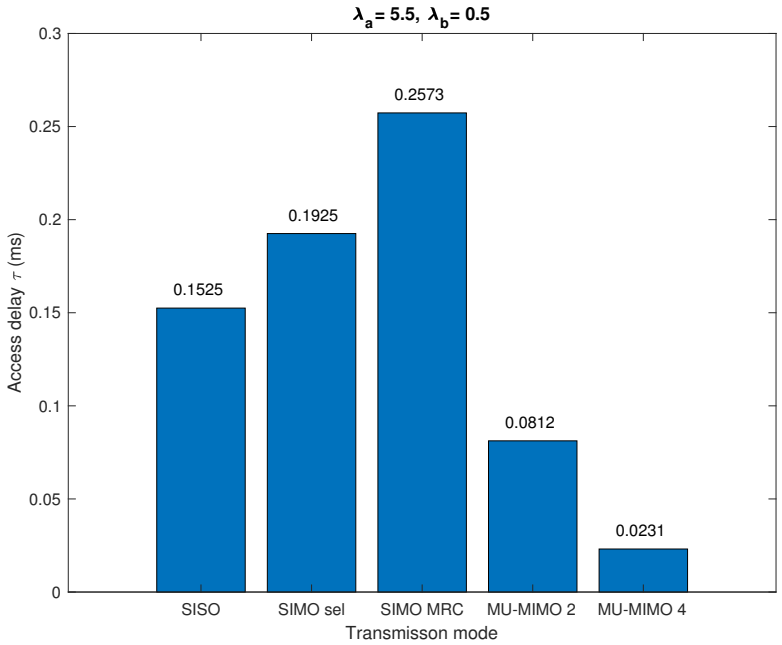

Figure 2.8: Low access delay τ with statistical dimensioning in which the maximal delay $\tau_{max} = 1$ ms, $\lambda_a = 5.5$ nodes/km^2 and $\lambda_b = 0.5$ nodes/km^2.

2.5.4 Tolerated delay and over-dimensioning

Figure 2.9 gives a comparison of the theoretical and empirical values of N_t for a typical cell that guarantee an average delay of 1 ms. From the figure, it can be seen that the N_t derived by our statistical tool is always larger than the empirical N_t, i.e., it is over-dimensioning. The excess in the radio-ressource provided by the theoretical model ensures that the expected data rate is achieved and the access to the cellular IoT network does not exceed the predefined average access delay.

In Figure 2.10, it shows the relationship between the total number of required RRs and the maximal access delay τ_{max} with $\lambda_a = 5.5$ nodes/km^2 and $\lambda_b = 0.5$ nodes/km^2. Assuming that τ_{max} ranges from 0.5 to 4 ms, a larger τ_{max} means that the node can wait longer for access to the network. The average access delay τ of the active nodes must not exceed the maximal delay $\tau \leq \tau_{max}$. In general, a lower total number of RRs is required to response to the demands of active sensor nodes with a larger τ_{max}.

2.5.5 Individual sensor off probability

As mentioned in Subsection 2.3.1, when the SINR received on the collector side is below the SINR threshold $\gamma_{N_{max}}$, no RR will be assigned to this sensor. In other words, this active sensor is forced to

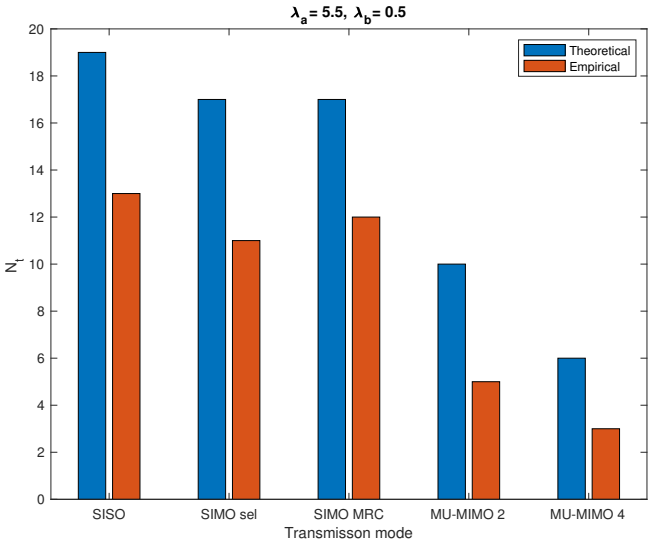

Figure 2.9: Comparison between theoretical and empirical N_t values in which $\lambda_a = 5.5$ nodes/km^2 and $\lambda_b = 0.5$ nodes/km^2.

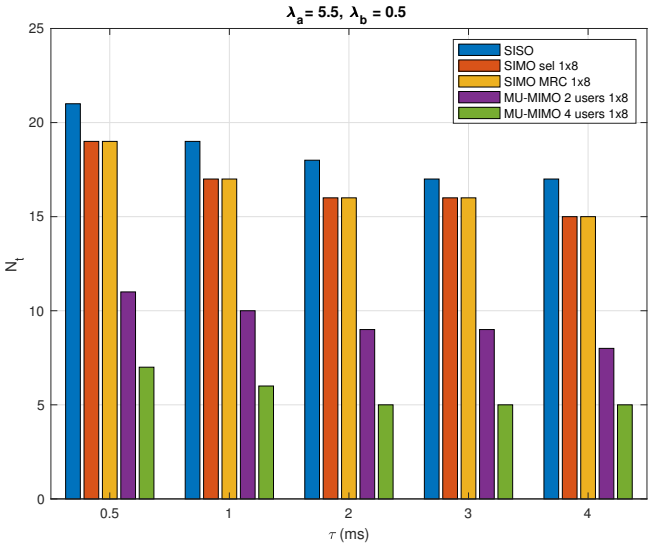

Figure 2.10: Total number of required RRs in a typical cell with respect to maximal access delay τ_{max} with $\lambda_a = 5.5$ nodes/km^2 and $\lambda_b = 0.5$ nodes/km^2.

be off in this trial. Table 2.4 illustrates the individual off probability in the typical cell according to the different antenna configurations, including SISO, 1×8 SIMO with antenna selection and MRC, 2 users and 4 users 1×8 MU-MIMO. From the table, we can see, the 1×8 SIMO with MRC outperforms other modes in the individual off probability. Although it doesn't reduce the number of RRs required in the typical cell significantly compared to the SIMO with antenna selection or the MU-MIMO, it does reduce the sensor individual off probability, ensuring more sensors to be served. This result gives us a new way of thinking about resource planning, i.e. we need to take into account both the total number of RRs assigned to the network and the individual off probability to improve network service.

λ_b	SISO	1×8 SIMO selection	1×8 SIMO MRC	1×8 MU-MIMO $n_u = 2$	1×8 MU-MIMO $n_u = 4$
0.1	23.40%	5.62%	**1.01%**	1.40%	2.90%
0.3	7.13%	0.31%	**0.03%**	0.07%	0.27%
0.5	3.97%	0.09%	**0.02%**	0.05%	0.20%
0.7	2.84%	0.07%	**0.01%**	0.05%	0.20%
0.9	2.30%	0.06%	**0.01%**	0.04%	0.21%

Table 2.4: Statistical individual OFF probability with regard to antenna configuration, transmission mode and collector intensity λ_b.

2.5.6 Power distribution

In Table 2.5, for a given pair of λ_a and λ_b, we elaborate the power distribution with the different transmission modes in the typical cell. The transmission power of each RR is fixed to $P_{\mathrm{RR}} = 25/6$ mW (6.3 dBm), so the maximal transmission power is $N_{\max} P_{\mathrm{RR}} = 25$ mW (14 dBm) with $N_{\max} = 6$. For each transmission mode, Table 2.5 shows the specific percentage share of each transmit power. Where off represents a number of nodes to which no RR is assigned and therefore have a transmission power of 0 mW. From P_{RR} to $6P_{\mathrm{RR}}$ corresponds to the transmission power of the nodes that are assigned the corresponding number of 1 to 6 RRs, respectively. As marked in the light grey part of the table, it can be noticed that SIMO with MRC mode has the least number of off nodes, meanwhile with 99.92% of the nodes being transmitting information at P_{RR} power. Therefore it has the best power distribution. MU-MIMO with $n_u = 2$ also has a good power distribution, with only 0.05% of nodes off and 99.80% of nodes transmitting at P_{RR}. SISO has the worst performance, with up to 3.97% of nodes unable to transmit information and only 90.76% of nodes transmitting at low power.

Power (mW)	SISO	1×8 SIMO selection	1×8 SIMO MRC	1×8 MU-MIMO $n_u = 2$	1×8 MU-MIMO $n_u = 4$
Off	3.97%	0.09%	**0.02%**	0.05%	0.20%
P_{RR}	90.76%	99.39%	**99.92%**	99.80%	99.17%
$2P_{\mathrm{RR}}$	2.81%	0.35%	0.04%	0.10%	0.40%
$3P_{\mathrm{RR}}$	1.11%	0.09%	0.01%	0.03%	0.12%
$4P_{\mathrm{RR}}$	0.10%	0.01%	0.00%	0.00%	0.01%
$5P_{\mathrm{RR}}$	0.20%	0.01%	0.00%	0.00%	0.02%
$6P_{\mathrm{RR}}$	1.06%	0.06%	0.01%	0.02%	0.09%

Table 2.5: The power distribution with the different transmission modes in the typical cell, $P_{RR} = 25/6$ mW, $\lambda_a = 5.5$ nodes/km^2, $\lambda_b = 0.5$ nodes/km^2.

2.6 Conclusion

In this chapter, we focus on licensed OFDMA-based IoT networks which corresponds to NB-IoT, LTE-M and to some extent 5G network using the numerology 0. We assume that a wireless sensor network in which sensor nodes and collectors are distributed according a spatial PPP. A statistical method based on PPP is proposed to model and analyze the average behavior of the cellular IoT networks. This method is used for statistical resource planning to support the dominant uplink communications in the IoT networks and fulfill the network requirements in terms of limited transmission power per RR, low access delay, preset network outage probability and target data rate. Different antenna configurations and transmission modes are taken into account, e.g., SISO, SIMO and MU-MIMO. Based on the preset tolerated average access delay and target data rate, the specific total number of RRs required for the typical cell is further calculated. Numerical results are finally given to assess our statistical analysis. We compare the theoretical results with the empirical simulation results in detail. The comparison shows that the results obtained from our statistical model are very close to the empirical results. Moreover, the results highlights and quantifies the radio resources gain obtained by the receiver diversity techniques and the multi-user gains.

With the growing demand on wireless connectivity for IoT, the limited and expensive band resource in IoT technologies cannot fully meet all the market requirements. These technologies should be complemented by technologies operating in licensed exempt-band offering massive access for non real time and non critical application. In the next chapters, we will focus on the mitigation of interference

in the unlicensed LoRa networks.

2.7 Appendices

2.7.1 Proof of Proposition 2.1

Consider the set of all active nodes $x \in \Phi_a$ generated by the homogeneous PPP, the node x is in the typical cluster $\Phi_c(0)$ if the origin is o is the closest point to x among all the other collectors $y \in \Phi_b$, *i.e.* $|x| < |y-x|, \quad \forall y \in \Phi_b$. We can note that the following indicator function

$$\prod_{y\in\Phi_b} \mathbb{1}_{\{|x|<|y-x|)} = \begin{cases} 1 & x \in \Phi_c(0), \\ 0 & \text{otherwise.} \end{cases}$$

The average number of users in this typical cell is,

$$\mathbb{E}\Big[\mathbb{1}_{\{x\in\Phi_c(0)\}}\Big] = \sum_{x\in\Phi_a}\left[\prod_{y\in\Phi_b} \mathbb{1}_{\{|x|<|y-x|)}\right]$$

Using Campbell Theorem,

$$\sum_{x\in\Phi_a}\left[\prod_{y\in\Phi_b} \mathbb{1}_{\{|x|<|y-x|)}\right] = \int\left[\prod_{y\in\Phi_b} \mathbb{1}_{\{|x|<|y-x|)}\right]\lambda_a dx. \tag{2.27}$$

For a given $x \in \Phi_a$, we use the PGFL property on the PPP of Φ_b,

$$\begin{aligned}\mathbb{E}\Big[\prod_{y\in\Phi_b} \mathbb{1}_{\{r<|y-x|\}}\Big] &= \exp\Big(-\lambda_b\int_{\mathbb{R}^2}(1-\mathbb{1}_{\{r<|y-x|\}})dy\Big) \\ &= \exp\Big(-\lambda_b\int_{|y-x|^2<r^2} dy\Big). \end{aligned}\tag{2.28}$$

Note that $|y-x|^2 = |y|^2 + |x|^2 - 2|y||x|\cos(\theta_z - \theta_y)$ where $|y|$ and θ_y (resp. $r = |y|$ and θ_x) are the polar coordinates of z (resp. y). The condition $|y-x|^2 < r^2$ in (2.28) is then equivalent to $|y| < 2|x|\cos(\theta_y - \theta_x)$ with $0 \le (\theta_y - \theta_x) \le \pi$ to guarantee a positive range of r_y. The corresponding integral is then,

$$\int_{|y-x|^2<r^2} dy = \int_0^{\pi-\theta_x}\int_0^{2r\cos(\theta_y-\theta_x)} r_y dr_y d\theta_y = \int_0^{\pi-\theta_x} r^2\cos^2(\theta_y-\theta_x)d\theta_y = \pi r^2 \tag{2.29}$$

independently of x. Replacing in (2.27), the equation (2.28) and (2.29), we have,

$$\mathbb{E}\Big[\mathbb{1}_{\{x\in\Phi_c(0)\}}\Big] = \int_0^\infty\int_0^{2\pi}\exp(-\lambda_b\pi r^2)\lambda_a r dr d\theta = \frac{\lambda_a}{\lambda_b}.$$

Finally, the pdf of r can be deduced using the CDF of r,

$$\text{Prob}\{x \in \Phi_c(0)\} = \text{Prob}\{\prod_{y\in\Phi_b}\mathbb{1}_{\{r<|y-x|\}}\} = \exp(-\lambda_b\pi r^2)$$

2.7.2 Proof of Proposition 2.2

The average number of radio-resources in the typical cluster is,

$$m_N = \mathbb{E}\Big[\sum_{x\in\Phi_c(o)} N_{RR}(x, A_f, I, P_n)\Big] = \mathbb{E}_{\Phi,\Phi_b,A_f,I,P_n}\Big[\sum_{x\in\Phi_a} \underbrace{\prod_{y\in\Phi_b} N_{RR}(x, A_f, I, P_n)\ \mathbb{1}_{\{|x|<|y-x|)\}}}_{f(x)}\Big]$$

Using Campbell Theorem,

$$m_N = \mathbb{E}_{A_f,I,P_n}\Big[\lambda_a \int \mathbb{E}_{\Phi_b}[f(x)]dx\Big].$$

with $dx = rdrd\theta$ and

$$\mathbb{E}_{\Phi_b}[f(x)] = N_{RR}(x, A_f, I, P_n)\ \mathbb{E}_{\Phi_b}\Big[\prod_{y\in\Phi_b} \mathbb{1}_{\{|x|<|y-x|)\}}\Big]. \tag{2.30}$$

Using the relationships (2.28) and (2.29),

$$m_N = \frac{\lambda_a}{\lambda_b}\ \mathbb{E}_{I,P_n}\mathbb{E}_{A_f}\left[\int N_{RR}(r, A_f, I, P_n)\ 2\pi\lambda_b r \exp(-\lambda_b\pi r^2)dr\right].$$

Notice that $2\pi\lambda_b r\exp(-\lambda_b\pi r^2)$ is nothing but the pdf of the smallest distance between the sensor and its nearest collector. This implies that,

$$m_N = \frac{\lambda_a}{\lambda_b}\ \mathbb{E}_r\ \mathbb{E}_{I,P_n}\ \mathbb{E}_{A_f}[N_{RR}(r, A_f, I)].$$

Proposition 2.2 can be deduced by replacing $N_{\mathrm{RR}}(r)$ by (2.9).

2.7.3 Proof of Proposition 2.3

Considering the distance based scheduling algorithm, we adjust the dimensioning of each group with respect to the $i \times n_u^{\mathrm{th}}$ nearest neighbor to the typical collector ($i \in \mathbb{N}^*$). We let r_i denote the distance between this $i \times n_u^{\mathrm{th}}$ nearest neighbor $x_i = r_i e^{j\theta_i}$ and the typical collector. The average number of required RR in the typical cluster is the total number of RR required by this $i \times n_u^{\mathrm{th}}$ nearest neighbors, such that,

$$m_N = \mathbb{E}_{r_i,\theta_i,A_f,I,P_n}\left[\sum_{r_i:i\in\mathbb{N}^*} N_{RR}(r_i, A_f, I, P_n) \prod_{y\in\Phi_b} \mathbb{1}_{\{r_i<|y-x_i|\}},\right]$$

By average on the collectors distribution as in Proof 2.7.2,

$$\mathbb{E}_{\Phi_b}\left[\prod_{y\in\Phi_b} \mathbb{1}_{\{r<|y-x_i|\}}\right] = \exp(-\lambda_b\pi r_i^2).$$

The average number of required RR is then,

$$m_N = \mathbb{E}_{A_f,I,P_n}\Big[\sum_{i\in\mathbb{N}^*}\int N_{RR}(r_i)\exp(-\lambda_b\pi r_i^2)f_{R_i}(r_i)dr_i\Big]$$

with

$$f_{R_i}(r_i) = \frac{2(\pi\lambda_a)^{in_u}}{(in_u-1)!}r_i^{2in_u-1}\exp(-\lambda_a\pi r_i^2)$$

being the distribution of $i\times n_u^{\text{th}}$ nearest neighbor of the typical collector.

2.7.4 Proof of Proposition 2.5

Using a single antenna receiver, the SISO fading coefficients are Rayleigh distributed and A_f has an exponential distribution, and,

$$\mathbb{E}_{A_f}[\mathbb{1}_{\{A_{f,k}\leq A_f<A_{f,k-1}\}}] = e^{-(P_n+I)s_k} - e^{-(P_n+I)s_{k-1}}.$$

Proposition 2.5 is obtained considering the average behavior of the noise and interference.

2.7.5 Proof of Proposition 2.7

2.7.5.1 Laplace transform of the interference with MRC

To show that the Laplace transform remains the same, we let $\mathbf{h}_x = [h_{x,1}\dots h_{x,n_r}]$ denote the complex Gaussian vector containing the (signal) fading coefficients and $\mathbf{h}_y = [h_{y,1}\dots h_{y,n_r}]$ the fading vector between the interferer and the collector. Unlike in [114], the receiver in our case is not aware of the interference power in each branch and does not take into account the non uniform instantaneous interference power over the branches [114]. The n_r observations of x are projected into the orthonormal vector $\mathbf{u}_x = \mathbf{h}_x/\|\mathbf{h}_x\|$. The equivalent interferer channel is then the scalar product between $\mathbf{u}_x$ and $\mathbf{h}_y$. Let $\mathbf{u}_y = \mathbf{h}_y/\|\mathbf{h}_y\|$, the equivalent fading seen by each interferer $A_{f,i} = |\langle\mathbf{u}_x,\mathbf{h}_y\rangle|^2$ is exponentially distributed. This is a consequence that the cosinus square of an angle between a Gaussian vector and a given direction $\cos^2(\mathbf{u}_x,\mathbf{h}_y)$ is beta distributed with parameters 1 and (n_r-1) as shown in [99]. This leads to a distribution of $\beta(1,n_r-1)$ by a chi-squared with $2n_r$ degrees of freedom which is exponentially distributed. In other words,

$$A_{f,i} = |\langle\mathbf{u}_x,\mathbf{h}_y\rangle|^2 = \|\mathbf{h}_y\|^2\cos(\mathbf{u}_x,\mathbf{u}_y) \sim \chi^2_{2n_r}\times\beta(1,n_r-1) = \text{exprnd}(1).$$

2.7.5.2 Fading distribution

Using the distribution of A_f in (2.23),

$$\mathbb{E}_{A_f}[\mathbb{1}_{\{A_{f,k}\leq A_f<A_{f,k-1}\}}] = \sum_{p=0}^{n_r-1} \frac{1}{p!}\Big[(P_n+I)^p s_k^p e^{-(P_n+I)s_k} - (P_n+I)^p s_{k-1}^p e^{-(P_n+I)s_{k-1}}\Big],$$

By averaging over the noise and the interference level, Proposition 2.7 is obtained by invoking the following lemma:

Lemma 2.1 *Let* $\Xi_i(s) = \mathbb{E}\left[s^i (P_n+I)^i e^{-s(P_n+I)}\right]$ *Then,*

$$\Xi_i(s) = (-1)^i \sum_{j=0}^{i} s^i \binom{i}{j} \frac{d^j \mathcal{L}_{P_n}(s)}{d\, s^j} \frac{d^{i-j}\mathcal{L}_I(s)}{d\, s^{i-j}}.$$

Proof: The expansion of $\Xi_i(s) = \mathbb{E}\left[s^i (P_n+I)^i e^{-s(P_n+I)}\right]$ gives

$$\Xi_i(s) = \frac{1}{i!} \sum_{j=0}^{i} s^i \binom{i}{j} \mathbb{E}\left[\, P_n^j I^{i-j} e^{-s(P_n+I)}\right]. \tag{2.31}$$

Due to the independence of P_n and I,

$$\Xi_i(s) = \frac{1}{i!} \sum_{j=0}^{i} s^i \binom{i}{j} \mathbb{E}\left[P_n^j e^{-sN}\right] \mathbb{E}\left[I^{i-j} e^{-sI}\right]. \tag{2.32}$$

Note that, for a given random variable X, we have,

$$\begin{aligned} \frac{d^k}{d^k s}\Big(\mathcal{L}_X(s)\Big) &= \frac{d^k}{d^k s}\left[\int_{\mathbb{R}} e^{-sx} p_X(x) dx\right] \\ &= (-1)^k\, \mathbb{E}[X^k e^{-sX}]. \end{aligned}$$

□

Chapter 3

Adaptive Multi Channels Allocation in LoRa Networks

In this chapter, we consider an IoT dedicated network corresponding to a non licensed LoRa Low Power Wide Area Network. The LoRa network operates in the unlicensed 868 MHz band within a total bandwidth of 1 MHz divided into 8 orthogonal channels of 125 kHz each. Despite the high level of interference, this network offers long range communications in the order of 2 to 5 km in urban areas and 10 to 30 km in rural areas. To efficiently mitigate this high level of interference, LoRa network essentially relies on a Chirp Spread Spectrum (CSS) modulation and on repetition diversity mechanisms. The LoRa CSS modulation spreads the signal within a band of 125 kHz using 6 possible spreading factors (from 7 to 12) to target data rates (starting from 5 kbps for the closest node to 300 bps for the furthest ones). The repetition diversity mechanisms enable the data recovery when the transmission is subject to bad channel conditions or/and high interference levels. Although the CSS modulation protects edge-cell's devices from the high level of interference induced by nodes in the proximity of the collector, it fails to protect nodes at the edge of a given SF region and several trials are required to recover the packet. In this chapter, we propose an adaptive multi-sub bands allocation policy that attributes multiple adjacent channels of 125 kHz for nodes situated at the edge of SF zones. We study the impact of this adaptive sub-band allocation on the collectors' intensities, the rate distribution and the power consumption. Our results are based on a statistical characterization of the interference in the network as well as the outage probability in a typical cell.

3.1 Introduction

With the massive expansion of the Internet of Things (IoT) application, several dedicated Low Power and Wide Area (LPWA) communications technologies have emerged. A statistical study from Ericsson [115] predicts 34 billion connected devices in 2024 among which 4.5 billion of IoT long range connected devices. To fulfill these massive demand on wireless connectivity, dedicated unlicensed LPWAN, considered as complementary to the licensed ones, have been extensively developed in the last recent years.

In this chapter, we focus on the LoRa technology that operates in the unlicensed 868 MHz band [116], [117]. within a total bandwidth of 1 MHz. The frequency band is usually sub-divided into several channels, typically 8 channels of 125 kHz, 4 channels of 250 kHz or 2 channels of 500 kHz. To maximize the success rate of packet transmission, LoRaWAN supports packet repetition and adopts Chirp Spread Spectrum (CSS) modulation that is parametrized by a Spreading Factor (SF). This latter is chosen to adapt the data rate with respect to the radio propagation condition. Depending on the value of SF, a symbol of SF bits is represented by a chirp that occupies a fixed bandwidth, and a chirp duration that increases with SF. The SF value increases with distance and the coverage cell is divided into several SF regions.

Several experimental and analytic works have addressed the performance of LoRa network in terms of coverage, power consumption and the multi-user network capacity [118, 119, 120, 121, 122, 123, 124]. It has been shown that using the highest SF, the LoRa's communication range can reach more than 20 km in line-of-sight environments such as the maritime environment [118, 119]. However, these coverage performances are significantly affected by obstacles and the coverage ranges reduce to few kms in urban and rural environments [118, 119, 120]. Other experimental setups in [118, 119] show that the device battery life can be increased by tuning the SF, the coding rate and the bandwidth size. Finally, experimental studies were led to evaluate the multi-user capacity of the LoRa gateway [121, 122]. In [122], the authors show that under a packet rate reception of 70%, the gateway supports within 15 mins up to 6000 nodes. The multi-user capacity of the gateway has been also analytically studied in many previous works, including [123, 124] to name but a few. These works generally assess the efficiency of the LoRa communications based on the simplification of strictly orthogonal sequences if they originated from different spreading factors. Indeed, as pointed in [123] signals having

different spreading factors can be received simultaneously but, given the co-channel rejection of SF combinations, at the condition that none is received with a much higher power than another. Using the ideal SF orthogonality assumption, the co-spreading factor interference however rapidly limits the scalability of LoRa networks, according to [124]. In this work, the authors found out that in each 125 kHz sub-band, the co-SF interference is the main cause of outage as soon as the number of end devices increases.

In this chapter, we propose a statistical modeling of the interference level received in LoRa network considering the intra-SF and cross-SF interference and deduce the outage behavior. To mitigate this high level of interference, LoRa network expoits repetition mechanisms where several trials are performed to recover the packet. This leads to an increased energy consumption and decreases the device battery life. Our goal in this chapter is to decrease the number of the trials in the network and hence to improve the energy efficiency. For this, we propose to relax the spectral efficiency by adaptively allocating higher bandwidth depending on the position of the nodes in the cell. To statistically evaluate the network performance, we consider the average statistical behavior where the active sensors and collectors are randomly distributed in a given area according to a random Poisson Point Process (PPP). The randomness of the wireless channel is represented by a mark introduced in the PPP as in [26, 27, 28, 29, 30, 31, 32, 33]. In a typical LoRa cell, we provide an analytic characterization of the interference and the outage probability distribution in function of the communication range. We derive this probability for both cases of fixed and adaptive sub-band allocation. The expression of the outage depends on the inter-correlation factors between the different spreading factor regions and the multi-band sizes that we also compute in this chapter. Based on this outage probability expression, we evaluate the enhancement in terms of error, rate distribution and power consumption when using multi channels allocation policy.

The rest of the chapter is organized as follows. Section 3.2 defines the IoT network, the LoRa CSS modulation and the fixed and adaptive multi sub-band allocation. Then, we statistically characterize in Section 3.3 the interference in a LoRa network taking into account the inter-correlation factors between the different spreading factor regions and the multi-band sizes. The outage probability within one and multi-trial is deduced in Section 3.4. Section 3.5 explains SF and channels allocation policy. Section 3.6 provides numerical results that assess the analytic ones and compare the numerical performance for the adaptive multi sub-band allocation to the fixed sub-allocation in terms of outage probability,

coverage, rate distribution and power consumption. Finally, Section 3.7 concludes the chapter.

3.2 IoT LoRa Network Model

In this section, we describe the system parameters, the Chirp Spectrum Spreading (CSS) modulation as well as the access to the shared medium techniques in LoRa networks.

3.2.1 Network parameters

We consider the uplink of a LoRa network in which a set of active devices Φ_a are distributed in a region $\mathcal{A}$ according to an homogeneous PPP characterized by its intensity λ_a nodes per km^2. We assume that there is no coordination between transmitting devices. The collectors are distributed according to a spatial PPP distribution with intensity λ_b collectors per km^2 and we let Φ_b denote the collectors set. Due to Slivnyak-Mecke Theorem in [27], the statistical behavior in the PPP remains unchanged when adding a collector at the center of this region. We assume that each sensor node is connected to the nearest collector. We focus on the typical cell centered at the origin o containing the set of all sensor nodes connected to o. Let $r = |x|$ be the distance between any sensor node x belonging to this typical cell and the origin. The probability distribution function of the distance r is known from [27, 28] and is,

$$f(r) = 2\pi\lambda_b r e^{-\lambda_b \pi r^2}. \tag{3.1}$$

Due the random spatial distribution of the collectors in the network, the cell coverage radius is a random variable. The maximal coverage radius R_c of the cell is determined with a confidence level of p_c is,

$$R_c = \sqrt{\frac{1}{\pi\lambda_b} \ln\left(\frac{1}{1-p_c}\right)}. \tag{3.2}$$

We set $p_c = 99\%$, and we determine λ_b ranges using (3.2) considering rural and urban environments in Table 3.1. The sensor nodes transmit with a maximal power of 14 dBm. The sensor nodes and the collector have omnidirectional antennas with 0 dBi of gain. For a given transmitting node x situated at a distance $|x|$ from the typical collector, the received power at the collector is,

$$P_r(x) = \alpha |x|^{-\beta} P_t \, A_f, \tag{3.3}$$

where α and β are respectively the attenuation factor and the path-loss exponent that are computed from the Okumura-Hata model, A_f is the random fading coefficient that is exponentially distributed

and P_t the transmission power. In LoRa network, the access to the shared medium is managed by an Aloha protocol. In the absence of a centralized control in the network, this simultaneous access induces significant interference. The collector receives in addition to its intended attenuated signal, the interference from all other nodes transmitting on the same sub-medium. The network parameters as well as the numerical values of the attenuation factor and the path-loss exponent are summarized in Table 3.1.

Parameter	**Value**
Carrier frequency	868 MHz
Maximum transmit power	14 dBm
Collector height	30 m
Device average height	1 m
Urban path-loss propagation	$\alpha = 10^{-10.07}$, $\beta = 3.52$
Rural path-loss propagation	$\alpha = 10^{-9.08}$, $\beta = 3.52$
Confidence level	$p_c = 10^{-2}$
Rural coverage radius R_c	10 to 30 km
Rural collector intensity λ_b	0.0015 to 0.015 collector per km^2
Urban coverage radius R_c	2 to 5 km
Urban collector intensity λ_b	0.1 to 0.3 collector per km^2

Table 3.1: System parameters

3.2.2 Chirp Spread Spectrum modulation

In a LoRa network in [12], Chirp Spread Spectrum (CSS) modulation is used to spread the signal within a limited bandwidth. This spreading technique protects the edge devices from the devices in the proximity of the network collector. The spreading factor is dictated by the receiver sensitivity and hence by the threshold communication ranges. A high spreading factor better prevents transmission errors, but at the cost of a reduced data rate. The LoRa network features 6 possible spreading factors (SF = 7 to 12). Each symbol transmits SF bits, has a time duration T and occupies a bandwidth B,

$$2^{\mathrm{SF}} = T \times B. \tag{3.4}$$

A channel coding with a rate $R_c = \frac{4}{5}$ is used, and the spectral efficiency (SE) in bits/s/Hz is,

$$\mathrm{SE(b/s/Hz)} = \frac{R_c \times \mathrm{SF}}{2^{\mathrm{SF}}}.$$

Considering that the chosen SF depends on the distance between the node and the BS, the corresponding SF of a given node x situated at a distance $|x|$ from the collector o is computed as,

$$\mathrm{SF}(x) = \sum_{\mathrm{SF}_0=7}^{12} \mathrm{SF}_0 \times \mathbb{1}_{\{x \in \mathcal{A}_{\mathrm{SF}}\}}, \tag{3.5}$$

where

$$\mathcal{A}_{\mathrm{SF}} = \{x \in \Phi_a : \rho_{\mathrm{SF}-1} \leq |x| < \rho_{\mathrm{SF}}\}, \tag{3.6}$$

and ρ_{SF} is the outer-radius for each SF region with $\rho_6 = 0$. The choice of these outer-radii will be further discussed in Section 3.5.

3.2.3 Channels allocation

We consider a LoRa network that operates on a frequency 868 MHz within a total allocated bandwidth of 1 MHz. The typical communication bandwidth in values are 125, 250 and 500 kHz in the HF-ISM 900 MHz band. For a given active node $x \in \Phi_a$, we denote by $B_a(x)$ the size of the sub-band on which the transmission occurs. In the following, we describe the fixed allocation strategy and the adaptive multi channels allocation that we introduce in this chapter.

3.2.3.1 Fixed size channel allocation

For the fixed size channels allocation policy, all the nodes in the network transmit within a fixed sub-band size B_0 chosen among $B_0 = 125, 250$ and 500 kHz, *i.e.*

$$\forall x \in \Phi_a : B_a(x) = B_0.$$

The total bandwidth of 1 MHz can be divided into $N_m = 8, 4$ or 2 depending on the fixed sub-bandwidth B_0. Each sub-band is labeled by an integer between 1 and N_m. The sensor node $x \in \Phi_a$ selects uniformly, before transmission, a random Medium Access Indicator (MAI) $e_{B_0}(x)$ from the set $\mathcal{M} = \{1, \ldots, N_m\}$ as illustrated in Figure 3.1. The authorized nodes transmit their information within the sub-band labeled by the medium access indicator.

The intra sub-band interference is induced by nodes that select the same sub-band for transmission. Each sub-band is accessible with the same probability $\mathrm{Prob}\{e_{B_0}(x) = k\} = 1/N_m, \forall\, k$. For a given node x transmitting in sub-band $e_{B_0}(x)$, the set of interference contains all nodes transmitting in the

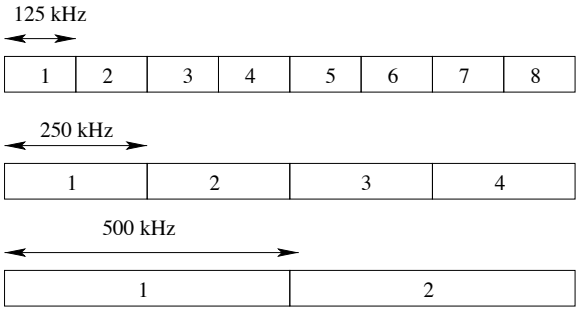

Figure 3.1: Channels labels for different bandwidth size

same sub-band, *i.e.*,

$$\Phi_i = \{y \neq x \in \Phi_a : e_{B_0}(y) = e_{B_0}(x)\}. \tag{3.7}$$

By the thinning theorem, the nodes of the set $\Phi_k \cup \{x\}$ are distributed according to a spatial PPP with an homogeneous intensity,

$$\lambda_i(y) = \lambda_a / N_m, \quad \forall y, \tag{3.8}$$

with $N_m = 8, 4$ or 2 with respect to the size of B_0.

3.2.3.2 Adaptive multi channels allocation

Although the CSS modulation protects edge cell devices from the high level of interference induced by nodes in the proximity of the collector, it fails to protect nodes at the edge of a given SF region. To solve this problem, we propose to decrease the spectral efficiency for the edge nodes of the SF regions. To perform this, we increase progressively, inside each SF region, the size of the bandwidth while keeping the same data rate as shown in Figure 3.2. Depending on the position of the sensor, the chirps are spread in one, two or four adjacent channels.

We let $\mathcal{B}_{B_0} = \{x \in \Phi_a : B_a(x) = B_0\}$ be the set of nodes transmitting within a band B_0 and $\mathcal{A}_{\mathrm{SF}} \cap \mathcal{B}_{B_0}$ the set of nodes using the same SF and bandwidth size. We denote by $d_{(\mathrm{SF},B_0)}$ the delimiting outer radius of this region.

For a given node $x \in \mathcal{A}_{\mathrm{SF}}$, the size of the sub-band allocated to this node using the adaptive multi channels policy is,

$$B_a(x) = \sum_{B_0 \in \{125,250,500\}} B_0 \times \mathbb{1}_{\{x \in \mathcal{A}_{\mathrm{SF}} \cap \mathcal{B}_{B_0}\}},$$

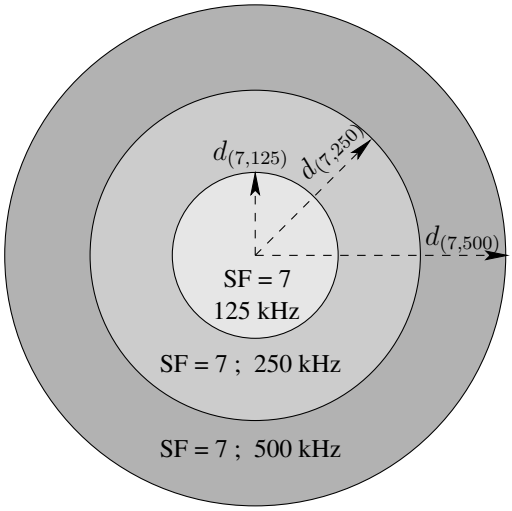

Figure 3.2: Multi channels allocation within SF zones

with

$$\mathcal{A}_{\mathrm{SF}} \cap \mathcal{B}_{B_0} = \{x \in \Phi_a : d_{\mathrm{in}} \leq |x| < d_{(\mathrm{SF},B_0)}\}$$

and

$$d_{\mathrm{in}} = \begin{cases} \rho_{\mathrm{SF}-1} & B_0 = 125 \text{ kHz}; \\ d_{(\mathrm{SF},B_0/2)} & \text{else.} \end{cases}$$

Based on the delimiting outer-radius $d_{(\mathrm{SF},B_0)}$ with $(\mathrm{SF}, B_0) \in \{7,\ldots,12\} \times \{125, 250, 500\}$ and depending on the position of a node in the cell, the SF and the size of the bandwidth are assigned. According to the size of the bandwidth $B_a(x)$, the node x selects next randomly and in a uniform way a sub-band index $e_{B_a(x)}(x)$ as illustrated in Figure 3.1. Our goal is to find the appropriate values of these communications ranges $d_{(\mathrm{SF},B_0)}$ to minimize the average outage probability in the cell. The optimized choice of these outer-radii will be further discussed in Subsection 3.5.2.

3.3 Statistical Interference Characterization

In the following, we provide a statistical model to characterize the uplink interference computed at a typical collector situated at the origin. Due to the high ranges in LoRa network, we consider only the intra-cell interference and neglect the inter-cell interference. We consider a given node x situated at distance $r = |x|$ from the typical point and transmitting with a spreading factor $\mathrm{SF}(x)$ and within a bandwidth $B_a(x)$. This latter is independent of x in the fixed size case. The interfering set Φ_i is defined in ((3.7) to (3.18)). For fixed sub-band allocation and in (3.10) to (3.18) for the adaptive

sub-band allocation. The position of a given interferer y in the cell determines its spreading factor $\mathrm{SF}(y)$ and the size of its sub-band $B_a(y)$ in the adaptive allocation case. Depending on the SF and sub-band size of the interferer as well as the intended transmitter ones, the power of the interferer is weighted by a correlation factor denoted by $c(x, y)$. Let I_x define the interference observed at the collector on a intended transmitter x. The expression of the interference I_x is then,

$$I_x \approx \sum_{y \in \Phi_i} c(x, y) P_r(y) \prod_{z \in \Phi_b} \mathbb{1}_{\{|y|<|z-y|\}}, \tag{3.9}$$

where $P_r(y)$ being the received power at the collector o from the transmitter y defined in (3.3). Note that the right hand side product in (4.4) is only equal to 1 if the sensor node y is closer to o than all other nodes of the collectors process. In the following, we first characterize the spatial distribution of the interfering nodes. Then, we compute the inter-correlation factor $c(x, y)$ and we characterize the Laplace transform expression of the interference.

3.3.1 Spatial distribution of interfering nodes

The set of the interfering nodes depends on the pre-assigned bandwidth $B_a(x)$ on which the intended node x is transmitting. The set of interfering nodes corresponds to

$$\Phi_i = \{y \in \Phi_a : \text{sub-band of y overlap with sub-band of x}\}.$$

In the following, we detail three possible cases.

3.3.1.1 Case 1: $B_a(x) = 125$ kHz

Given a device transmitting on the band $B_a(x) = 125$ kHz say with $e_{125}(x) = 3$ for example. The interference is generated by: (i) devices with band 125 kHz transmitting on sub-band 3 in Figure 3.1, (ii) devices with band 250 kHz transmitting on sub-band 2 in Figure 3.1 and (iii) devices with band 500 kHz transmitting on sub-band 1 in Figure 3.1. The set of interfering nodes Φ_i can be written as the union of three subsets such that $\Phi_i = \Phi_{i,1} \cup \Phi_{i,2} \cup \Phi_{i,3}$, with

$$\Phi_{i,1} = \{y \neq x \in \mathcal{B}_{125} : e_{125}(y) = e_{125}(x)\}, \tag{3.10}$$

$$\Phi_{i,2} = \{y \in \mathcal{B}_{250} : 2e_{250}(y) - 1 = e_{125}(x)\} \cup \{y \in \mathcal{B}_{250} : 2e_{250}(y) = e_{125}(x)\} \tag{3.11}$$

$$\begin{aligned}\Phi_{i,3} = &\{y \in \mathcal{B}_{500} : 4e_{500}(y) - 3 = e_{125}(x)\} \\ &\cup \{y \in \mathcal{B}_{500} : 4e_{500}(y) - 2 = e_{125}(x)\} \\ &\cup \{y \in \mathcal{B}_{500} : 4e_{500}(y) - 1 = e_{125}(x)\} \\ &\cup \{y \in \mathcal{B}_{500} : 4e_{500}(y) = e_{125}(x)\}\end{aligned} \tag{3.12}$$

Note that the intensity of interfering nodes in $\Phi_{i,1}$ is $\lambda_a/8$, in $\Phi_{i,2}$ is $\lambda_a/4$ and in $\Phi_{i,3}$ is $\lambda_a/2$.

3.3.1.2 Case 2: $B_a(x) = 250$ kHz

In a similar way, assuming $B_a(x) = 250$ kHz, the interference set Φ_i is $\Phi_i = \Phi_{i,1} \cup \Phi_{i,2} \cup \Phi_{i,3}$, with

$$\Phi_{i,1} = \{y \in \mathcal{B}_{125} : e_{125}(y) = 2e_{250}(x)\} \cup \{y \in \mathcal{B}_{125} : e_{125}(y) = 2e_{250}(x) - 1\} \tag{3.13}$$

$$\Phi_{i,2} = \{y \neq x \in \mathcal{B}_{250} : e_{250}(y) = e_{250}(x)\} \tag{3.14}$$

$$\Phi_{i,3} = \{y \in \mathcal{B}_{500} : 2e_{500}(y) - 1 = e_{250}(x)\} \cup \{y \in \mathcal{B}_{500} : 2e_{500}(y) = e_{250}(x)\} \tag{3.15}$$

The intensity of interfering nodes in $\Phi_{i,1}$ is $2\lambda_a/8 = \lambda_a/4$, in $\Phi_{i,2}$ is $\lambda_a/4$ and in $\Phi_{i,3}$ is $\lambda_a/2$.

3.3.1.3 Case 3: $B_a(x) = 500$ kHz

For the case with $B_a(x) = 500$ kHz, the interference set $\Phi_i = \Phi_{i,1} \cup \Phi_{i,2} \cup \Phi_{i,3}$, with

$$\begin{aligned}\Phi_{i,1} = &\{y \in \mathcal{B}_{125} : e_{125}(y) = 4e_{500}(x) - 3\} \\ &\cup \{y \in \mathcal{B}_{125} : e_{125}(y) = 4e_{500}(x) - 2\} \\ &\cup \{y \in \mathcal{B}_{125} : e_{125}(y) = 4e_{500}(x) - 1\} \\ &\cup \{y \in \mathcal{B}_{125} : e_{125}(y) = 4e_{500}(x)\}\end{aligned} \tag{3.16}$$

$$\Phi_{i,2} = \{y \in \mathcal{B}_{250} : e_{250}(y) = 2e_{500}(x) - 1\} \cup \{y \in \mathcal{B}_{250} : e_{250}(y) = 2e_{500}(x)\} \tag{3.17}$$

$$\Phi_{i,3} = \{y \neq x \in \mathcal{B}_{500} : e_{500}(y) = e_{500}(x)\} \tag{3.18}$$

The intensity of interfering nodes in $\Phi_{i,1}$ is $4 \times \lambda_a/8 = \lambda_a/2$, in $\Phi_{i,2}$ is $2\lambda_a/4 = \lambda_a/2$ and in $\Phi_{i,3}$ is $\lambda_a/2$.

Heterogeneous interfering nodes distribution

Considering the three above mentioned different cases, the set of interfering nodes on an intended node x with assigned sub-band size B_x, is distributed as a spatial PPP with heterogeneous distribution that depends on x and on the position of y and is given by,

$$\lambda_{i,x}(y) = \sum_{B_y \in \{125,250,500\}} \Lambda(B_y, B_x) \mathbb{1}_{\{y \in \mathcal{B}_{B_y} | x \in \mathcal{B}_{B_x}\}},$$

The values of $\Lambda(B_x, B_y)$ are detailed in Table 3.2 and can be deduced by considering the intensity of the sets detailed in (3.10) to (3.18).

Table 3.2: Intensity $\Lambda(B_y, B_x)$

B_y \ B_x	125	250	500
125	$\lambda_a/8$	$\lambda_a/4$	$\lambda_a/2$
250	$\lambda_a/4$	$\lambda_a/4$	$\lambda_a/2$
500	$\lambda_a/2$	$\lambda_a/2$	$\lambda_a/2$

3.3.2 Inter-correlation Factor Computation

The CSS modulation is based on chirp (obtained through a continuously varying carrier frequency [125]). A single LoRa chirp codes up to SF = 12 bits. To do so, during one chirp period, a specific frequency trajectory is defined for each of the 2^{SF} symbols. This is done by shifting the chirp based on the symbol value, so that the lowest frequency is observed at time $\frac{k}{T}$ where k is the symbol numerical value, and T the chirp duration. This introduces a sharp edge in the instantaneous frequency trajectory. Let us consider a transmitting node interfering with the intended signal. The expression for the instantaneous frequency of the interfering coded chirp is thus:

$$f_{cc}^{(k)}(t) = \begin{cases} \frac{B}{T}\left(t - \frac{k}{B}\right) + B & \text{if } -\frac{T}{2} \leq t \leq \frac{k}{B} \\ \frac{B}{T}\left(t - \frac{k}{B}\right) & \text{if } \frac{k}{B} \leq t \leq \frac{T}{2} \end{cases}. \tag{3.19}$$

with $0 \leq k \leq 2^{\mathrm{SF}} - 1$. At the receiver side, the received signal is multiplied with the raw down-chirp (supposedly perfectly synchronized) related to the desired user parameters.

The instantaneous frequency becomes:

$$f_p(t) = \Big(\Big(\frac{B}{T} - \frac{B_0}{T_0} \Big) \times t - \frac{k}{T} + B \Big) \mathbb{1}_{\{-\frac{T}{2} \leq t \leq \frac{k}{B}\}} + \Big(\Big(\frac{B}{T} - \frac{B_0}{T_0} \Big) \times t - \frac{k}{T} \Big) \mathbb{1}_{\{\frac{k}{B} \leq t \leq \frac{T}{2}\}}$$

This signal is then sampled at B_0 Hz, leading to 2^{SF_0} samples such that,

$$s\left(n\right) = A\text{exp}\left(j2\pi \int_0^{\frac{n \cdot T_0}{2^{\text{SF}_0}}} \mod \left(f_p(t), B_0\right) dt \right), \, 1 \leq n \leq 2^{\text{SF}_0}. \tag{3.20}$$

with A the amplitude coefficient which aggregates the effects of the transmitted power, channel losses, and circuit. The samples are processed with a Fast Fourier Transform (FFT) of 2^{SF_0} size. The generated contribution, which depends on the initial parameters of the encoded chirp is thus given by:

$$S_m\left(\text{SF}, B\right) = \max\left(\text{FFT}\left[s\left(1\right), ..., s\left(2^{\text{SF}_0}\right) \right] \right). \tag{3.21}$$

We can finally deduce the inter-correlation factor, by comparing the contribution of the interferer y with $\text{SF}(y) = \text{SF}_y$ and $B_a(y) = B_y$ to the desired user's x using $\text{SF}(x) = \text{SF}_x$ and $B_a(x) = B_x$ such that,

$$c(x, y) = \frac{S_m\left(\text{SF}_x, B_x\right)}{S_m\left(\text{SF}_y, B_y\right)}. \tag{3.22}$$

Note that this inter-correlation factor depends on the parameters $(\text{SF}_x, B_x, \text{SF}_y, B_y)$, and is denoted in the following as

$$c(x, y) = c_{\{\text{SF}_x, B_x, \text{SF}_y, B_y\}}.$$

The typical bandwidth values are 125, 250 and 500 kHz in the HF ISM 900 MHz band. Besides, the spreading factor SF can vary from 7 to 12. Tables 3.4 and 3.5 provide all numerical data obtained for all these cases.

3.3.3 Interference Laplace Transform Computation

Let I_x be the random interference on the signal of a given transmitter x situated at a distance r from the typical o and transmitting with $\text{SF}(x) = \text{SF}_x$ and within a sub-band $B_a(x) = B_x$. The Laplace transform of the interference I_x computed for $s \in \mathbb{R}$ is

$$\mathcal{L}_{I_x}(s) = \mathbb{E}\Big[e^{-sI_x} \Big].$$

The main results are summarized as follows.

3.3.3.1 Fixed sub-band allocation

In this case, the sub-band is fixed and is allocated independently of the node position *i.e.* $B_a(y) = B_a(x) = B_0$. Independently of the node x position in the cell, the interferer is distributed in a spatial PPP with intensity λ_a/N_m.

Proposition 3.1 *The expression of the interference Laplace transform is*

$$\mathcal{L}_{I_x}(s) = \exp\left(-\frac{\lambda_a}{N_m} 2\pi \sum_{\mathrm{SF}=7}^{12} \kappa(s)\right). \tag{3.23}$$

with

$$\kappa(s) = \int_{\rho_{\mathrm{SF}-7}}^{\rho_{\mathrm{SF}-6}} \frac{s\omega P_t \alpha r^{-\beta}}{s\omega P_t \alpha r^{-\beta} + 1}\, r\, e^{-\lambda_b \pi r^2}\, dr. \tag{3.24}$$

and $\omega = c_{\{\mathrm{SF}_x, B_0, \mathrm{SF}_y, B_0\}}$ *is the inter-correlation factor weight.*

Proof: See Appendix 3.8.1 □

3.3.3.2 Adaptive multi channels allocation

Proposition 3.2 *The expression of the Laplace transform of the interference on a transmitter x depends upon the size of its allocated bandwidth $B_a(x) = B_x$, and is given by,*

$$\mathcal{L}_{I_x}(s) = \exp\big(-2\pi g(x)\big), \tag{3.25}$$

with

$$g(x) = \sum_{\mathrm{SF}=7}^{12} \sum_{B_y \in \{125,250,500\}} \xi(s), \tag{3.26}$$

and

$$\xi(s) = \int_{u \in \mathcal{A}_{\mathrm{SF}} \cap \mathcal{B}_{B_y}} \Lambda(B_y, B_x) \frac{s\omega P_t \alpha r^{-\beta}}{s\omega P_t \alpha r^{-\beta} + 1}\, r\, e^{-\lambda_b \pi r^2}\, dr, \tag{3.27}$$

such that $\omega = c_{\{\mathrm{SF}_x, B_x, \mathrm{SF}_y, B_y\}}$ *and* $r = |u|$.

Proof: The main difference between the adaptive multi channels and fixed sub-band allocation is the spatial distribution of the PPP that becomes heterogeneous. The intensity becomes then position dependent. The expression of the Laplace transform can be deduced by repeating similar steps as the fixed sub-band allocation case, and by taking into account the heterogeneity of the spatial PPP. □

3.4 Outage Probability Computation

For a given transmitter x situated at a distance $r = |x|$ from the typical o and transmitting with $\mathrm{SF}(x) = \mathrm{SF}_x$ within a sub-band $B_a(x) = B_x$, the received SINR(x) from a sensor node x at a typical collector point o is

$$\mathrm{SINR}(x) = \frac{P_r(x)}{P_n + I_x} \tag{3.28}$$

where $P_r(x)$ is the received power in (3.3), P_n is the thermal noise, I_x is the interference and A_f the equivalent fading coefficient that is exponentially distributed. There will be a failure in the transmission if the value of SINR is less than a given threshold. This threshold is determined in order to ensure a target symbol error rate. For the fixed or the adaptive sub-band allocation, the failure probability is,

$$\mathbb{P}_{\mathrm{out}}(r) = \mathrm{Prob}\{\mathrm{SINR}(x) < \gamma_{(\mathrm{SF}_x, B_x)}\},$$

with $\gamma_{(\mathrm{SF}_x, B_x)}$ being the required threshold values according to (SF_x, B_x).

3.4.1 Threshold values

The analytical expression of symbol error rate using the LoRa PHY layer has been derived in [126] and compared to the simulation ones. These symbol error probabilities were computed for different spectral efficiencies using spreading factors SF = 7 to 12. By targeting a symbol error probability of 10^{-4}, we have deduced from [126] the values of $\gamma_{(\mathrm{SF},125)}$ in Table 3.3. When targeting the same data rate with a larger bandwidth than 125 kHz, the time dedicated to transmit the SF bits contained within a chirp should remain unchanged. Spreading the signal on a larger bandwidth of 250 or 500 kHz naturally decreases the chirp duration compared to the case of 125 kHz. Using (3.4), the chirp duration reduces to half in the case of 250 kHz and to the quarter in the case of 500 compared to the chirp duration in 125 kHz. To keep the same data rate despite the reduced chirp duration, we propose to repeat the same chirp twice for the case with 250 kHz and four times with 500 kHz. In each trial, the spectral efficiency for a given SF remains the same as in the case of 125 kHz. The chirp is completely lost if it is impossible to recover it in all the trials.

Based on this multi-trial transmission when considering multi-bands allocations within the duration of a packet of SF bits, we have deduced from [126] the values of $\gamma_{(\mathrm{SF},250)}$ and $\gamma_{(\mathrm{SF},500)}$ listed in Table 3.3.

Table 3.3: Threshold $\gamma_{(\mathrm{SF},B_x)}$ in dB

B_x \ SF	7	8	9	10	11	12
125	-7.5	-10	-12.5	-15	-18	-21
250	-9	-12	-14.5	-17	-20	-23
500	-11	-13.8	-16.5	-19	-21.8	-25

3.4.2 Outage probability

Using the distribution of the exponential distribution of the fading, the expression of the probability simplifies to

$$\mathbb{P}_{\text{out}}(r) = 1 - \mathcal{L}_{P_n}(s)\mathcal{L}_{I_x}(s), \tag{3.29}$$

with

$$s = \frac{\gamma_{(\mathrm{SF}_x,B_x)}}{\alpha r^{-\beta}\ P_t}.$$

The Laplace transform interference expressions $\mathcal{L}_I(s)$ are given in (3.23) for the fixed band case and in (3.25) for the adaptive one. The noise Laplace transform $\mathcal{L}_{P_n}(s)$ is computed as,

$$\mathcal{L}_{P_n}(s) = \frac{1}{sN_oB_x + 1},$$

and $N_o = 10^{-17.4}$ mW/Hz. Considering a single trial, the average outage probability in the typical cell is then,

$$\bar{\mathbb{P}}_{\text{out}} = \int \mathbb{P}_{\text{out}}(r) f(r) dr.$$

For a multi-independent trial transmission with L number of trials, which is the case in a LoRa network, the transmission fails if no successful transmission occurs during the L trials. The average outage probability is,

$$\bar{\mathbb{P}}_{\text{out}}(L) = \int \mathbb{P}_{\text{out}}(r)^L f(r) dr. \tag{3.30}$$

3.5 SF and Sub-Channel Allocation Policy

In this section, we detail the SF and sub-band allocation policy that we used to delimit the outer-radii of the regions with nodes sharing the same SF and the same band B_x *i.e.* $\mathcal{A}_{\mathrm{SF}} \cap \mathcal{B}_{B_x}$.

3.5.1 SF allocation policy

The outer-radii of SF zones depends on the power consumption of the devices as well as the intensity of collectors in the network and consequently the average coverage radius R_c in (3.2). The nodes situated at a distance less than R_c are assigned to the CSS with spreading factor from 7 to 11, and we set ρ_{11} to R_c *i.e.* $\rho_{11} = R_c$. The SF = 12 is left for devices tuated at a distance above R_c. One can compute the path-loss at the distance R_c and deduce the maximal required path-loss. Based on the coefficients of the Okumura Hata model in Table 3.1, the maximal path-loss in dB denoted $\mathrm{PL}_{\max}^{(11)}$ in the zone with SF = 11 is computed as,

$$\mathrm{PL}_{\max}^{(11)} = 10\log_{10}\left(\alpha R_c^{-\beta}\right).$$

As we can notice from Table 3.3, there is a gap of

$$\Delta\gamma_{(\mathrm{SF},B_x)} = \gamma_{(\mathrm{SF},B_x)} - \gamma_{(\mathrm{SF}+1,B_x)} = \Delta\gamma_{\mathrm{SF}}, \quad \forall B_x$$

when decreasing the spreading factor. The maximal path-loss in the other SF regions is then,

$$\mathrm{PL}_{\max}^{(\mathrm{SF})} = \mathrm{PL}_{\max}^{(\mathrm{SF}+1)} - \Delta\gamma_{\mathrm{SF}} \quad 7 \leq \mathrm{SF} \leq 10.$$

Based on the Okumura Hata model in Table 3.1, the outer-radius of each SF region can be computed accordingly.

3.5.2 Multiple Channels allocation policy

Given the choice of the SF outer-radius, we allocate the channels to minimize the average outage probability in the cell. The delimiting outer-radius $d_{(\mathrm{SF},B_x)}$ of the $\mathcal{A}_{\mathrm{SF}} \cap \mathcal{B}_{B_x}$ region is expressed in function of the conditional probability $p_{(B_x|\,\mathrm{SF})}$ that we define as,

$$p_{(B_x|\,\mathrm{SF})} \triangleq \mathrm{Prob}\left\{x \in \mathcal{B}_{B_x} | x \in \mathcal{A}_{\mathrm{SF}}\right\}. \tag{3.31}$$

with

$$\sum_{B_x \in \{125,250,500\}} p_{(B_x|\,\mathrm{SF})} = 1, \qquad \forall\,\mathrm{SF}\,.$$

Using the ergodicity of the spatial PPP, this probability reduces to,

$$p_{(B_x|\,\mathrm{SF})} = \frac{|\mathcal{A}_{\mathrm{SF}} \cap \mathcal{B}_{B_x}|}{|\mathcal{A}_{\mathrm{SF}}|} \tag{3.32}$$

with $|\mathcal{A}_{\mathrm{SF}} \cap \mathcal{B}_{B_x}|$ and $|\mathcal{A}_{\mathrm{SF}}|$ being the areas of $\mathcal{A}_{\mathrm{SF}} \cap \mathcal{B}_{B_x}$ and $\mathcal{A}_{\mathrm{SF}}$. Using (3.32), the delimiting outer radius of the $\mathcal{A}_{\mathrm{SF}} \cap \mathcal{B}_{B_x}$ region can be computed as,

$$d^2_{(\mathrm{SF},B_x)} = \rho^2_{\mathrm{SF}-1} + (\rho^2_{\mathrm{SF}} - \rho^2_{\mathrm{SF}-1}) \sum_{By \leq Bx} p_{(B_y|\,\mathrm{SF})}. \tag{3.33}$$

The multi channels assignment policy consists then in determining the values of the delimiting outer-radius $d_{(\mathrm{SF},B_x)}$ or equivalently $p_{(B_x|\,\mathrm{SF})}$ in order to minimize the worst case outage probability, *i.e.*,

$$\underset{p_{(B_x|\,\mathrm{SF})}}{\text{Minimize}} \quad \bar{\mathbb{P}}_{\mathrm{out}}. \tag{3.34}$$

constrained by

$$\sum_{B_x \in \{125,250,500\}} p_{(B_x|\,\mathrm{SF})} = 1, \quad 7 \leq \mathrm{SF} \leq 12.$$

Given the intensity of collectors and devices in the network, an exhaustive search solution for this optimization problem is provided in Section 3.6.

3.6 Numerical Results

We consider a cellular LoRa network with system parameters defined in Table 3.1 studied in both cases of urban and rural environments. The density of active nodes ρ_a nodes per km^2 and per min transmitting in average n_a messages a day. In rural (respectively urban) environment, we set $n_a = 2$ (respectively $n_a = 8$) and $\rho_a = 72$ (respectively $\rho_a = 360$) nodes per km^2. We assume that the mean time of service is $\nu^{-1} = 12$s. The intensity of active nodes computed as $\lambda_a = n_a \rho_a \nu^{-1}/(24 \times 60 \times 60)$ nodes per km^2 is equal to 0.02 nodes per km^2 (respectively 0.4 nodes per km^2) in rural (respectively in urban) environment.

3.6.1 Assessment of theoretical results

We compare in Figure 3.3 the simulated average outage probability and the analytic expressions in (3.29) computed in rural and urban environments considering fixed and optimized adaptive sub-band allocation. We assume that the nodes in the network transmit with maximal power of 14 dBm. The outer-radii of the SF regions are computed with respect to the collector intensities λ_b as explained in Subsection 3.5.1 to distribute the spreading factors in the whole area of coverage.

Considering the adaptive band policy, the outer-radius $d_{(\mathrm{SF},B_x)}$ of $\mathcal{A}_{\mathrm{SF}} \cap \mathcal{B}_{B_x}$ is chosen for each collector intensity case in order to minimize the average outage probability in the cell. An exhaustive

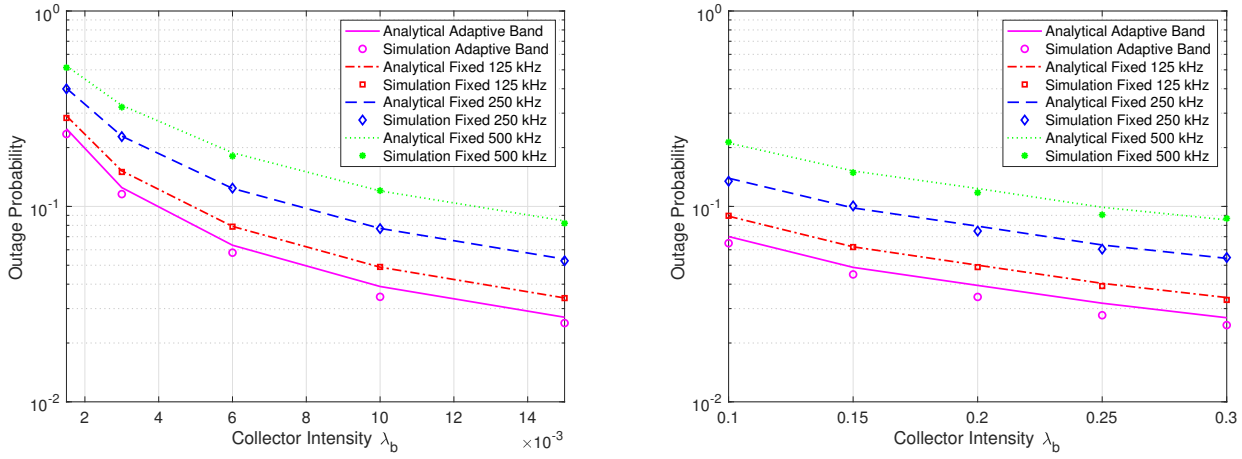

(a) Rural environment

(b) Urban environment

Figure 3.3: Comparison of analytic and simulation average outage probability computed with fixed and adaptive size of bandwidth

search is performed and the values of the conditional probabilities $p_{(B_x|\,\mathrm{SF})}$ are determined. As we can see from Figures 3.3(a) and 3.3(b) corresponding respectively to urban and rural environments, the difference between the numerical and the analytic results is negligible which validates our derived analytic results. For all policies, increasing the number of collectors reduces the size of the typical cells and enhances the level of the received SINR and consequently the outage probability. It can be observed from Figure 3.3(a) and 3.3(b) that increasing the size of the allocated fixed bandwidth increases the number of collision of the network. The interference level increases significantly and this cannot be compensated by the SINR threshold gain compared to the case of 125 kHz. For the adaptive band, the optimized choice of the outer-radius reduces the average outage probability compared to the fixed allocation policy. We can also notice that the outage probabilities have approximately the same ranges in rural and urban cases in Figure 3.3(a) and 3.3(b).This is due to the compensation of the high interference level in the highly loaded urban cell, by the path-loss of long rural communication ranges.

3.6.2 Coverage probability variation

Figure 3.4 illustrates the variation of the coverage probability (complementary event as the outage one) with distance in rural and urban network. For both cases, we can see that the use of larger

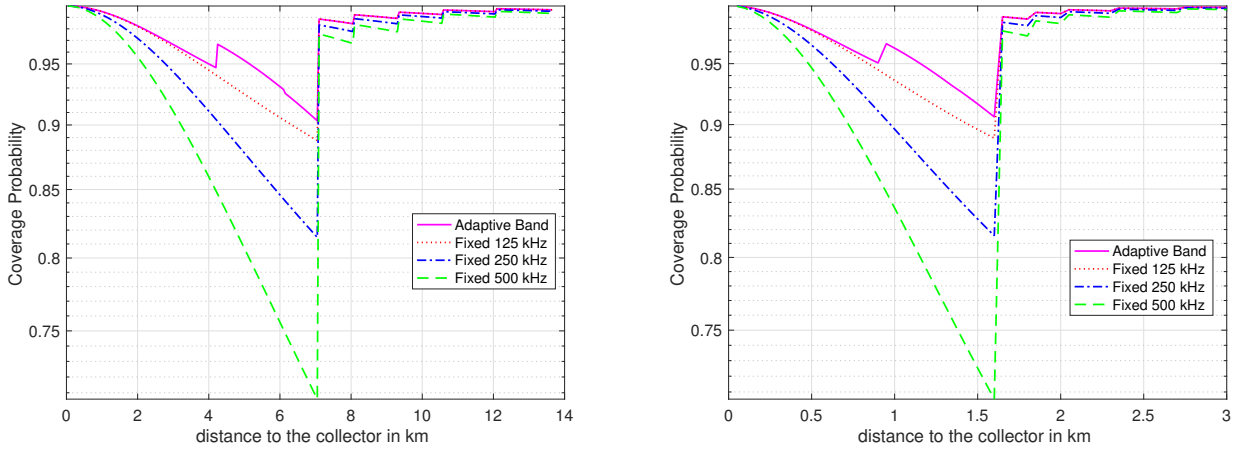

(a) Rural environment: $\lambda_b = 0.01$ collectors per km^2

(b) Urban environment: $\lambda_b = 0.2$ collectors per km^2

Figure 3.4: Variation of coverage probability with distance

bandwidth is only advantageous for nodes situated in $\mathcal{A}_7$. For larger spreading factor, decreasing the spectral efficiency by increasing the size of the bandwidth does not over-balance the high level of interference on these bands coupled with the high inter-correlation factor between the lower spreading factor and lower bandwidth. For the urban and rural environments, we can note that for nodes with fixed band allocation situated at the edge of the region $\mathcal{A}_7$ with SF 7 are highly affected by the high level of interference generated by nodes in the proximity of the collector. In this case, several trials should be performed before achieving an acceptable successful transmission rate. The nodes that are situated in the higher SF zones do not face this problem as the inter-correlation factor between the higher SF order with the SF 7 region one is low. By using the above mentioned policy, we can notice that the progressive increase of the bandwidth for nodes is only advantageous for nodes in the SF 7 region. The gain in SNR provided by the increase of the size of the bandwidth to 250 kHz in the network relatively counter-balance the high level of interference induced by the nodes in proximity to the collector. Note as the channels overlap, the density of the interfering nodes on the 250 kHz becomes higher than if we kept the 125 kHz. However, the inter-correlation factor between the channels becomes lower and compensate for this high density. For the considered node intensity, the increase of the sub-band to 500 kHz is not benefiting as the inter-correlation factor does not compensate for the high density of interfering nodes.

3.6.3 Average data-rate

Figure 3.5 compares the mean data rate considering rural and urban environments. We target a multiple trials outage probability of 10^{-4} achieved through several repetitions of the packet. These trials penalize the corresponding data rate related to each spreading factor. We can see that the adaptive band allocation policy slightly enhances the average data rate in the network compared to the other fixed band policies. Figure 3.6 compares the distribution of the rate in an urban and rural cell considering the adaptive and 125 kHz fixed allocation. In both cases, the adaptive band policy enhances the distribution of the rate in the zone with spreading factor of 7 which is naturally larger in the rural case than the urban one.

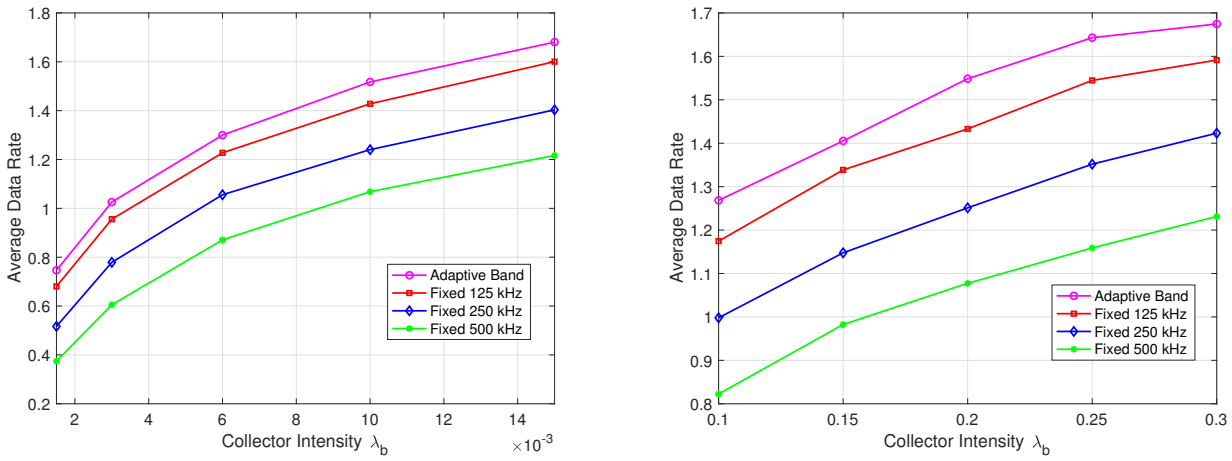

(a) Rural environment

(b) Urban environment

Figure 3.5: Average data rate in kbps versus the collector intensities

3.6.4 Maximal transmission power

Figure 3.7 illustrates the variation average outage probability considering long range rural communications in function of the maximal power of device. We can see that the adaptive band slightly enhances the power consumption compared to fixed band allocation. When targeting a single outage probability of 4×10^{-2} with a single trial, the required maximal probability with adaptive band is 12 dBm compared to 14 dBm with 125 kHz fixed band. The adaptive band allocation policy can enhance the maximal device power consumption.

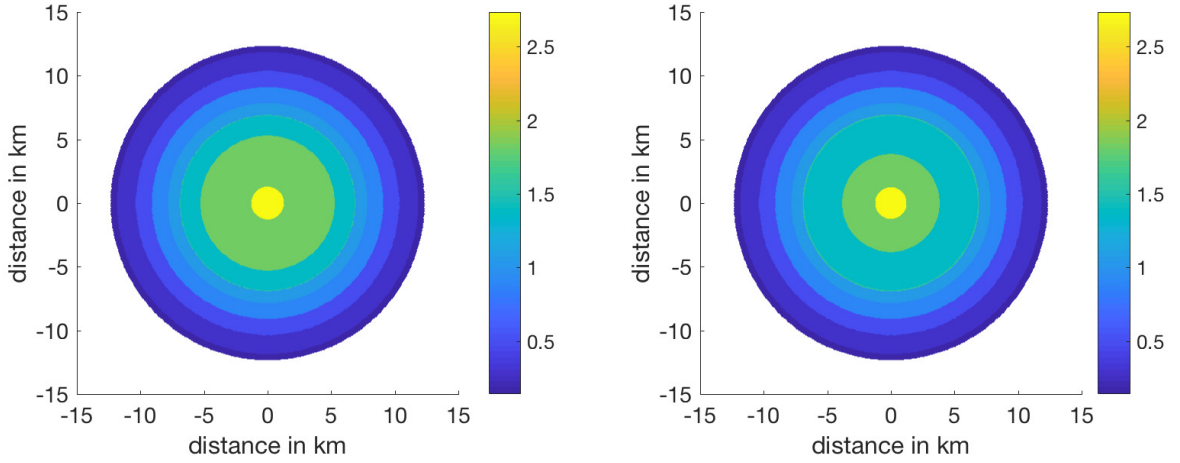

(a) Rural environment: $\lambda_b = 0.01$ collectors per km^2

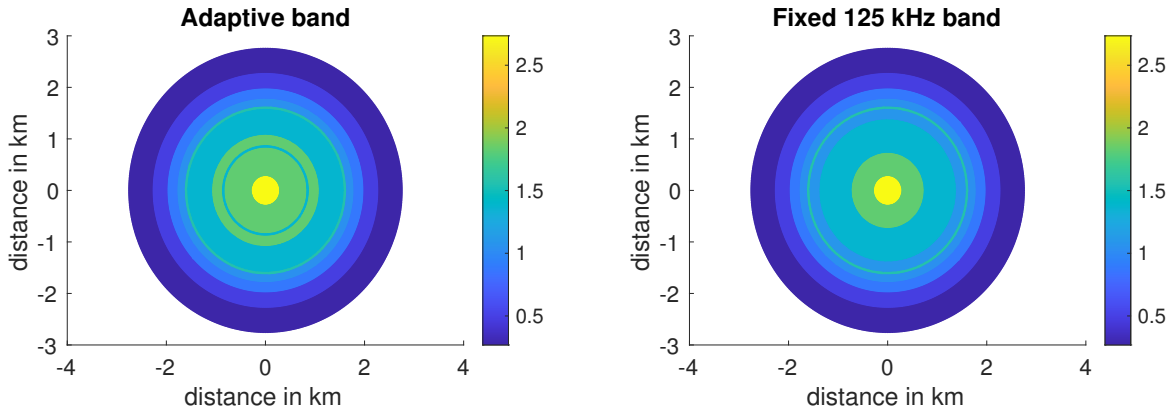

(b) Urban environment: $\lambda_b = 0.2$ collectors per km^2

Figure 3.6: Rate distribution in kbps in the cell

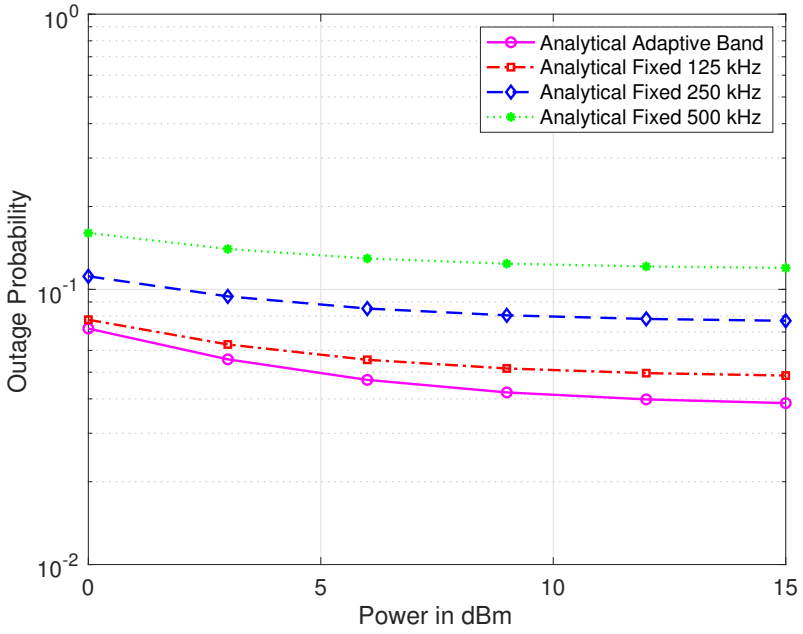

Figure 3.7: Outage probability versus the maximal transmitted power- Rural environment $\lambda_b = 0.01$ collectors per km^2.

Figure 3.8 shows the variation of the rate with the maximal transmitted power considering a multiple-trial threshold outage probability of 10^{-4}. We can see that for low power consumption, the data rate is much more penalized by the number of trials that should be performed. The adaptive allocation policy slightly enhances the data rate when increasing the power compared to other fixed allocation policies.

3.7 Conclusion

In this chapter, we proposed an adaptive bandwidth allocation policy compatible with the long range IoT LoRa networks specifications to mitigate the high interference level induced by nodes transmitting with the same SF. With respect to the distance to the station, a joint allocation of SF and one, two or four sub-channels of 125 kHz are allocated to a single sensor device. By modeling the network using spatial PPPs, we have statistically characterized an approximation of the interference Laplace transform in a typical cell taking into account the inter-correlation factor between the different spreading factors as well as the different allocated bandwidth. For this policy, we have derived the analytical expression of the outage probability. Based on this expression, we have computed in each

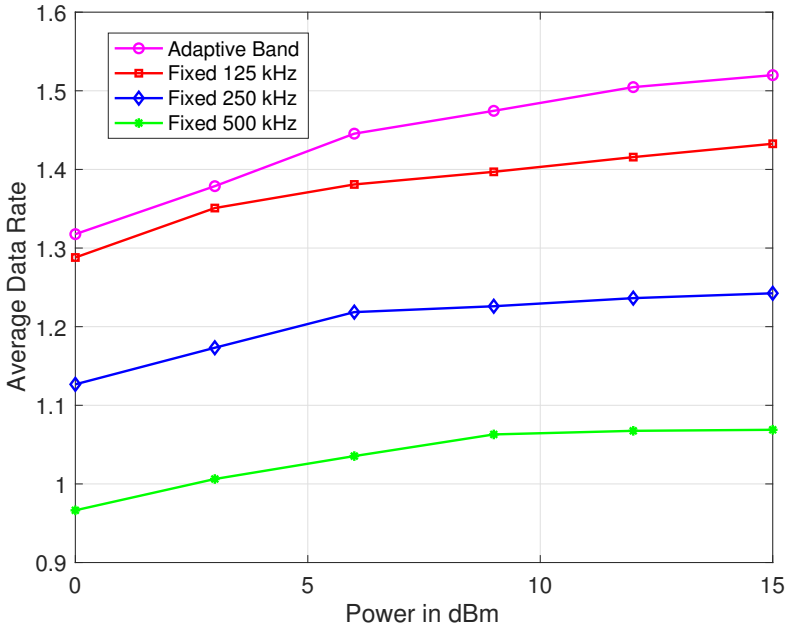

Figure 3.8: Average data rate versus the device power - Rural environment $\lambda_b = 0.01$ collectors per km^2.

SF region the outer-radius of the region where a larger bandwidth is required to minimize the average outage probability. We have shown that the optimized adaptive sub-band allocation outperforms the average outage probabilities with fixed allocation policy. Moreover, it minimizes the device power consumption and enhances the distribution of the rate in the cell by statistically decreasing the required number of trials for the edge nodes using the SF of 7. These results can be of high utility for network planners to find the dimensioning parameters of the network: the gateways' intensities, the maximal power consumption and to estimate the average data rate distribution in the network.

To ensure a mathematical tractability using stochastic geometry tools, we have defined in this chapter SF regions where the SF remains constant within a given communication range. In the next chapter, we consider a more flexible framework based on machine learning where a dynamic allocation of the spreading factor is enabled.

3.8 Appendices

3.8.1 Proof of Proposition 3.1

The interference Laplace transform is written as

$$\mathcal{L}_{I_x}(s) = \mathbb{E}\Big[e^{-s\sum_{y\in\Phi_i} g(x,y)}\Big] = \mathbb{E}\Big[\prod_{y\in\Phi_i} e^{-sg(x,y)}\Big].$$

with

$$g(x,y) = c(x,y)\alpha|y|^{-\beta}A_f P_t \prod_{z\in\Phi_b} \mathbb{1}_{\{|y|<|z-y|\}}.$$

Note that $c(x,y) = c_{\{\mathrm{SF}_0,B_0,\mathrm{SF},B_0\}} \times \mathbb{1}_{\{y\in\mathcal{A}_{\mathrm{SF}}\}}$ and $\mathcal{A}_{\mathrm{SF}}$ defined in (3.6). Next, we rewrite $e^{-sg(x,y)}$ as,

$$e^{-sg(x,y)} = 1 - (1 - e^{-sc(x,y)\alpha|y|^{-\beta}A_f P_t}) \prod_{z\in\Phi_b} \mathbb{1}_{\{|y|<|z-y|\}}.$$

For the fixed sub-band allocation case, the interferers are distributed in an homogeneous PPP with intensity λ_a/N_m. By applying the Probability Generating Functional (PGFL) property,

$$\mathcal{L}_{I_x}(s) = \exp\Big(-\frac{\lambda_a}{N_m}\mathbb{E}_z\Big[\int (1 - e^{-sg(x,y)}) f(A_f) dA_f dy\Big]\Big),$$

with $f(A_f) = e^{-A_f}$ being the exponential distribution of A_f. Focusing now on the integral on the right hand side, this latter can be written as,

$$\text{RHS integral} = \int_0^\infty \int_0^{2\pi} \int_0^\infty (1 - e^{-sc(x,y)\alpha r^{-\beta}A_f P_t}) \times \mathbb{E}_z\Big[\prod_{z\in\Phi_b} \mathbb{1}_{\{|y|<|z-y|\}}\Big] e^{-A_f} r dr\ d\theta\ dA_f \quad (3.35)$$

As in the previous chapter,

$$\mathbb{E}\Big[\prod_{z\in\Phi_b} \mathbb{1}_{\{r<|z-y|\}}\Big] = \exp(-\lambda_b \pi r^2).$$

Replacing $c(x,y)$ by its value, we can get the expression of $\mathcal{L}_{I_x}(s)$ in (3.23).

	SF_y	7			8			9		
SF_x	B_y / B_x	125	250	500	125	250	500	125	250	500
7	125	0	21.07	21.07	16.67	21.07	21.07	18.20	0	21.07
	250	12.41	0	21.07	13.33	16.67	21.07	13.66	18.20	0
	500	13.80	12.41	0	13.51	13.33	16.67	13.73	13.66	18.20
8	125	24.08	24.08	24.08	0	24.08	24.08	19.70	24.08	24.08
	250	19.70	24.08	24.08	15.42	0	24.08	16.23	19.70	24.08
	500	16.38	19.70	24.08	16.46	15.42	0	16.57	16.23	19.70
9	125	27.09	27.09	27.09	27.09	27.09	27.09	0	27.09	27.09
	250	6.02	27.09	27.09	22.71	27.09	27.09	18.39	0	27.09
	500	24.60	6.02	27.09	18.96	22.71	27.09	19.45	18.39	0
10	125	30.10	30.10	30.10	30.10	30.10	30.10	30.10	30.10	30.10
	250	27.51	30.10	30.10	6.02	30.10	30.10	25.73	30.10	30.10
	500	25.72	27.51	30.10	27.57	6.02	30.10	22.15	25.73	30.10
11	125	33.11	33.11	33.11	33.11	33.11	33.11	33.11	33.11	33.11
	250	28.30	33.11	33.11	30.55	33.11	33.11	6.020	33.11	33.11
	500	12.04	28.30	33.11	28.73	30.55	33.11	30.56	6.02	33.11
12	125	36.12	36.12	36.12	36.12	36.12	36.12	36.12	36.12	36.12
	250	30.92	36.12	36.12	31.49	36.12	36.12	33.57	36.12	36.12
	500	33.53	30.92	36.12	12.04	31.49	36.12	31.75	33.57	36.12

Table 3.4: Inter-correlation factors $c_{\{SF_x,B_x,SF_y,B_y\}}$ in dB, x is the intended device and y the interfering device

	SF_y	10			11			12		
SF_x	B_y / B_x	125	250	500	125	250	500	125	250	500
7	125	18.62	16.45	18.51	18.70	18.14	0	18.65	18.60	16.46
	250	14.01	18.62	16.46	13.98	18.70	18.15	13.74	18.65	18.60
	500	13.87	14.01	18.62	14.19	13.98	18.7	13.9	13.74	18.65
8	125	21.27	0	24.08	21.75	19.54	21.52	21.82	21.21	0
	250	16.65	21.27	0	16.90	21.75	19.54	17.00	21.82	21.21
	500	16.60	16.65	21.27	16.61	16.9	21.75	16.75	17.00	21.82
9	125	22.71	27.09	27.09	24.34	0	27.09	24.85	22.60	24.54
	250	19.17	22.71	27.09	19.66	24.34	0	19.79	24.85	22.60
	500	19.76	19.17	22.71	19.75	19.66	24.34	19.68	19.79	24.85
10	125	0	30.10	30.10	25.73	30.10	30.10	27.38	0	30.10
	250	21.43	0	30.10	22.08	25.73	30.10	22.56	27.39	0
	500	22.44	21.43	0	22.79	22.08	30.10	22.60	22.56	27.39
11	125	33.11	33.11	33.11	0	33.11	33.11	28.73	33.11	33.11
	250	28.73	33.11	33.11	24.44	0	33.11	25.10	28.73	33.11
	500	25.13	28.73	33.11	25.42	24.44	33.11	25.68	25.10	28.73
12	125	36.12	36.12	36.12	36.12	36.12	36.12	0	36.12	36.12
	250	6.02	36.12	36.12	31.74	36.12	36.12	27.46	0	36.12
	500	33.55	6.02	36.12	28.11	31.74	36.12	28.45	27.46	0

Table 3.5: Inter-correlation values $c_{\{SF_x,B_x,SF_y,B_y\}}$ in dB, x is the intended device and y the interfering device

Chapter 4

Multi-Agent Q-Learning for Resource Allocation in LoRa Networks

In this chapter, a Q-Learning approach is introduced to improve the energy efficiency and communication reliability in the uplink of the unlicensed LoRa networks. We propose a multi-agent Q-Learning algorithm to jointly optimize the Spreading Factor (SF) allocation and the power control of active sensor devices. The choice of SF and the transmit power is performed to consume the less possible power while guaranteeing that the connection between the device and the gateway is not in outage. Compared to the stochastic geometry approach, this approach enables dynamic allocation of the spreading factors and the transmit power at the sensor devices. Our numerical results show that, this Q-learning approach outperforms the static approach in terms of energy consumption.

4.1 Introduction

Reinforcement Learning (RL) is a branch of Machine Learning (ML) techniques which is of great interest because of its large number of practical applications in control engineering, multi agent systems and operation research. It is an efficient and dynamic decision-making tool. RL is different from supervised and unsupervised learning. Supervised learning learns a function through the training data which consists of a set of labeled input and corresponding output. Then it gives the predicted output of the new input data. It is often used in classification, regression problems, etc. Unsupervised learning, on the other hand, finds hidden patterns in it through unlabeled data, usually applied in clustering and downscaling, etc. Thanks to the environment-agent interaction scheme in RL, it enables a system to be controlled in such a way as to maximize a numerical measure of performance that expresses

a long-term objective [127]. It shows great potential for system controls in real engineering cases. In particular, we are interested in this chapter in the Q-learning which is a popular RL algorithm. It adopts off-policy Temporal-Difference (TD) methods for agents to learn how to act optimally to control problems. Considering multi-agent systems in a variety of fields, including robotics, distributed control, and telecommunications, multi agent Q-learning algorithm gives outstanding performance in decision-making problems for these complicated scenarios [39, 40, 41, 42].

Based on it, we propose in this chapter to apply it to the SF and power allocation problems in LPWAN. LPWAN is well suited for massive IoT network deployment as it can provide long-range, wide-area, low-power consumption communications for thousands of connected devices. There are different types of low power wide area communication technologies on the market, i.e unlicensed LoRa [12, 13] and Sigfox [128] technologies and licensed NB-IoT technology [14, 15], etc. In this chapter, we focus on LoRa network. LoRa technology uses Chirp Spread Spectrum modulation which allocates spreading factors to each active sensor node to mitigate destructive collisions in the overall network. Higher spreading factors can protect the devices from the interference caused by signals transmitted simultaneously from devices closer to the collector. To improve network reliability, we need to assign different spreading factors in an adaptive way to the active sensors. In LPWAN, energy efficiency always attracts a lot of attention. Normally, a single IoT module is expected to serve for around ten years with very low energy consumption. By reducing power consumption during each message transmission for uplink communications in LPWAN, it can improve the lifetime of IoT devices and offer remarkable financial benefits. In this chapter, we fully consider the energy efficiency by select distinct transmit power values for each sensor node for uplink communications to achieve a better power control solution for LoRa network. Some relative work has been done by using different methods. For example, in [43], a power, channel and spreading factor selection algorithm is proposed to avoid near-far problem and decrease the packet error rate in LoRa network. A distributed learning approach is introduced for self-organized LoRa networks in [129]. Inspired by them, we use multi-agent Q-learning approach to solve the concerned power and SF allocation problems dynamically.

The rest of the chapter is organized as following. An unlicensed LoRa network model is defined in Section 4.2. Then, we review in Section 4.3 the multi-agent Q-learning scheme. Next, in Section 4.4, multi-agent Q-learning algorithm is applied to solve the problems of SF selection and power allocation in LoRa network. In Section 4.5, the performance evaluation in resource allocation with respect to

network reliability and power efficiency is presented. Finally, Section 4.6 concludes this part.

4.2 LoRa Network Model

In this section, we consider a single unlicensed LoRa network cell. The cell coverage radius is R. We assume that the collector is located in the cell center and the N active sensor nodes are randomly distributed in the given cell. Let $|x|$ denotes the distance between the active sensor node x and the collector o. The out-of-cell interference is ignored in our case. Considering the uplink transmission of LoRa network, each active sensor has 5 different choices for the transmission power P_t: 2, 5, 8, 11 and 14 dBm [43]. The sensor nodes and the collector have omnidirectional antennas with 0 dBi of antenna gains. For the sensor node x, the received power P_r at the collector is:

$$P_r(x) = P_t \alpha |x|^{-\beta} A_f, \tag{4.1}$$

where α and β are respectively the attenuation factor and the path-loss exponent that are computed from Okumura-Hata model. A_f is the random fading coefficient with Rayleigh distribution.

The LoRa network adopts CSS modulation, which is a spread-spectrum technology[12, 72, 17]. According to [130], CSS modulation has several key properties, it offers high robustness and resists the Doppler effect while having a low latency. In LoRa network, the active sensors located far away from the collector suffer the collision caused by sensors that are closer to the collector. This CSS spreading technique can protect the cell edge sensor nodes from the nodes in the proximity of the network collector. It features 6 possible spreading factors (SF = 7 to 12) to the active sensors according to the receiver sensitivity and hence by the threshold communication ranges. Table 4.1 shows the corresponding SINR threshold ranges according to the values of SF with the sub-bandwidth equal to 125 kHz. With CSS modulation, each symbol transmits SF bits, has a time duration T and occupies a bandwidth B, we have

$$2^{\mathrm{SF}} = T \times B \tag{4.2}$$

For the same sub-bandwidth, the high spreading factor transmits longer time on air which means the communication distance increases. Concern the data rate R_b (bits/s),

$$R_b = \mathrm{SF} \times \frac{B}{2^{\mathrm{SF}}} \frac{4}{(4+CR)} \tag{4.3}$$

with CR being the code rate. A high spreading factor better prevents transmission errors, but at the cost of a reduced data rate. LoRa network uses high spreading factors for the weak signal or the signal suffering high interference.

SF	Rate (kbps)	SINR (dB)	S_r (dBm)	ρ (km)
7	5.4	-7.5	-124	11.43
8	3.12	-10	-127	13.9
9	1.76	-12.5	-130	17
10	0.98	-15	-133	20.6
11	0.5	-18	-135	23.5
12	0.3	-21	-137	26.8

Table 4.1: CSS LoRa parameters with sub-bandwidth B = 125 kHz

In this chapter, our objective is to manage the resource allocation in a dynamic manner. Transmission power and SF are allocated to each active sensor node to ensure the overall network communications. We aim at increasing the communication reliability for each sensor while keeping the energy consumption as low as possible. In LoRa network, the access to the shared medium is managed by Aloha protocol. The transmitted signals on the same sub-medium interfere with each other. The collector receives in addition to its intended attenuated signal. Assume that Φ_i denotes the set of interfering nodes. For an intended signal sent by node x, the interferer $y \in \Phi_i$. The power of the interference is weighted by a correlation factor denoted by $c(x, y)$. The expression of the interference is then,

$$I_x \approx \sum_{y \in \Phi_i} c(x, y) \alpha |y|^{-\beta} A_f P_t(y), \tag{4.4}$$

where α and β are respectively the attenuation factor and the path-loss exponent that are computed from the Okumura-Hata model, A_f is the random fading coefficient that is exponentially distributed and $P_t(y)$ is the transmit power of interferer y. The inter-correlation factor $c(x, y)$ is calculated in [44]. Table 4.2 presents the $c(x, y)$ values according to different spreading factors of the transmitter x and the receiver y with the sub-bandwidth of 125 kHz. The received SINR for the sensor node x at the given collector o is calculated as follows,

$$\text{SINR}_x = \frac{P_t \alpha \, |x|^{-\beta} \, A_f}{P_n + I_x}, \tag{4.5}$$

with $P_n = KTB$ being the additive thermal noise, K is the Boltzmann constant, T is the noise temperature and B is the bandwidth.

SF	7	8	9	10	11	12
7	0	16.67	18.20	18.62	18.70	18.65
8	24.08	0	19.70	21.27	21.75	21.82
9	27.09	27.09	0	22.71	24.34	24.85
10	30.10	30.10	30.10	0	25.73	27.38
11	33.11	33.11	33.11	33.11	0	28.73
12	36.12	36.12	36.12	36.12	36.12	0

Table 4.2: The inter-correlation factor $c(x, y)$ with sub-bandwidth $B = 125$ kHz

4.3 Multi-Agent Q-Learning Algorithm

Reinforcement Learning has been widely used recently in decision-making systems. It is based on Markov Decision Processes (MDPs). In MDPs, we consider a set of elements consisting of state S, action A, state transition probability $P(S'|S, A)$ Figure 4.1 demonstrates the general RL framework. The environment and the agent can have interaction and learn from it to make decisions. S is the set of possible environment states. At time t, observing the environment, a state $s \in S$ is observed and passed to the agent. Then, according to the policy π, the agent decides to take action $a \in A$, where A is the set of actions available for state s. As a is performed, the agent earns a reward $r(s, a)$ and the environment turns to a new state s'.

Since the agent determines a policy π, the choose of action a in a given state s can be described as $\pi(s) = a$. To evaluate the performance of policy π, the state-action value function $Q(s, a)$ is introduced as follows:

$$Q(s, a) = \mathbb{E}\left[G_t | s_t = s, a_t = a\right], \tag{4.6}$$

where G_t is the discounted future cumulative reward,

$$G_t = r_t + \gamma r_{t+1} + \gamma^2 r_{t+2} + \cdots + \gamma^{n-t} r_n, \tag{4.7}$$

with γ as the discount factor which is a constant and $\gamma \in [0, 1]$. The objective of reinforcement learning

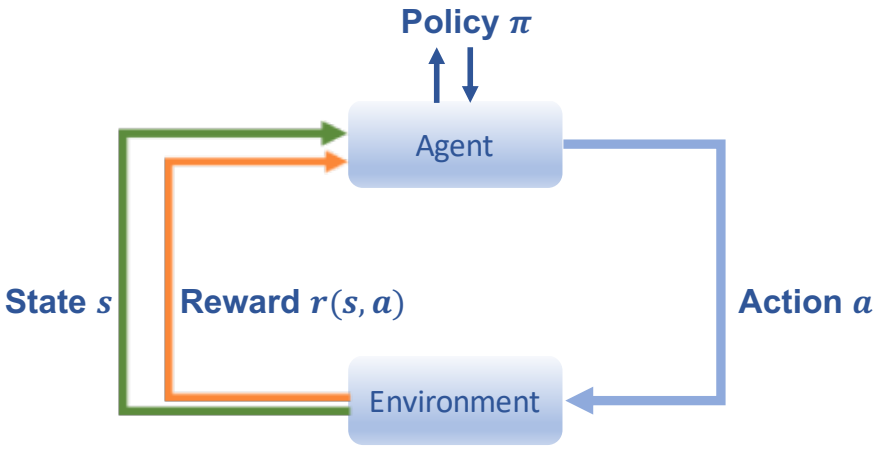

Figure 4.1: General Reinforcement Learning Framework

is to find the best policy $\pi^\star$ that maximizes the state-action value function which can be described as:

$$\pi^\star(s) = \arg\max_{a \in A} Q(s, a). \tag{4.8}$$

Q-learning Function Q-learning uses a non-deterministic policy, i.e. a function mapping each state to a set of actions so that the agent can choose one among them, while it is based on a sampling of other policies instead of the current policy alone. The Q-learning process keeps an estimate and an update of the Q-function, it can be written as follows:

$$Q(s, a) = Q(s, a) + \sigma \left\{ r(s, a) + \gamma \max_{a \in A} Q\left(s', a'\right) - Q(s, a) \right\}, \tag{4.9}$$

where $\sigma \in [0, 1]$ is a learning rate.

Multi-Agent Q-Learning Algorithm Assume that there are n agents in the system. At a given time t, action $\boldsymbol{a} = \{a_1, a_2, ..., a_n\}$ is executed by all the agents with $a_i \in A$ being the action chosen by the i-th agent. Observing the environment, a current state $s \in S$ and a total reward $r(s, \boldsymbol{a})$ are obtained and passed to all the agents. Based on state s and reward r, each agent updates its own Q-learning function and chooses a new action $a_i{}'$ for next operation separately. Then, the action $\boldsymbol{a}' = \{a_1', a_2', ..., a_n'\}$ is executed. The workflow of multi-agent Q-learning keeps the same as the single-agent Q-learning algorithm. But the state and reward information are distributed to all the agents and then a decision is made by each agent independently.

4.4 Multi-Agent Q-Learning for SF and Power Allocation

The framework of multi agent Q-learning is presented in Section 4.3. In this section, we apply the multi-agent Q-learning algorithm to solve the problems of SF allocation and power control in a licensed-exempted LoRa network. According to the network model mentioned in Section 4.2, for each active sensor node connected to the collector o, it must be assigned one SF value among 6 possible spreading factors $[7, 8, 9, 10, 11, 12]$ and one transmit power value out of 5 achievable transmit power values including $[2, 5, 8, 11, 14]$ dBm.

Algorithm 1 Multi-agent Q-learning algorithm for SF allocation and Power Control in LoRa Networks

Input: Positions of N active sensor nodes

Output: SF and transmit power values for each active sensors

Sort N sensor nodes by distance to the collector from near to far;
Set $n = N$ agents and generate n Q-learning function $Q_i(S, A), i \in [1, n]$;
Initialize each Q-learning function $Q_i(S, A), i \in [1, n]$ with random values;
for episode $= 1, M$ **do**
  Set the initial observation state s.
  for $t = 1$: until s is a terminal state **do**
    For each agent:
    with the probability ϵ select a random action $a_i = (SF, P_t)$,
    otherwise select $a_i = \max_a Q_i(s, a_i)$;
    Execute action $\boldsymbol{a} = \{a_1, a_2, ..., a_n\}$ in emulator and observe reward r and state s';
    If s' is a terminal state, set the value function target y_i to $r(s, \boldsymbol{a})$;
    Otherwise set it to: $y_i = r(s, \boldsymbol{a}) + \gamma \max_a Q_i(s', a_i)$;
    Compute the critic parameter update $\Delta Q_i = y_i - Q_i(s, a_i)$;
    Update the critic using the learning rate σ:
    $Q_i(s, a_i) = Q_i(s, a_i) + \sigma \times \Delta Q_i$;
    Set the observation state s to s'
  end for
end for
return Results

Following the multi-agent Q-learning algorithm, the LoRa network model is the environment that provides the state s and reward r information for the agents. We set $n = N$ agents for the system. Each agent corresponding to an active sensor node. A single agent here is a Q-learning function which selects an action for an active node. The action is a pair of SF and P_t values with probability ϵ or selects an action with probability $(1 - \epsilon)$ by maximizing the Q value,

$$a_i = \arg\max_a Q_i\left(s, a_i\right).$$

After the execution of the action $\boldsymbol{a_i}$, the agents obtain the new state information $s \to s'$ and a reward r. Considering the network reliability and the power efficiency, the reward r_i for the i-th sensor node is calculated as follows:

$$r_i = \delta_i(t) \times \varphi + \delta_i(t) \times (1 - \varphi) \times \frac{P_{t\,max}}{P_t}. \tag{4.10}$$

where φ is a design parameter offering a tradeoff between the network reliability and energy efficiency. P_t is the transmit power for the i-th sensor node. $\delta_i(t) \in \{0, 1\}$ which indicates whether the i-th sensor has a stable connection to the collector o or not. With a given SF value SF_i and a transmit power P_t for the i-th sensor node, we can calculate the SINR_i on the collector side for each sensor node. In Table 3.2, the SINR threshold γ_{SF} for different SF values is given in detail. Hence, if $\text{SINR}_i \geqslant \gamma_{SF_i}$, the i-th node can successfully send the message to the collector. Otherwise, the transmission fails.

$$\delta_i(t) = \begin{cases} 1 & \text{SINR}_i \geqslant \gamma_{SF_i} \\ 0 & \text{SINR}_i < \gamma_{SF_i} \end{cases} \tag{4.11}$$

The state of the environment after the execution of the action $\boldsymbol{a}$ is the decimal value corresponding to a binary number consists of all the δ_i. For example, if the number of agents n is equal to 5. There are $2^5 = 32$ states ranging from 0 to 31. At time t, if $\{\delta_1\delta_2...\delta_5\} = \{10110\}$, then the state equals 22 which is the decimal value for this binary number. Obviously, the terminal state is when all the $\delta_i = 1$. In case $n = 5$, the terminal state $s = 31$. The total reward for the action $\boldsymbol{a}$ is then calculated as follows:

$$r(s, \boldsymbol{a}) = \frac{1}{N}\sum_{i=1}^{N} r_i. \tag{4.12}$$

Algorithm 1 demonstrates the selection of SF and transmit power for the active sensors in LoRa with multi-agent Q-learning algorithm.

Parameter	Value
Carrier frequency	868 MHz
Sub-bandwidth	$B = 125$ kHz
Coverage radius	$R = 10$ km
Transmit power	$[2, 5, 8, 11, 14]$ dBm
Spreading factor	$[7, 8, 9, 10, 11, 12]$
Collector height	30 m
Device average height	1 m
Antenna gain	0 dBi
Urban path-loss model	$\alpha = 10^{-10.07}, \beta = 3.52$

Table 4.3: Network parameters

4.5 Numerical Results

In this section, we numerically evaluate the performance of the multi-agent Q-learning algorithm applied in SF selection and power allocation in LoRa network with respect to network reliability and power efficiency. We consider a single LoRa network cell with coverage radius of $R = 10$ km. Assume that N sensor nodes are activated simultaneously with random positions. The sensor nodes and the collector have omnidirectional antennas. Nodes transmitting in the same frequency band generate additive interference with power. The power of the additive thermal noise is $N_0 = KTB$ with $K = 1.379 \times 10^{-23}$ W Hz^{-1} K^{-1}, $T = 290$ K and $B = 125$ kHz. The system parameters are shown in detail in Table 4.3. We assume without loss of generality a Q-learning algorithm with 5 agents. Set the learning rate $\sigma = 0.9$. The expected SF and transmit power values for all 5 nodes are generated by Algorithm 1 after the training. Figure 4.2 shows the distribution of active nodes for 500 times of simulation with 5 agents. There are 30 different colors which represent 30 pairs of SF and P_t values. We can notice that the joint allocated SF and transmission power is made in a dynamic way depending on the instantaneous network configuration. To make a comparison with our multi-agent Q-learning algorithm, we introduce a static allocation algorithm in which the whole cell is divided into 30 rings. Within each ring, a static SF and P_t is attributed to the active nodes depending on its location. Low SF and low power are attributed to the nodes in the proximity of the collector.

Figure 4.3 illustrates the Cumulative Distribution Function (CDF) of the SINR. Multi-agent Q-learning algorithm outperforms the static one which means the former has higher reliability then the

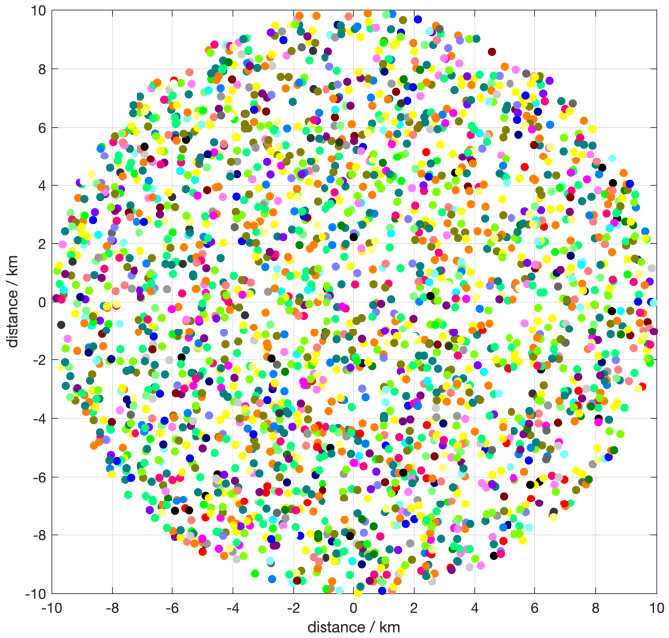

Figure 4.2: The distribution of active sensor nodes in a single cell with different choices of SF and transmit power

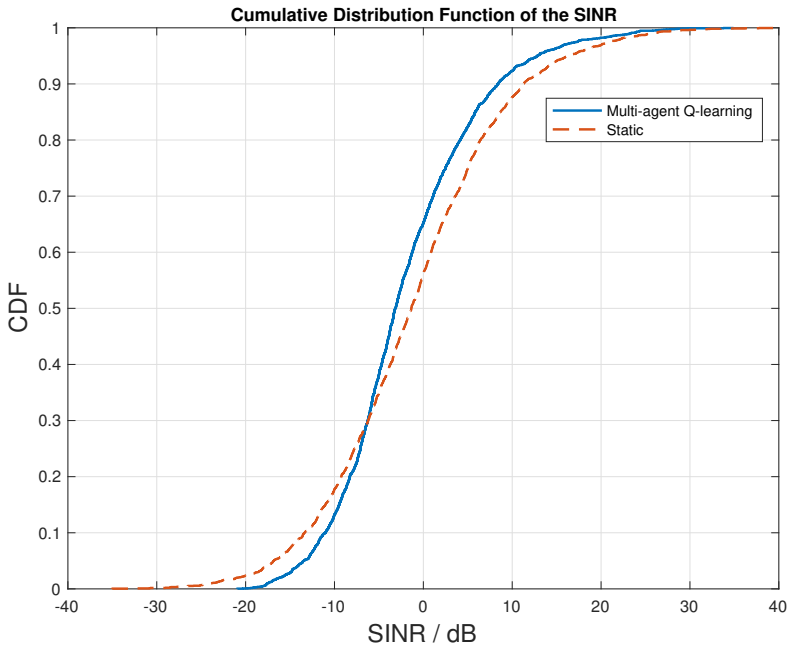

Figure 4.3: The Cumulative distribution function of the SINR

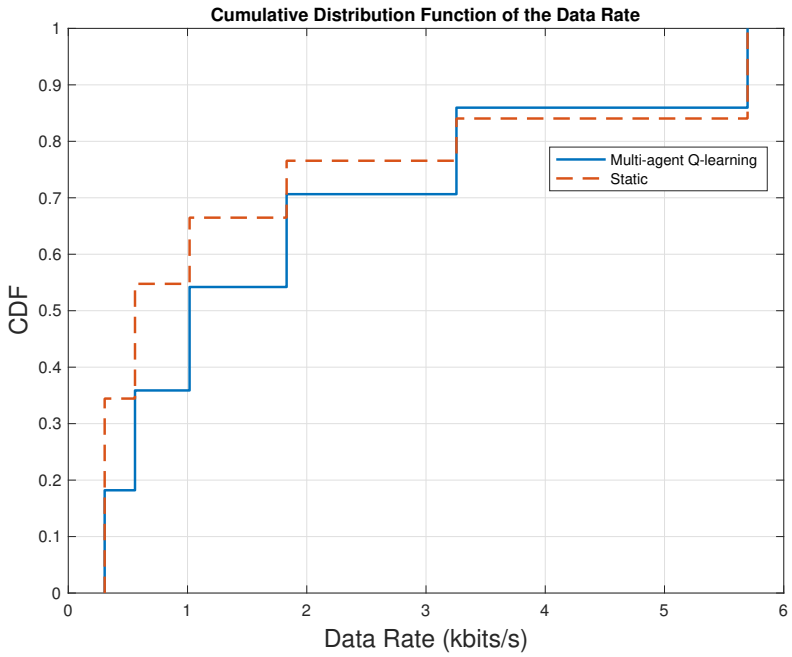

Figure 4.4: The Cumulative distribution function of the Data Rate

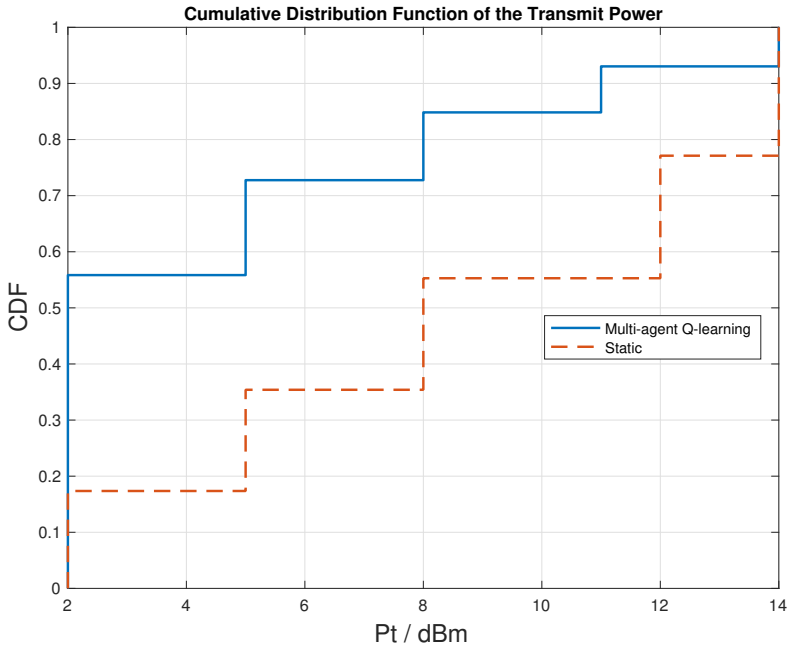

Figure 4.5: The Cumulative distribution function of the Transmit Power

latter. Meanwhile, it also achieves higher data rate during the transmission as shown in Figure 4.4.

Figure 4.5 presents the comparison of the CDF of transmit power for all sensor nodes based on two different algorithms. Our multi-agent Q-learning algorithm shows large improvements in the energy efficiency. Using the multi-agent Q-learning algorithm, the average value of the transmit power for all active sensors is equal to 4.81 dBm while for the static algorithm it is 8.66 dBm.

4.6 Conclusion

In this chapter, we have proposed a multi-agent Q-learning algorithm to jointly allocate a SF and power in the uplink of LoRa network. Each agent has interactions with the environment and based on that, it updates dynamically the policy. We have also evaluated its reliability and energy efficiency performance and compared it with a static allocation algorithm. The simulation results show the advantages of our Q-learning algorithm with respect to SINR, data rate and transmit power. So far, in this chapter and the previous chapter, we have used dynamic multi-agent Q-learning and statistical dimensioning methods to allocate resources in the LoRa networks, respectively. Each of the two different approaches has significant gains, taking into account different network performance including energy efficiency, network outage probability, data rate, spectral efficiency and so on.

Conclusion and Perspectives

This thesis focuses on the topic of power control and resource planning in LPWAN. In Chapter 1, we gave an overview on the recent development of IoT technology and the high economic value it has created. Some examples of practical applications of IoT technologies are listed and analyzed. Our focus is on LPWAN technologies that offer long range, low power consumption, long battery life and low cost IoT communication. More specifically, the LPWAN includes different technologies, licensed NB-IoT, LTE-M and unlicensed LoRa, Sigfox, etc. Around these technical standards, this chapter presents the relevant technical context, the direction of development, etc. Next, the application of multi-antenna technology in IoT networks is presented. Other relevant mathematical tools applied in this thesis are also provided, such as PPP and Q-learning.

In Chapter 2, we have elaborated the problem of network dimensioning in the uplink of NB-IoT networks. Homogeneous PPP are used to model the network and to simulate the distribution of active sensors and collectors. Based on the approximate analytical characterization of the interference Laplacian, we estimate the number of radio resource that should be allocated in the network to fulfill the network requirements in terms of limited transmission power per RR, low access delay, preset network outage probability and target data rate. We have also investigated the advantage of deploying multiple antennas at the receiver side. Our results highlight and quantify the radio resources gain obtained by the receiver diversity techniques and the multi-user gains in terms of power consumption and spectral occupancy.

In Chapter 3, we have proposed an adaptive multi sub-channel allocation strategy for LoRa networks. Depending on the characteristics of CSS modulation, the typical LoRa cell is divided into multiple SF partitions based on different values of SF (SF = 7 to 12). With respect to the distance to the station, a joint allocation of SF and one, two or four sub-channels of 125 kHz are allocated to a single sensor device. The sensors located in the SF region near the collector spread their signal

within bandwidth of 125 kHz, while the nodes in the middle part are given 250 kHz, and for the nodes located in the edge-cell of a given SF region, in 500 kHz of bandwidth. The simulation results show that the adaptive sub-channel allocation strategy outperforms the fixed allocation policy. It minimizes device power consumption and enhances the distribution of rates in the SF = 7 zone by statistically reducing the number of trials required for the edge nodes. These results are highly useful for network planners to find the dimensional parameters of the LoRa networks: the intensities of the gateway, the maximum power consumption, and to estimate the average data rate distribution in the network.

In Chapter 4, we continue our focus on LoRa networks. In contrast to the traditional statistical approach used in the previous chapters to handle the network resource planing, we employ an emerging machine learning approach to tackle the problem in this chapter. We propose a Q-learning algorithm to solve the dynamic SF allocation and power control problems in LoRa networks. The numerical results show that compared with the traditional static allocation algorithm, multi-agent Q-learning improves the energy efficiency.

The research topics that I am planning to develop fall within the context of the beyond 5G generation and the other alternative low power wide area networks.

1. **Incremental redundancy in non licensed LoRa networks** The high level of interference in unlicensed LoRa network induces significant packet loss and highly affects the network reliability. Current LoRa networks are based on time-diversity message replication. This induces a relatively high decoding latency especially for slow time-varying channel. When considering the evolution in time of the network, the interference does not change in an independent manner and correlation scheme model should be considered as in [131, 132]. We intend to model this time interference correlation, and to propose based on that an incremental redundancy scheme as in [133, 134] to enhance the packet recovery latency.

2. **Realistic network modeling** The derivations of Chapter 2 to 4 assume that the randomly appearing active sensors and collectors in an IoT network are distributed according to an homogeneous spatial PPP. In realistic network deployments, the scattering and clustering of the users create interaction between them and their locations are spatially correlated. The spatially correlated process is not mathematically tractable. Consequently, the uncorrelated assumption of PPP becomes non accurate. To further improve the simulation of the mathematical model

to the real situation, the Independent Double Thinning Approach (IDT), approximates the spatially correlated Point Process (PP) by means of two independent inhomogeneous I-PPPs.[135]. The densities of these two I-PPPs are related to the distance and are numerically chosen to minimize the mean square distance between the F-function of the first PP and the K-function of the second PP. Using this approach, we can obtain a more accurate modeling that is closer to the real-world case.

3. **Machine learning for beyond 5G networks** In this thesis, we have already examined the problems of resource allocation in an LPWA network with a multi-agent Q-learning algorithm. Machine learning tools are practical and promising technologies in the new 5G era. At the same time, for beyond 5G networks, massive network links create massive computational demands as more and more computation-intensive and data-intensive tasks are taken into account [136]. The combination of machine learning and Beyond 5G technology will lead to many innovations that will improve the performance of networks. For example, the deployment of Ultra Dense Networks (UDN) has attracted a great deal of interest [137]. UDN refers to the idea of densifying cellular networks to reduce the distance between access nodes and User Equipment (UE) in order to achieve the highest possible transmission rates and enhance QoS [138]. For instance, to improve the energy efficiency of the UDN, Deep Reinforcement Learning (DRL) approaches can be adopted to address this problem. In the following research after this thesis, we will consider DRL algorithms and apply them to solve complex computation-intensive tasks in Beyond 5G scenarios.

Bibliography

[1] A. Al-Fuqaha *et al.*, "Internet of things: A survey on enabling technologies, protocols, and applications," *IEEE communications surveys & tutorials*, vol. 17, n°. 4, p. 2347–2376, 2015.

[2] L. Atzori, A. Iera et G. Morabito, "The internet of things: A survey," *Computer networks*, vol. 54, n°. 15, p. 2787–2805, 2010.

[3] F. Wortmann et K. Flüchter, "Internet of things," *Business & Information Systems Engineering*, vol. 57, n°. 3, p. 221–224, 2015.

[4] L. Da Xu, W. He et S. Li, "Internet of things in industries: A survey," *IEEE Transactions on industrial informatics*, vol. 10, n°. 4, p. 2233–2243, 2014.

[5] S. Madakam *et al.*, "Internet of things (iot): A literature review," *Journal of Computer and Communications*, vol. 3, n°. 05, p. 164, 2015.

[6] M. Gerla *et al.*, "Internet of vehicles: From intelligent grid to autonomous cars and vehicular clouds," dans *2014 IEEE world forum on internet of things (WF-IoT)*. IEEE, 2014, p. 241–246.

[7] P. Schulz *et al.*, "Latency critical iot applications in 5g: Perspective on the design of radio interface and network architecture," *IEEE Communications Magazine*, vol. 55, n°. 2, p. 70–78, 2017.

[8] A. Brogi et S. Forti, "Qos-aware deployment of iot applications through the fog," *IEEE Internet of Things Journal*, vol. 4, n°. 5, p. 1185–1192, 2017.

[9] R. Gómez-Chabla *et al.*, "Iot applications in agriculture: A systematic literature review," dans *2nd International Conference on ICTs in Agronomy and Environment*. Springer, 2019, p. 68–76.

[10] X. Krasniqi et E. Hajrizi, "Use of iot technology to drive the automotive industry from connected to full autonomous vehicles," *IFAC-PapersOnLine*, vol. 49, n°. 29, p. 269–274, 2016.

[11] N. Naik, "Lpwan technologies for iot systems: choice between ultra narrow band and spread spectrum," dans *2018 IEEE International Systems Engineering Symposium (ISSE)*. IEEE, 2018, p. 1–8.

[12] "Lora official website," www.lora-alliance.org/.

[13] N. Sornin *et al.*, "Lorawan specification," *tECH; REP; LoRa Alliance*, 2016.

[14] G. T. . v13.1.0, "Cellular system support for ultra low complexity and low throughput internet of things," *[Online]*, November 2015.

[15] R. Ratasuk *et al.*, "NB-IoT System for M2M Communication," *IEEE Wireless Communications and Networking Conference Workshops (WCNCW)*, 2016.

[16] R. Ratasuk *et al.*, "Narrowband lte-m system for m2m communication," dans *2014 IEEE 80th vehicular technology conference (VTC2014-Fall)*. IEEE, 2014, p. 1–5.

[17] L. Vangelista, "Frequency shift chirp modulation: The lora modulation," *IEEE Signal Processing Letters*, vol. 24, n°. 12, p. 1818–1821, 2017.

[18] "3gpp release 13," https://www.3gpp.org/release-13.

[19] "3gpp release 14," https://www.3gpp.org/release-14.

[20] "3gpp release 15," https://www.3gpp.org/release-15.

[21] S. Li, L. Da Xu et S. Zhao, "5g internet of things: A survey," *Journal of Industrial Information Integration*, vol. 10, p. 1–9, 2018.

[22] V. Sharma *et al.*, "Energy efficient device discovery for reliable communication in 5g-based iot and bsns using unmanned aerial vehicles," *Journal of Network and Computer Applications*, vol. 97, p. 79–95, 2017.

[23] C. X. Mavromoustakis, G. Mastorakis et J. M. Batalla, *Internet of Things (IoT) in 5G mobile technologies*. Springer, 2016, vol. 8.

[24] I. Budhiraja *et al.*, "Tactile internet for smart communities in 5g: An insight for noma-based solutions," *IEEE Transactions on Industrial Informatics*, vol. 15, n°. 5, p. 3104–3112, 2019.

[25] A. Maeder *et al.*, "A scalable and flexible radio access network architecture for fifth generation mobile networks," *IEEE Communications Magazine*, vol. 54, n°. 11, p. 16–23, 2016.

[26] J. G. Andrews, A. K. Gupta et H. S. Dhillon, "A primer on cellular network analysis using stochastic geometry," *CoRR*, vol. abs/1604.03183, 2016. [En ligne]. Disponible: http://arxiv.org/abs/1604.03183

[27] F. Baccelli et B. Blaszczyszyn, "Stochastic Geometry and Wireless Networks: Volume I Theory," *Foundations and Trends in Networking*, vol. 3, n°. 34, p. 249–449, 2010.

[28] ——, "Stochastic Geometry and Wireless Networks: Volume II Application," *Foundations and Trends in Networking*, vol. 4, n°. 12, p. 1–312, 2010.

[29] M. Haenggi et R. Ganti, "Interference in Large Wireless Networks," *Foundations and Trends in Networking*, vol. 3, n°. 2, p. 127–248, 2009.

[30] R. Giacomelli, R. Ganti et M. Haenggi, "Outage Probability of General Ad Hoc Networks in the High-Reliability Regime," *IEEE/ACM Transactions in Networking*, vol. 19, n°. 4, p. 1151–1163, 2011.

[31] M. Haenggi, "Outage, local throughput, and capacity of random wireless networks," *IEEE Transactions on Wireless Communications*, vol. 8, n°. 8, p. 4350–4359, 2009.

[32] S. Weber, J. G. Andrews et N. Jindal, "An overview of the transmission capacity of wireless networks," *IEEE Trans. On Communications*, vol. 56, n°. 12, p. 3593–3604, 2010.

[33] S. Weber *et al.*, "Transmission Capacity of Wireless Ad Hoc Networks with Outage Constraints," *IEEE Trans. on Information Theory*, vol. 51, n°. 12, p. 4091–4102, 2005.

[34] M. Haenggi *et al.*, "Stochastic geometry and random graphs for the analysis and design of wireless networks," *IEEE journal on selected areas in communications*, vol. 27, n°. 7, p. 1029–1046, 2009.

[35] T. D. Novlan, H. S. Dhillon et J. G. Andrews, "Analytical modeling of uplink cellular networks," *IEEE Transactions on Wireless Communications*, vol. 12, n°. 6, p. 2669–2679, 2013.

[36] Y. Li *et al.*, "Statistical modeling and probabilistic analysis of cellular networks with determinantal point processes," *IEEE Transactions on communications*, vol. 63, n°. 9, p. 3405–3422, 2015.

[37] S. Singh, H. S. Dhillon et J. G. Andrews, "Offloading in heterogeneous networks: Modeling, analysis, and design insights," *IEEE transactions on wireless communications*, vol. 12, n°. 5, p. 2484–2497, 2013.

[38] H. S. Dhillon, R. K. Ganti et J. G. Andrews, "A tractable framework for coverage and outage in heterogeneous cellular networks," dans *2011 Information Theory and Applications Workshop*. IEEE, 2011, p. 1–6.

[39] L. Bu *et al.*, "A comprehensive survey of multiagent reinforcement learning," *IEEE Transactions on Systems, Man, and Cybernetics, Part C (Applications and Reviews)*, vol. 38, n°. 2, p. 156–172, 2008.

[40] M. Abdoos, N. Mozayani et A. L. Bazzan, "Traffic light control in non-stationary environments based on multi agent q-learning," dans *2011 14th International IEEE conference on intelligent transportation systems (ITSC)*. IEEE, 2011, p. 1580–1585.

[41] E. Rodrigues Gomes et R. Kowalczyk, "Dynamic analysis of multiagent q-learning with ε-greedy exploration," dans *Proceedings of the 26th annual international conference on machine learning*, 2009, p. 369–376.

[42] M. Kaisers et K. Tuyls, "Frequency adjusted multi-agent q-learning," dans *Proceedings of the 9th International Conference on Autonomous Agents and Multiagent Systems: volume 1-Volume 1*, 2010, p. 309–316.

[43] B. Reynders, W. Meert et S. Pollin, "Power and spreading factor control in low power wide area networks," dans *2017 IEEE International Conference on Communications (ICC)*. IEEE, 2017, p. 1–6.

[44] Y. Yi *et al.*, "Adaptive multi sub-bands allocation in lora networks," *Accepted by IEEE Access*, 2020.

[45] A. Zanella *et al.*, "Internet of things for smart cities," *IEEE Internet of Things journal*, vol. 1, n°. 1, p. 22–32, 2014.

[46] R. Ratasuk, N. Mangalvedhe et A. Ghosh, "Overview of lte enhancements for cellular iot," dans *2015 IEEE 26th annual international symposium on personal, indoor, and mobile radio communications (PIMRC)*. IEEE, 2015, p. 2293–2297.

[47] M. Centenaro *et al.*, "Long-range communications in unlicensed bands: The rising stars in the iot and smart city scenarios," *IEEE Wireless Communications*, vol. 23, n°. 5, p. 60–67, 2016.

[48] B. S. Chaudhari, M. Zennaro et S. Borkar, "Lpwan technologies: Emerging application characteristics, requirements, and design considerations," *Future Internet*, vol. 12, n°. 3, p. 46, 2020.

[49] Y. Kabalci *et al.*, "Internet of things applications as energy internet in smart grids and smart environments," *Electronics*, vol. 8, n°. 9, p. 972, 2019.

[50] P. A. Catherwood *et al.*, "A community-based iot personalized wireless healthcare solution trial," *IEEE journal of translational engineering in health and medicine*, vol. 6, p. 1–13, 2018.

[51] S. Duangsuwan *et al.*, "A study of air pollution smart sensors lpwan via nb-iot for thailand smart cities 4.0," dans *2018 10th International Conference on Knowledge and Smart Technology (KST)*. IEEE, 2018, p. 206–209.

[52] "Ericsson mobility report november 2019," https://www.ericsson.com/en/mobility-report/reports/november-2019.

[53] A. Ericsson, "Ericsson mobility report. ericsson," Sweden, Tech. Rep. EAB-17, 1. 1, Rapport technique, 2017.

[54] X. Xiong *et al.*, "Low power wide area machine-to-machine networks: key techniques and prototype," *IEEE Communications Magazine*, vol. 53, n°. 9, p. 64–71, 2015.

[55] A. Ikpehai *et al.*, "Low-power wide area network technologies for internet-of-things: A comparative review," *IEEE Internet of Things Journal*, vol. 6, n°. 2, p. 2225–2240, 2018.

[56] N. Mangalvedhe, R. Ratasuk et A. Ghosh, "Nb-iot deployment study for low power wide area cellular iot," dans *2016 ieee 27th annual international symposium on personal, indoor, and mobile radio communications (pimrc)*. IEEE, 2016, p. 1–6.

[57] I. Lee et K. Lee, "The internet of things (iot): Applications, investments, and challenges for enterprises," *Business Horizons*, vol. 58, n°. 4, p. 431–440, 2015.

[58] M. Marjani *et al.*, "Big iot data analytics: architecture, opportunities, and open research challenges," *IEEE Access*, vol. 5, p. 5247–5261, 2017.

[59] H. Malik *et al.*, "Radio resource management scheme in nb-iot systems," *IEEE Access*, vol. 6, p. 15 051–15 064, 2018.

[60] N. Kaur et S. K. Sood, "An energy-efficient architecture for the internet of things (iot)," *IEEE Systems Journal*, vol. 11, n°. 2, p. 796–805, 2015.

[61] H. Lu *et al.*, "The cognitive internet of vehicles for autonomous driving," *IEEE Network*, vol. 33, n°. 3, p. 65–73, 2019.

[62] E. Yurtsever *et al.*, "A survey of autonomous driving: Common practices and emerging technologies," *IEEE Access*, vol. 8, p. 58 443–58 469, 2020.

[63] D. A. Chekired *et al.*, "5g-slicing-enabled scalable sdn core network: Toward an ultra-low latency of autonomous driving service," *IEEE Journal on Selected Areas in Communications*, vol. 37, n°. 8, p. 1769–1782, 2019.

[64] P. Popovski *et al.*, "5g wireless network slicing for embb, urllc, and mmtc: A communication-theoretic view," *IEEE Access*, vol. 6, p. 55 765–55 779, 2018.

[65] A. Khanna et S. Kaur, "Evolution of internet of things (iot) and its significant impact in the field of precision agriculture," *Computers and electronics in agriculture*, vol. 157, p. 218–231, 2019.

[66] T. Popović *et al.*, "Architecting an iot-enabled platform for precision agriculture and ecological monitoring: A case study," *Computers and electronics in agriculture*, vol. 140, p. 255–265, 2017.

[67] S. Al-Sarawi *et al.*, "Internet of things (iot) communication protocols," dans *2017 8th International conference on information technology (ICIT)*. IEEE, 2017, p. 685–690.

[68] K. Mekki *et al.*, "Overview of cellular lpwan technologies for iot deployment: Sigfox, lorawan, and nb-iot," dans *2018 ieee international conference on pervasive computing and communications workshops (percom workshops)*. IEEE, 2018, p. 197–202.

[69] D. Patel et M. Won, "Experimental study on low power wide area networks (lpwan) for mobile internet of things," dans *2017 IEEE 85th Vehicular Technology Conference (VTC Spring)*. IEEE, 2017, p. 1–5.

[70] U. Raza, P. Kulkarni et M. Sooriyabandara, "Low power wide area networks: An overview," *IEEE Communications Surveys & Tutorials*, vol. 19, n°. 2, p. 855–873, 2017.

[71] A. Augustin *et al.*, "A study of lora: Long range & low power networks for the internet of things," *Sensors*, vol. 16, n°. 9, p. 1466, 2016.

[72] "Semtech official website/lora," https://www.semtech.com/lora/why-lora.

[73] L. Bao *et al.*, "Coverage analysis on nb-iot and lora in power wireless private network," *Procedia computer science*, vol. 131, p. 1032–1038, 2018.

[74] M. Lauridsen *et al.*, "Coverage comparison of gprs, nb-iot, lora, and sigfox in a 7800 km^2 area," dans *2017 IEEE 85th Vehicular Technology Conference (VTC Spring)*. IEEE, 2017, p. 1–5.

[75] B. Vejlgaard *et al.*, "Coverage and capacity analysis of sigfox, lora, gprs, and nb-iot," dans *2017 IEEE 85th vehicular technology conference (VTC Spring)*. IEEE, 2017, p. 1–5.

[76] R. Sanchez-Iborra *et al.*, "Performance evaluation of lora considering scenario conditions," *Sensors*, vol. 18, n°. 3, p. 772, 2018.

[77] A. J. Wixted *et al.*, "Evaluation of lora and lorawan for wireless sensor networks," dans *2016 IEEE SENSORS*. IEEE, 2016, p. 1–3.

[78] B. Reynders et S. Pollin, "Chirp spread spectrum as a modulation technique for long range communication," dans *2016 Symposium on Communications and Vehicular Technologies (SCVT)*. IEEE, 2016, p. 1–5.

[79] M. Knight et B. Seeber, "Decoding lora: Realizing a modern lpwan with sdr," dans *Proceedings of the GNU Radio Conference*, vol. 1, n°. 1, 2016.

[80] U. Noreen, A. Bounceur et L. Clavier, "A study of lora low power and wide area network technology," dans *2017 International Conference on Advanced Technologies for Signal and Image Processing (ATSIP)*. IEEE, 2017, p. 1–6.

[81] A. Adhikary, X. Lin et Y.-P. E. Wang, "Performance evaluation of nb-iot coverage," dans *2016 IEEE 84th Vehicular Technology Conference (VTC-Fall)*. IEEE, 2016, p. 1–5.

[82] W. Ayoub *et al.*, "Internet of mobile things: Overview of lorawan, dash7, and nb-iot in lpwans standards and supported mobility," *IEEE Communications Surveys & Tutorials*, vol. 21, n°. 2, p. 1561–1581, 2018.

[83] R. Ratasuk *et al.*, "Overview of narrowband iot in lte rel-13," dans *2016 IEEE conference on standards for communications and networking (CSCN)*. IEEE, 2016, p. 1–7.

[84] J. G. Andrews *et al.*, "What will 5g be?" *IEEE Journal on selected areas in communications*, vol. 32, n°. 6, p. 1065–1082, 2014.

[85] Y. Cai *et al.*, "Modulation and multiple access for 5g networks," *IEEE Communications Surveys & Tutorials*, vol. 20, n°. 1, p. 629–646, 2017.

[86] M. Series, "Imt vision–framework and overall objectives of the future development of imt for 2020 and beyond," *Recommendation ITU*, p. 2083–0, 2015.

[87] S. Sun *et al.*, "Propagation models and performance evaluation for 5g millimeter-wave bands," *IEEE Transactions on Vehicular Technology*, vol. 67, n°. 9, p. 8422–8439, 2018.

[88] J. G. Andrews, W. Choi et R. W. Heath, "Overcoming interference in spatial multiplexing mimo cellular networks," *IEEE Wireless Communications*, vol. 14, n°. 6, p. 95–104, 2007.

[89] S. Jacobsson *et al.*, "Quantized precoding for massive mu-mimo," *IEEE Transactions on Communications*, vol. 65, n°. 11, p. 4670–4684, 2017.

[90] Z. Shen *et al.*, "Low complexity user selection algorithms for multiuser mimo systems with block diagonalization," *IEEE Transactions on Signal Processing*, vol. 54, n°. 9, p. 3658–3663, 2006.

[91] S. Shim *et al.*, "Block diagonalization for multi-user mimo with other-cell interference," *IEEE Transactions on Wireless Communications*, vol. 7, n°. 7, p. 2671–2681, 2008.

[92] B. Nosrat-Makouei, J. G. Andrews et R. W. Heath, "Mimo interference alignment over correlated channels with imperfect csi," *IEEE Transactions on Signal Processing*, vol. 59, n°. 6, p. 2783–2794, 2011.

[93] J. Zhang *et al.*, "Multi-mode transmission for the mimo broadcast channel with imperfect channel state information," *IEEE Transactions on Communications*, vol. 59, n°. 3, p. 803–814, 2010.

[94] S. Sur *et al.*, "Practical mu-mimo user selection on 802.11 ac commodity networks," dans *Proceedings of the 22nd Annual International Conference on Mobile Computing and Networking*, 2016, p. 122–134.

[95] C. Jeon *et al.*, "Decentralized equalization with feedforward architectures for massive mu-mimo," *IEEE Transactions on Signal Processing*, vol. 67, n°. 17, p. 4418–4432, 2019.

[96] L. Decreusefond, E. Ferraz et P. Martins, "Upper bound of loss probability for the dimensioning of ofdma systems with multi class randomly located users," dans *Proc. WiOpt*, 2009, p. 1–6.

[97] M. Haenggi, "On distances in uniformly random networks," *IEEE Transactions on Information Theory*, vol. 51, n°. 10, p. 3584–3586, 2005.

[98] R. Ganti et M. Haenggi, "Interference in large wireless networks, vol. 3," *Now, Paris*, 2009.

[99] P. Frankl et H. Maehara, "Some geometric applications of the beta distribution," *Annals of the Institute of Statistical Mathematics*, vol. 42, n°. 3, p. 463–474, 1990.

[100] V. Pong *et al.*, "Temporal difference models: Model-free deep rl for model-based control," *arXiv preprint arXiv:1802.09081*, 2018.

[101] P. Hernandez-Leal, B. Kartal et M. E. Taylor, "A survey and critique of multiagent deep reinforcement learning," *Autonomous Agents and Multi-Agent Systems*, vol. 33, n°. 6, p. 750–797, 2019.

[102] K. Mekki *et al.*, "A comparative study of lpwan technologies for large-scale iot deployment," *ICT express*, vol. 5, n°. 1, p. 1–7, 2019.

[103] B. Martinez *et al.*, "Exploring the performance boundaries of nb-iot," *IEEE Internet of Things Journal*, vol. 6, n°. 3, p. 5702–5712, 2019.

[104] S. Al-Rubaye *et al.*, "Call admission control for non-standalone 5g ultra-dense networks," *IEEE Communications Letters*, vol. 22, n°. 5, p. 1058–1061, 2018.

[105] D. Bankov *et al.*, "Ofdma uplink scheduling in ieee 802.11 ax networks," dans *2018 IEEE International Conference on Communications (ICC)*. IEEE, 2018, p. 1–6.

[106] W. R. Ghanem *et al.*, "Resource allocation for multi-user downlink miso ofdma-urllc systems," *IEEE Transactions on Communications*, 2020.

[107] L. Decreusefond, E. Ferraz et P. Martins, "Upper Bound of Loss probability for the dimensioning of OFDMA systems with multi class randomly located users," dans *WiOpt, workshop SPASWIN, IEEE 2009*. IEEE, 2009.

[108] L. Decreusefond *et al.*, "Robust methods for LTE and WiMAX dimensioning," dans *6th International Conference on Performance Evaluation Methodologies and Tools*. IEEE, 2012.

[109] F. Kaddour *et al.*, "Robust methods for LTE and WiMAX dimensioning," dans *6th International Conference on Performance Evaluation Methodologies and Tools*. IEEE, 2013.

[110] L. Mroueh *et al.*, "Radio Resource Dimensioning in a Centralized Ad-Hoc Maritime MIMO LTE Network," dans *IEEE Sarnoff conference*. IEEE, 2013.

[111] L. Mroueh *et al.*, "Statistical uplink dimensioning in licensed cellular low power iot networks," dans *2018 25th International Conference on Telecommunications (ICT)*. IEEE, 2018, p. 527–531.

[112] J. Lee et N. Jindal, "High snr analysis for mimo broadcast channels: Dirty paper coding versus linear precoding," *IEEE Transactions on Information Theory*, vol. 53, n°. 12, p. 4787–4792, 2007.

[113] "Coverage analysis of LTE-M category M1," *White Paper*, 2017.

[114] R. Tanbourgi *et al.*, "Effect of spatial interference correlation on the performance of maximum ratio combining," *IEEE Transactions on Wireless Communications*, vol. 13, n°. 6, p. 3307–3316, 2014.

[115] "Ericsson mobility report 2018," https://www.ericsson.com/assets/local/mobility-report/documents/2018/ericsson-mobility-report-june-2018.pdf.

[116] "Lorawan specification," https://lora-alliance.org/lorawan-for-developers.

[117] "Semtech website for lora developper," https://lora-developers.semtech.com/.

[118] N. Jovalekic *et al.*, "Experimental study of lora transmission over seawater," *Sensors*, vol. 18, n°. 9, p. 2853, 2018.

[119] J. Gaelens *et al.*, "Lora mobile-to-base-station channel characterization in the antarctic," *Sensors*, vol. 17, n°. 8, p. 1903, 2017.

[120] J. Petäjäjärvi *et al.*, "Performance of a low-power wide-area network based on lora technology: Doppler robustness, scalability, and coverage," *International Journal of Distributed Sensor Networks*, vol. 13, n°. 3, p. 1550147717699412, 2017.

[121] T. Bouguera *et al.*, "Energy consumption model for sensor nodes based on lora and lorawan," *Sensors*, vol. 18, n°. 7, p. 2104, 2018.

[122] J. C. Liando *et al.*, "Known and unknown facts of lora: Experiences from a large-scale measurement study," *ACM Transactions on Sensor Networks (TOSN)*, vol. 15, n°. 2, p. 1–35, 2019.

[123] C. Goursaud et J.-M. Gorce, "Dedicated networks for iot: Phy/mac state of the art and challenges," *EAI endorsed transactions on Internet of Things*, 2015.

[124] O. Georgiou et U. Raza, "Low power wide area network analysis: Can lora scale?" *IEEE Wireless Communications Letters*, vol. 6, n°. 2, p. 162–165, 2017.

[125] A. Springer *et al.*, "Spread spectrum communications using chirp signals," dans *IEEE/AFCEA EUROCOMM 2000. Information Systems for Enhanced Public Safety and Security (Cat. No. 00EX405)*. IEEE, 2000, p. 166–170.

[126] G. Ferré et A. Giremus, "Lora physical layer principle and performance analysis," dans *2018 25th IEEE International Conference on Electronics, Circuits and Systems (ICECS)*. IEEE, 2018, p. 65–68.

[127] C. Szepesvári, "Algorithms for reinforcement learning," *Synthesis lectures on artificial intelligence and machine learning*, vol. 4, n°. 1, p. 1–103, 2010.

[128] "Sigfox official website," www.sigfox.com.

[129] A. Azari et C. Cavdar, "Self-organized low-power iot networks: A distributed learning approach," dans *2018 IEEE Global Communications Conference (GLOBECOM)*. IEEE, 2018, p. 1–7.

[130] "Ieee 802.15 working group for wireless specialty networks (wsn) website / ieee 802.15 documents," http://www.ieee802.org/15//.

[131] Z. Gong et M. Haenggi, "Interference and outage in mobile random networks: Expectation, distribution, and correlation," *IEEE Transactions on Mobile Computing*, vol. 13, n°. 2, p. 337–349, 2014.

[132] U. Schilcher, C. Bettstetter et G. Brandner, "Temporal correlation of interference in wireless networks with rayleigh block fading," *IEEE Transactions on Mobile Computing*, vol. 11, n°. 12, p. 2109–2120, 2012.

[133] A. Rajanna et M. Haenggi, "Enhanced cellular coverage and throughput using rateless codes," *IEEE Transactions on Communications*, vol. 65, n°. 5, p. 1899–1912, 2017.

[134] B. Li *et al.*, "Capacity-achieving rateless polar codes," dans *Information Theory (ISIT), 2016 IEEE International Symposium on*. IEEE, 2016, p. 46–50.

[135] M. Di Renzo, S. Wang et X. Xi, "Inhomogeneous double thinning?modeling and analysis of cellular networks by using inhomogeneous poisson point processes," *IEEE Transactions on Wireless Communications*, vol. 17, n°. 8, p. 5162–5182, 2018.

[136] M. Chen et Y. Hao, "Task offloading for mobile edge computing in software defined ultra-dense network," *IEEE Journal on Selected Areas in Communications*, vol. 36, n°. 3, p. 587–597, 2018.

[137] Q. Ren *et al.*, "Analysis of spectral and energy efficiency in ultra-dense network," dans *2015 IEEE International Conference on Communication Workshop (ICCW)*. IEEE, 2015, p. 2812–2817.

[138] A. Khodmi *et al.*, "A joint power allocation and user association based on non-cooperative game theory in an heterogeneous ultra-dense network," *IEEE Access*, vol. 7, p. 111 790–111 800, 2019.

le cnam

Yi YU

Radio Resource Planning in Low Power Wide Area IoT Networks

le cnam

Résumé : Cette thèse étudie le problème de planification des ressources pour les réseaux IoT longues portées basés sur les technologies NB-IoT et LoRa. Dans les deux cas, on suppose que les capteurs et les collecteurs sont distribués suivant des processus de points de Poisson spatial indépendants marqués par le caractère aléatoire du canal. Pour le NB-IoT, nous élaborons un modèle de dimensionnement statistique qui estime le nombre de ressources radio nécessaires en fonction du délai d'accès toléré, de la densité des noeuds actifs, des collecteurs et de la configuration de l'antenne. Pour le réseau LoRa, nous proposons une technique d'allocation de plusieurs sous-bandes pour atténuer le niveau élevé d'interférence induit par les noeuds qui transmettent avec le même facteur d'étalement. Pour allouer dynamiquement le facteur d'étalement et la puissance, nous présentons une approche d'apprentissage automatique avec multi-agents qui permet d'améliorer l'efficacité énergétique.

Mots clés : LPWAN, NB-IoT, LoRa, Spatial Point Poisson Process, Chirp Spread Spectrum, allocation de ressources, Q-Learning

Abstract: In this thesis, we focus on radio resource planning issues for low power wide area networks based on NB-IoT and LoRa technologies. In both cases, the average behavior of the network is considered by assuming the sensors and the collectors are distributed according to independent random Poisson Point Process marked by the channel randomness. For the NB-IoT, we elaborate a statistical dimensioning model that estimates the number of radio resources in the network depending on the tolerated delay access, the density of active nodes, the collectors, and the antenna configuration with single and multi-user transmission. For the LoRa network, we propose a multi-sub band allocation technique to mitigate the high level of interference induced by nodes that transmit with the same spreading factor. To dynamically allocate the spreading factor and the power, we present a Q-learning multi-agent approach to improve the energy efficiency.

Keywords: LPWAN, NB-IoT, LoRa, Spatial Point Poisson Process, Chirp Spread Spectrum, resource allocation, Q-Learning